INTERNATIONAL CENTER FOR AGGREGATES RESEARCH

ICAR

Automation of Aggregate Characterization Using Laser Profiling and Digital Image Analysis

RESEARCH REPORT ICAR – 503-3F

Sponsored by the
Aggregates Foundation
for Technology, Research and Education

Technical Report Documentation Page

1. Report No. ICAR 503-3	2. Government Accession No.	3. Recipient's Catalog No.
4. Title and Subtitle RAPID TEST TO ESTABLISH GRADING OF UNBOUND AGGREGATE PRODUCTS: Automation of Aggregate Characterization Using Laser Profiling and Digital Image Analysis		5. Report Date June 2002 6. Performing Organization Code
7. Author(s) Carl T. Haas, Alan F. Rauch, Hyoungkwan Kim, and Craig Browne		8. Performing Organization Report No. ICAR 503-3F
9. Performing Organization Name and Address International Center for Aggregates Research The University of Texas at Austin Cockrell Hall 5.200 Austin, TX 78712-1076		10. Work Unit No. (TRAIS) 11. Contract or Grant No. Project No. ICAR-503
12. Sponsoring Agency Name and Address Aggregates Foundation for Technology, Research, and Education 1415 Elliott Place NW Washington, D.C. 20007		13. Type of Report and Period Covered Final Report Sept. 1, 1999 – June 1, 2002 14. Sponsoring Agency Code
15. Supplementary Notes		

16. ABSTRACT

This final project report describes the development of a laser scanning device for measuring the gradation and other morphological characteristics of unbound construction aggregates. The device is called the *LASS*, for "Laser-based Aggregate Scanning System". The method of characterizing aggregate particles from three-dimensional (3D) laser profiling required the development of particle segmentation algorithms, particle measurement algorithms, and generalized particle descriptors. With the *LASS*, true 3D data of aggregate particles are obtained by laser profiling. This data is first transformed into digital images. Second, segmentation and particle measurement algorithms separate the particles and process each particle data individually with the aid of various digital image technologies. Finally, in order to provide a generalized, quantitative, and representative way to characterize aggregate particles, 3D particle descriptors were developed using the multi-resolution analysis feature of wavelet transforms. Verification tests show that this approach can characterize various aggregate properties in a fast, accurate, and reliable way. When implemented, this ability to automatically analyze multiple characteristics of an aggregate sample will lead to reduced labor costs in the laboratory, but more importantly, to better control of the quality of aggregate products. ICAR Project 503 was undertaken to study rapid, automated methods of determining the grain size distribution of unbound aggregate products. Automatic measurement of particle size and shape properties has the potential to overcome problems with manual measurements such as subjectivity, labor intensity, and slow speed. Testing machines that rely on 2D digital image analysis were evaluated as described earlier in Report ICAR 503-2.

17. Key Words	18. Distribution Statement
angularity, digital image analysis, gradation, laser profiling, proportional caliper, shape, sieve analysis, texture	No restrictions

19. Security Classif. (of report)	20. Security Classif. (of this page)	21. No. of pages	22. Price
Unclassified	Unclassified	182	

Form DOT F 1700.7 (8-72) Reproduction of completed page authorized

RAPID TEST TO ESTABLISH GRADING OF UNBOUND AGGREGATE PRODUCTS

Automation of Aggregate Characterization Using Laser Profiling and Digital Image Analysis

by:

Carl T. Haas
Alan F. Rauch
Hyoungkwan Kim
Craig Browne

Department of Civil Engineering
The University of Texas at Austin
Austin, Texas

June 2002

Research Report ICAR 503-3F

Research Project Number ICAR-503

Sponsored by the
Aggregates Foundation for Technology, Research, and Education

INTERNATIONAL CENTER FOR AGGREGATES RESEARCH
The University of Texas at Austin
Austin, Texas 78712
and
Texas A&M University
College Station, Texas 77843

DISCLAIMER

The contents of this report reflect the views of the authors who are responsible for the accuracy of the information presented herein. The contents do not necessarily reflect the official views of the International Center for Aggregates Research (ICAR). This report does not constitute a standard, specification, or regulation.

ACKNOWLEDGEMENTS

This is final report from a study sponsored by the Aggregates Foundation for Technology, Research, and Education (AFTRE). The authors gratefully acknowledge the sponsorship of AFTRE.

Table of Contents

List of Tables

List of Figures

List of Acronyms

- 2D: Two-dimensional
- 3D: Three-dimensional
- AHP: Analytical Hierarchy Process
- CANWE: Cumulative And Normalized Weighted Error
- CCD: Charge Coupled Device
- DAU: Data Acquisition Unit
- DIA: Digital Image Analysis
- EFR: Elongation and Flatness Ratio
- FIR: Finite Impulse Response
- HMA: Hot Mix Asphalt
- HPF: High Pass Filter
- ICAR: International Center for Aggregate Research
- JPEG: Joint Photographic Experts Group
- LASS: Laser-based Aggregate Scanning System
- LPF: Low Pass Filter
- MRA: Multiple-Resolution Analysis
- PCC: Portland Cement Concrete
- ROI: Region Of Interest
- Superpave: Superior Performing Asphalt Pavements

CHAPTER 1
INTRODUCTION

1.1 BACKGROUND

The United States produces a total of 2.7 billion metric tons of aggregates valued at $14.2 billion per year (Tepordei 2001). The aggregates are utilized in a variety of applications, including road base courses, railway ballast layers, drainage systems, water filter systems, erosion control systems, and most importantly as a component of Portland Cement Concrete (PCC) and Hot Mix Asphalt (HMA). Stone aggregates represent 70 to 85 percent of PCC and 90 to 95 percent of HMA by weight (National Stone Association 1993). Considering the fact that PCC and HMA are major construction materials, it would not be difficult to imagine the enormous magnitude of influence that construction aggregates may have on the quality of such civil engineering structures as buildings, bridges, airports, highways, dams, etc.

The characteristics of aggregates are crucial to the lifespan of the structure where they are used. As the wide range of aggregate usages may imply, it is important to select aggregates that have proper characteristics for each specific application. Examples show numerous failures traceable directly to improper aggregate selection and use, such as inappropriate design of aggregate base course that led to premature breakup of pavements, rapid deterioration of PCC caused by nondurable aggregates, rapid pavement erosion from using unacceptable

aggregate in asphalt concrete construction, and so on (National Stone Association 1993).

Particle morphological characteristics such as size, shape, angularity, and texture are key properties that are frequently used to characterize aggregates. They are known to have a significant impact on the performance of PCC and HMA (Ahlrich 1996, Barksdale and Samir 1989, Kuo et al. 1998, and National Stone Association 1993). However, it is difficult to conduct aggregate characterization in a timely manner using standard aggregate test methods. For example, the sieve analysis (ASTM C 136) and the standard test method for index of aggregate particle shape and texture (ASTM D 3398) require a significant amount of time and human intervention. Similarly, the proportional caliper method for flat and elongated particles (ASTM D 4791) and the standard test method for determining the percentage of fractured particles in coarse aggregate (ASTM D 5821) require labor-intensive, manual measurements of individual aggregate particles. Moreover, there is a strong need for well-defined particle descriptors to provide accurate and objective quantification of particle characteristics, which goes beyond the current standardized methods.

In aggregate producing plants, PCC plants, HMA plants, or even large construction sites, a fast, accurate, and reliable way to characterize aggregate is needed. Based on the resulting information, prompt, necessary actions could then be taken to improve the quality of the product. In an aggregate producing plant, the equipment setup could be changed on a real time basis if unacceptable product was being produced. In PCC and HMA plants, the proportions of different

aggregates could be adjusted. In large construction sites, a decision on whether to accept the supplied aggregate could be easily made.

Increased awareness of the importance of aggregate properties and increased expectation of high quality aggregate products are motivating new developments in aggregate characterization. In particular, recent technological advances in computer technology, along with a trend to tighten specifications for aggregate properties (Kennedy et al. 1994), indicate a strong need to develop automated methods to determine aggregate properties (Kruse 1999).

1.2 RESEARCH OBJECTIVES

The main objective of this research is to develop a three-dimensional (3D) measurement method for characterizing aggregates in a faster, more accurate, and more reliable manner than those methods currently available. Four subobjectives include:

1. Development of a 3D particle data acquisition system: As a first step, it is crucial to obtain high quality particle surface data. Laser profiling techniques are used to produce sufficient 3D data.
2. Development of a robust particle segmentation algorithm: To accurately determine particle size and shape parameters, each particle data should be isolated and identified as a unique region so that it can be processed individually. Consequently, it is necessary to develop an efficient particle segmentation algorithm that can work well with the 3D laser-based data.

3. Development of a particle measurement algorithm: This subobjective aims to develop an algorithm that provides particle shape and size parameters that correlate to results of ASTM D 4791 (Standard test method for flat particles, elongated particles, or flat and elongated particles in coarse aggregate) and ASTM C 136 (Standard test method for sieve analysis of fine and coarse aggregates).
4. Development of 3D particle descriptors: To accurately identify and quantify critical aggregate characteristics, well-defined particle descriptors are essential. Then, based on this quantified data, better design and construction methods can be developed, especially in terms of aggregate selection and production. This subobjective aims to develop 3D particle descriptors to characterize morphological properties of particles in an objective, comprehensive, and generalized manner.

1.3 HYPOTHESIS

The underlying hypothesis of this research is that 3D measurement tools can improve the speed, accuracy, and capability of automated aggregate characterization, beyond that of conventional methods or 2D analysis.

1.4 RESEARCH SCOPE AND METHODOLOGY

This study focused on laser profiling techniques as a 3D data acquisition method and digital image analysis (DIA) as a way to analyze the obtained data, in order to automate aggregate characterization. This research direction was

determined, as shown in Figure 1.1, based on the research hypothesis, literature review, site visits to aggregate, PCC, and HMA plants, and interviews with experts. This research also focused on characterizing aggregates ranging in size from a no. 8 mesh (2.36 mm) sieve to 50 mm, which covers the vast majority of coarse aggregates produced. Once this objective is achieved, it could be easily modified to cover larger or smaller particles by changing the resolutions of the data acquisition hardware.

After a prototype system was developed using the selected technologies, it was first applied to the determination of dimensional ratios of aggregates such as elongation and flatness ratios. The results were compared with those of the proportional caliper measurements (ASTM D 4791). Second, the system was applied to the characterization of size distribution of aggregates, where the results were compared with those of the conventional sieve analyses (ASTM C 136). Finally, aggregates' morphological properties such as shape, angularity, and texture were quantified by the system. Since there is no proper standardized way of measuring these morphological properties directly, the system's results were compared with human visual perception to be verified. The overall research steps are shown in Figure 1.1.

1.5 ORGANIZATION OF THE REPORT

Chapter 2 presents the current standardized methods and five different alternative methods of measuring aggregate particle properties that were identified as candidates for the prototype rapid aggregate characterization device.

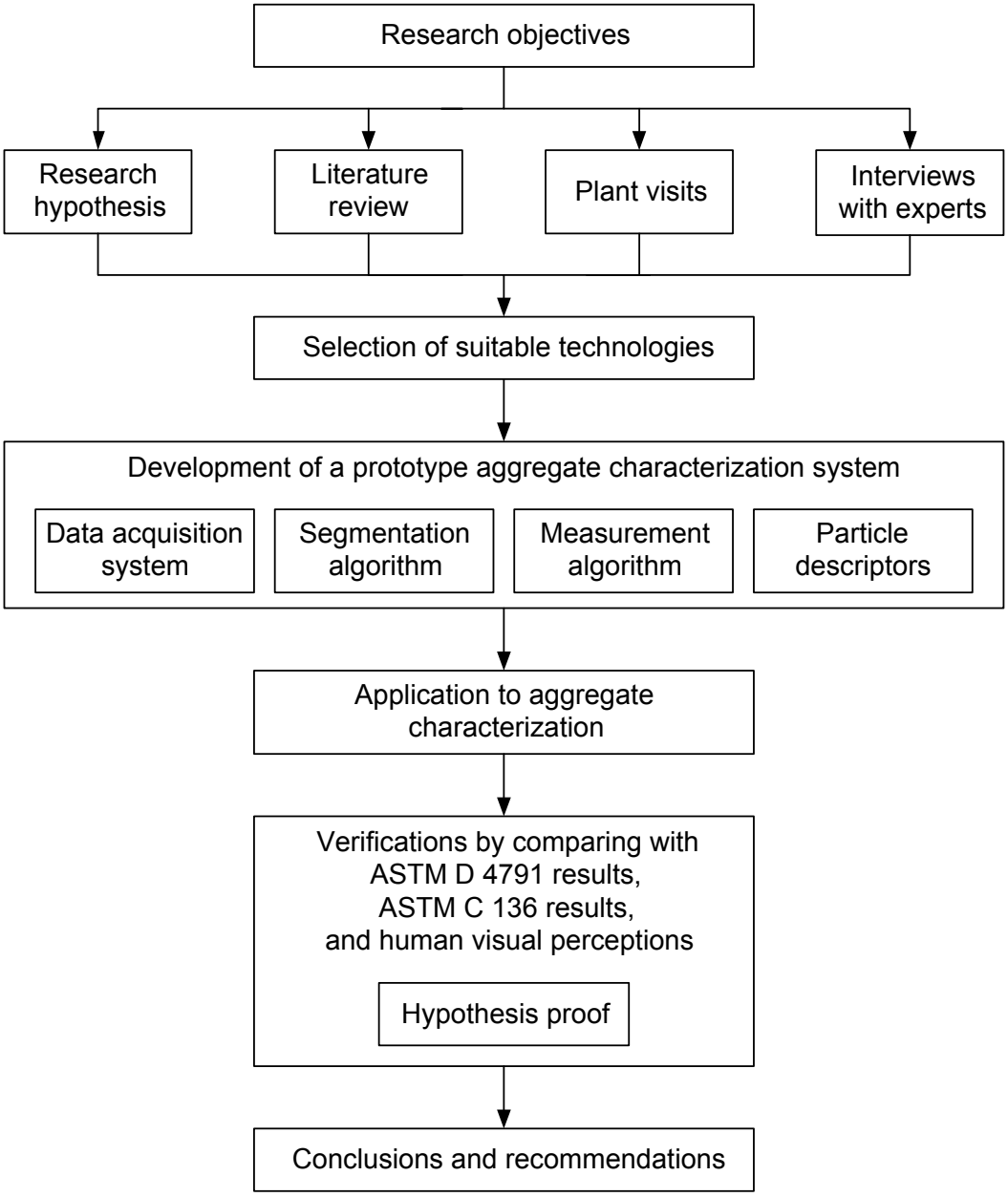

Figure 1.1: Research Steps.

Chapter 2 also shows how the alternative methods were evaluated and compared with each other using analytical analytical hierarchy process and how laser profiling and digital image analysis were selected as best suited for this research.

Chapter 3 presents the work on building the 3D data acquisition device. The chapter begins by a discussion of the laser profiling mechanism followed by descriptions of the hardware system architecture. Next, an image creation method for effectively storing the 3D data is described.

Chapter 4 describes the developed segmentation algorithm. It first establishes the need for a good particle segmentation method, and provides background information. Subsequently, the developed algorithm is presented with a step by step graphical example.

The particle measurement methodologies for determining size and shape parameters are reported in Chapter 5. This chapter first shows how the shape of a particle is measured using the so-called "virtual caliper" method. Then, the so-called "virtual sieve" method is introduced to determine particle size parameter. Experimental results of these "virtual" methods are compared with those of the standardized methods to verify their validity.

In Chapter 6, the motivation for development of new 3D particle descriptors is first established. Then, possible technologies that can be used for developing particle descriptors are reviewed with the main focus on wavelet transform. Finally, the descriptors are defined, and their physical meanings are discussed along with verification test results.

Chapter 7 addresses several issues related to the implementation of a fast aggregate characterization system including a modular system architecture that involves the idea of ubiquity of the data acquisition units. It also presents a simple economic feasibility study that demonstrates the justification of the purchase of the developed aggregate characterization system.

In chapter 8, conclusions and contributions are identified, and potential benefits of the developed system are also drawn. Finally, future research is recommended.

CHAPTER 2
BACKGROUND

The main objective of this chapter is to establish a foundation for the development of an automated aggregate characterization system. Section 2.1 presents the current standardized particle measurement methods including the conventional sieve analysis, proportional caliper analysis, visual methods, and indirect methods, while section 2.2 examines the feasibility of using various different technologies as an alternative way of characterizing aggregate particles. Finally, section 2.3 shows how laser profiling and digital image analysis are chosen through analytical hierarchy process as the technologies best suited for the research objectives.

2.1 STANDARD METHODS FOR PARTICLE CHARACTERIZATION

2.1.1 Sieve Analysis

The conventional sieve analysis (ASTM C 136) is the industry-accepted practice for determining particle size parameters. After a series of sieves are nested in order of decreasing sieve opening size from top to bottom, the aggregate sample is placed on the top sieve. Then, the sieves are agitated by hand or a mechanical apparatus (sieve shaker) for a sufficient amount of time so that the aggregate particles are sorted into different size brackets defined by the opening sizes of the sieves. If it is deemed that no more than one percent by mass of the material retained on any individual sieve will pass that sieve during one more

minute of continuous sieving, the sieving is finished, and the mass of each size bracket is measured on a scale. In this way, percentages passing, total percentages retained, or percentages in various size fractions on the basis of the total mass of the initial aggregate sample can be calculated. If the particle weights are accumulated as they proceed from smallest to largest mesh size and expressed as a percentage, the cumulative particle size distribution (gradation curve) is obtained. Aggregate gradation is key to controlling the quality of the mixed product such as portland cement concrete, hot mix asphalt, etc. Since the proportion of different grain sizes in a mixture is critical to the workability, strength, and durability of the product, the gradation is used in a variety of construction related specifications. The optimum gradation for most construction applications is approximately the particle size distribution that allows the maximum amount of aggregate to be included in a unit volume of mixture (National Stone Association 1993).

However, this conventional sieve test is time-consuming. Even automatic mechanical shakers need up to 20 minutes of shaking time to sufficiently separate a mixed sample of mineral aggregate into a nested stack of sieves of progressively smaller opening sizes (Aljassar 1993). In addition, manual checking and brief hand sieving are required to make sure that all particles retained on a sieve are bigger than the sieve apertures because not all particles retained on a sieve are really larger than the sieve apertures (Mora et al. 1998). Consequently, sieve testing is generally not fast enough for real-time adjustments of the aggregate mix

so that the production of large quantities of improperly graded material may be prevented.

2.1.2 Proportional Caliper Method

The shape of coarse aggregate particles may be characterized in a number of ways, but a widely used technique involves evaluating elongation and flatness ratios based on the three principal dimensions of a particle as specified in ASTM D 4791. If a particle is circumscribed in a virtual rectangular prism of minimum size as indicated in Figure 2.1, then the length, width, and thickness of the prism correspond to the longest, intermediate, and shortest dimensions of the particle, respectively. The principal dimensions can be measured using a conventional vernier caliper as shown in Figure 2.2 (a), or an electronic caliper (Jahn 2000). Elongation is then defined as the ratio of the longest to the intermediate dimension, while flatness is defined as the ratio of the intermediate to the shortest dimension.

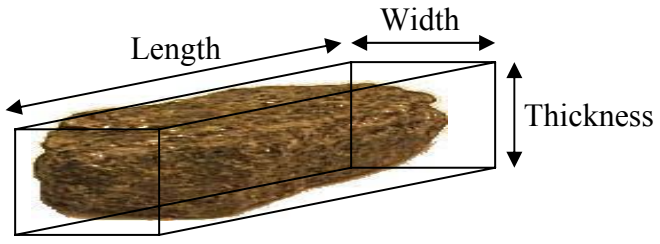

$$Flatness = \frac{Width}{Thickness} \qquad Elongation = \frac{Length}{Width}$$

Figure 2.1: Principal dimensions of an aggregate particle and definition of dimensional ratios.

To manually characterize the flatness and elongation of an aggregate sample, each particle is evaluated individually with a proportional caliper, which is shown in Figure 2.2 (b). Upon inspecting each particle, a technician must visualize the orientation corresponding to the smallest rectangular box that would circumscribe the particle. The technician then sets one side of the proportional caliper to the particle length. If the rotated particle will pass through the smaller opening on the caliper using the width, the particle is then classified as elongated according to the dimensional ratio set on the caliper. If the technician wants to determine the particle's flatness ratio, the same process is repeated using the width and thickness of the particle. Also, if the particle has a ratio of length to thickness greater than the specified value, it is called flat and elongated. In this way, each particle can be classified as to whether or not it is flat, elongated, or flat and elongated. The proportional caliper must be reset and the test repeated to determine how many particles in the sample are categorized according to a different limiting dimensional ratio. As the above description indicates, this manual shape measurement method is a tedious, labor intensive, and costly process.

It is generally recognized that cubic particles are desired to develop aggregate interlock, which increases the shear strength of hot mix asphalt (HMA) and unbound aggregate base material (National Stone Association 1993). Relatively flat or elongated particles are also known to contribute to segregation and aggregate breakdown during compaction of HMA (Kennedy et al. 1994). This

is why the use of flat and elongated particles is limited to a maximum of 10 % in the Superior Performing Asphalt Pavements (Superpave) mix design method.

(a)

(b)

Figure 2.2: (a) A vernier caliper; (b) a proportional caliper conforming to ASTM D 4791.

2.1.3 Visual Methods

It is more difficult to measure particle properties such as angularity and texture, because they need to be measured based on finer scales than the scale used for the measurement of size or shape. As a result, ASTM D 2488 (Standard practice for description and identification of soils) and ASTM D 5821 (Standard test method for determining the percentage of fractured particles in coarse aggregate) both rely on human visual perception to measure coarse aggregate

angularity. ASTM D 2488 describes aggregate particles as angular, subangular, subrounded, or rounded in accordance with the following criteria:

- Angular: particles have sharp edges and relatively plane sides with unpolished surfaces
- Subangular: particles are similar to angular particles but have rounded edges
- Subrounded: particles have nearly plane sides but have well-rounded corners and edges
- Rounded: particles have smoothly curved sides and no edges

In a slightly different manner, ASTM D 5821 specifies the way the particle angularity is determined. It begins with defining "fractured face" as an angular, rough, or broken surface of an aggregate particle created by crushing, by other artificial means, or by nature. Then, any particle with at least the minimum number of fractured faces specified (usually one or two) is considered a fractured particle. The Superpave guideline recommends the use of fractured particles in hot mix asphalt mixes because those angular particles ensure an adequate aggregate skeleton to resist shear forces that cause rutting (Kennedy et al. 1994).

These standardized methods are examples that show the efforts expended in order to enhance the life of construction structures through the selection of the most suitable aggregate mix. However, the above methods are labor-intensive, time-consuming, and subject to human errors. Moreover, important properties of aggregates may not be captured using these simple measurement methods.

2.1.4 Indirect Methods

In an effort to avoid the laborious particle by particle measurement for the determination of aggregate morphological properties, some indirect methods have

been used. ASTM D 3398 and ASTM C 1252 represent two examples. ASTM D 3398 (Standard test method for index of aggregate particle shape and texture) makes use of the phenomenon that the shape and texture of aggregates of almost equal size affect the initial void ratio and the changed void ratio after being compacted in a specified way. The particle index defined in ASTM D 3398 tends to be bigger with crushed and rough particles. In a similar way, ASTM C 1252 (Standard test method for uncompacted void content of fine aggregate (as influenced by particle shape, surface texture, and grading)) was developed based on the concept that aggregate properties such as shape, texture, and gradation are closely related to the loose uncompacted void content. Studies concluded that decreasing aggregate angularity and smoother surface textures decrease the loose uncompacted void content (Ahlrich 1996). This testing method was also expanded to coarse aggregate measurement. Ahlrich (1996) modified and enlarged the test apparatus used in ASTM C 1252 to test particles in the range of 4.75 to 19 mm.

These indirect methods have clear advantages over such tedious direct particle measurement methods as ASTM D 4791, ASTM D 5821, etc. As a result, the Superpave design method specifies ASTM C 1252 as a standard way of measuring fine aggregate angularity. However, the very indirectness in those methods is not that advantageous to the production or mixing of aggregates. For example, if a group of aggregate turns out to be not suitable for a specific application, the characteristics of the aggregate need to be changed by most likely adding another group of aggregates that has the right properties to compensate for the improper characteristics of the original aggregate. For this purpose, it is

important to be able to identify positive or negative properties of aggregate particles that can increase or decrease the strength of the structure in which they are used. However, since the indirect methods only permit the use of the overall characteristic (the combined result of aggregate shape, angularity, texture, gradation, etc.), it is not easy to pinpoint the specific property that needs to be either suppressed or replaced. In this case, the indirect methods will have to yield to direct particle measurement methods.

2.2 REVIEW OF RAPID PATICLE CHARACTERIZATION TECHNOLOGIES

2.2.1 Automated Sieve Analysis

One of the straightforward options in automating particle size gradation is to automate the industry-standard sieve analysis. One advantage to this technique is that it remains within the accepted practice of utilizing standard sieves of various mesh sizes to determine grain size distribution.

The Gradex 2000 Particle Size Analyzer (Figure 2.3), manufactured by Rotex Inc., and the Automatic Gradation Unit, manufactured by Pavement Technology Inc., are two examples of automated sieve analysis devices. Both devices automate the process of performing a sieve analysis from shaking a sieve stack to the calculation of grain size distribution from the cumulative weight retained on individual sieves. They incorporate a sieve shaker, an arm to empty the sieve into a cumulative weighing pan, a brush operated through air pressure to clean off the sieves, and an electronic scale. The process yields a particle size distribution curve on a personal computer coupled with the machine.

There are some drawbacks to using an automated sieving apparatus to rapidly characterize aggregates. First, no information on particle shape or surface texture is obtained with this technique. Second, the method works in a batch mode which is not a good approach for continuous sampling and analysis of aggregates. Finally, maintenance of the parts that physically contact with others is a potential problem. For example, sieves need to be replaced on a regular basis because they contact with aggregates.

Figure 2.3: Gradex 2000 automatic sieve analyzer (Rotex, Inc. 1997).

2.2.2 Fractionating Water Column

Another automated method of determining particle size distribution involves differentiating between settling times in a fluid, assuming that larger particles have proportionally larger mass. The basis for a fractionating water column is that particles will reach a terminal settling velocity in a medium (generally water) as the force due to their weight is counteracted by the force due to drag on the particle surface. Force due to weight is proportional to diameter cubed; whereas the force due to drag is proportional to diameter squared, thus as particle size increases the settling velocity increases.

An automated version of the hydrometer has been developed by Micromeritics Corporation and is called the SediGraph (Figure 2.4). This device can determine grain size distributions for particles between 0.1 and 300 μm (Coakley and Syvitski 1991). The SediGraph machine utilizes x-rays to detect the changing concentration with time of fine particles settling in an aqueous suspension. Analysis time is reduced through a controlled upward movement of the x-ray detector with time (Coakley and Syvitski 1991). Aljassar (1993) developed a prototype of a fractionating water column to determine gradations of particles ranging from .075 mm (no. 200 sieve) to 2.38 mm (no. 8 sieve). It involved a 1.6 m tall clear sedimentation cylinder with light sensing photocells used to measure light blockage from settling particles. The device can measure a grain size distribution that very closely matches conventional sieve analysis, after establishing empirical correlation to properly calibrate the setup.

Figure 2.4: SediGraph (Micromeritics Corporation 1999).

There are several disadvantages of applying this technique to aggregate characterizations. First, as in the case of automated sieve analysis, no information on particle shape or surface texture can be obtained with this technique. Second, a constant temperature must be maintained for measuring the settling velocity accurately. Third, particles larger than 2 mm are difficult to be measured because they do not have steady settling velocities as they instigate turbulent flow in the column. Finally, the water in the column must be changed when it gets cloudy.

2.2.3 Laser Diffraction

Used extensively in determining the homogeneity of fine powders and gels, laser diffraction analysis has recently been used to study fine soil gradation. This technique involves a laser directed through a gas or fluid suspension of particles to create a diffraction pattern of particle shadows. The resulting

diffraction pattern is interpreted using a combination of Fraunhofer and Mie light scattering theories (Agrawal et al. 1991).

Most laser diffraction equipment currently available is geared towards grading particles of much more uniformity than a typical soil. Nevertheless, Loizeau et al. (1994) and Buurman et al. (1997) have conducted studies to evaluate the potential of such devices to determine soil gradation. Buurman et al. (1997) concluded that laser diffraction cannot replace conventional sieving and hydrometer techniques as long as correlation between the methods have not been established for many different soils.

Several companies market laser diffraction equipment including CILAS and Beckman Coulter, Inc. The CILAS Model CILAS 940 (Figure 2.5) and the Coulter Model LS200 are reported to be capable of grading particles from approximately 0.5 μm up to 2 mm in diameter or particles in the medium sand range (Beckman Coulter 1999, CILAS 2000). As this particle size range indicates along with the above discussion, the laser diffraction technique has almost the same disadvantages as those of the fractionating water column method.

2.2.4 Digital Image Technology

Two-dimensional (2D) digital image analysis (DIA) appears to be the technology most often studied for automating the characterization of coarse aggregates. In this technique, images of particles obtained by a camera are digitized so that a computer can analyze the shape and size of each particle. To

extract size information from each particle from the digitized image, image segmentation and size measurement related algorithms are used.

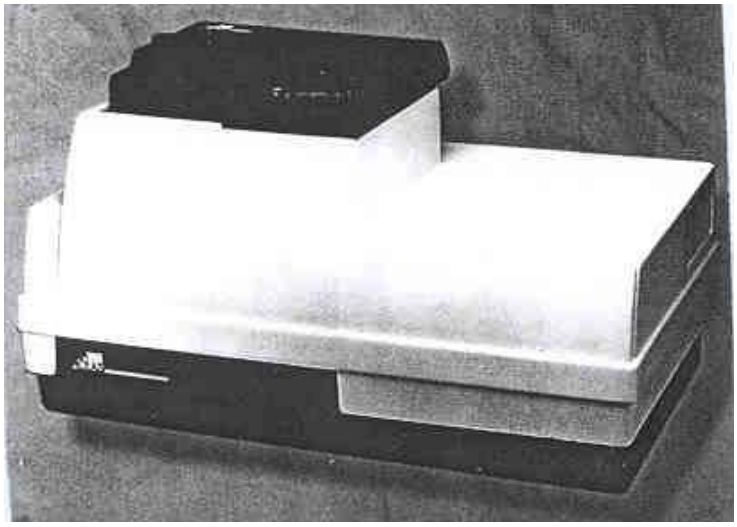

Figure 2.5: CILAS 940 laser diffraction device (CILAS 2000).

There have been many efforts to apply digital image analysis to characterization of particles. Kennedy and Mazzulo (1991) developed a semi-automatic image analysis system where the operator points to a particle on the computer screen and its size is automatically determined. Although this technique is more accurate than a completely automated system, it is more selective and therefore slower.

In Sweden, Fernlund (1998) used digital image analysis to show that particle form had a substantial influence on sieve analysis results. Also, Persson

(1998) used a scanning electron microscope to do image analysis of shape and size of fine aggregates. Persson sorted the sample into groups of similar size, scanning the groups at different magnifications, and found that sample preparation and segmentation methods are primary sources of error. The problems associated with measuring the distribution of widely differing sizes of particles have also been addressed by Dearnley (1985).

Several DIA based devices are commercially available for the determination of particle size distribution. With minor differences, all of these commercial machines rely on 2D DIA. In these devices, particles are arranged in a single layer and dropped in a controlled manner with the aid of a vibrating channel or chute. When these particles fall vertically, a shadow image of them cast by a backlight is obtained with either a linear Charge Coupled Device (CCD) scanning camera or a matrix CCD scanning camera. The particles' images obtained in this manner are processed to establish the principal dimensions and volume of each constituent using various algorithms. One of the most important assumptions in this technique is that particles' accurate volumetric information (which can convert to the weight based particle size distribution) can be extracted from the 2D image. A comprehensive review of commercially available grading machines can be found in Browne (2001).

Using digital image analysis to rapidly grade aggregates has the advantage of obtaining data on particle shape, and potentially texture, in addition to size. However, there are obstacles that need to be overcome to make this approach feasible. First, it is difficult to discern particles that are touching each other in

digital images. Second, it is necessary to separate particles to a degree before scanning. That is, some sample preparation may be needed to ensure that particles do not adhere to one another to form larger clumps. Third, analyzing a broad range of material sizes with a single camera setup is very challenging because a camera has a limited number of CCD cells. Finally, a sophisticated algorithm is needed to accurately convert the 2D data to 3D volumes and a weight-based gradation.

2.2.5 Laser Profiling

Laser profiling, also termed "structured lighting" or "active stereopsis", provides 3D data of an object's surface by illuminating the scene with patterned lighting such as stripes, dots, and color and by capturing the illuminated image. In a typical application, an active light source projects a light stripe onto the object's surfaces. A laser beam, or a focused beam of ordinary light, can be used as a source in this technique. The fact that lasers have parallel, monochromatic, and coherent characteristics has resulted in the widespread use of lasers as the lighting source.

Cheung and Ord (1990) made use of a light stripe projected onto the surface of rock fragments on a conveyor belt. Video images captured by a CCD camera were processed so that the 3D profile of the surface could be obtained by triangulation. However, it was reported that their final system not only could not detect particles smaller than 5 mm, but that it also produced results different from those given by manual screening (Dumitru et al. 1999).

One clear potential advantage of laser profiling is that far more accurate particle characterization is possible with the aid of the 3D data as opposed to 2D data. To illustrate how much difference the 3D measurement can make compared to a typical 2D image based approach, Figure 2.6 shows four regular shaped objects represented both in 3D and 2D manners. If the objects were scanned by the laser profiling, they would be represented as close to their actual sizes, shapes, and volumes as the resolution of the laser scanner allows (Figure 2.6 (a)). However, if they were scanned by a 2D camera from the above, then, no matter how good the resolution of the camera might be, they would all be represented as the same flat circle as shown in Figure 2.6 (b). That is, only one projected image of the object would end up being used, losing all other information. Therefore, it is natural that the four clearly different objects should have the same volume, size, and shape information in the 2D image approach. This is problematic not only in the determination of particle volume but also in measuring all other morphological properties of an object. For example, if shape or angularity of the object is to be measured in the 2D approach, one cannot choose but use the outline of the 2D circle, a small fragment of the entire particle information, which may lead to inaccurate analysis results.

Most of the difficulties mentioned previously regarding the application of 2D DIA to particle characterization also pertain to laser profiling because there exist many similarities between them such as using a camera as a data acquisition device. However, there exist unique disadvantages in laser profiling such as complex computational procedures necessary to handle the 3D data.

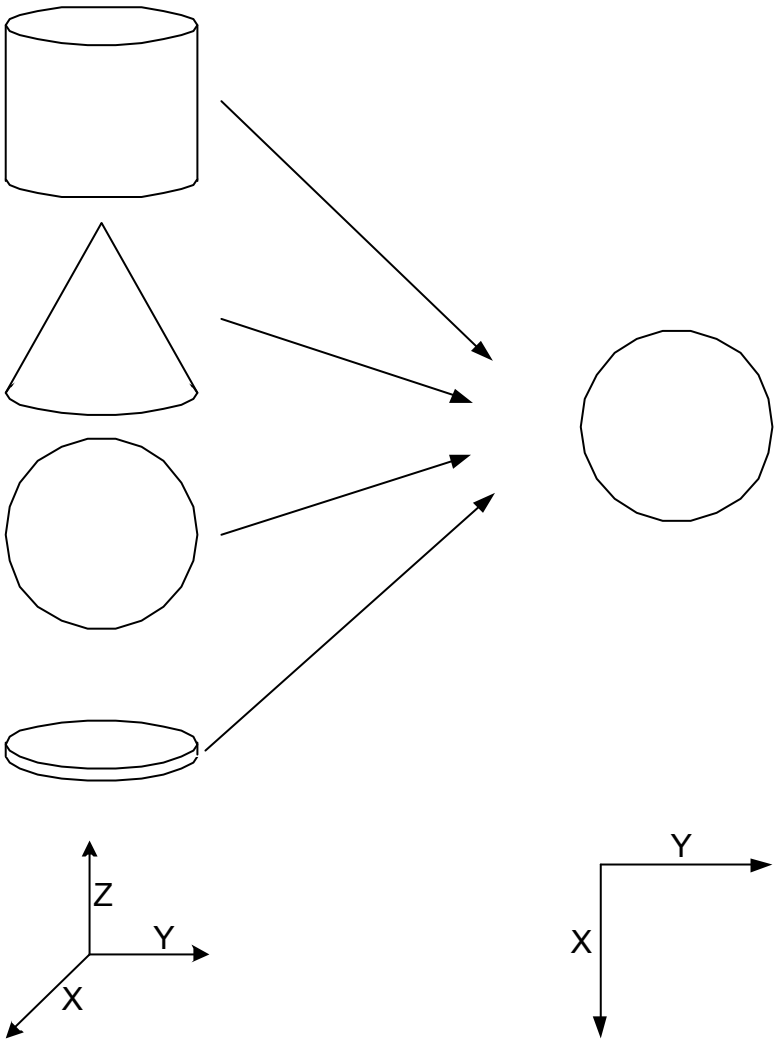

Figure 2.6: Comparison of 3D and 2D representations of regular shaped solids (a cylinder, a cone, a sphere, and a circular plate): (a) 3D representations; (b) 2D representation.

2.3 SELECTION OF BEST TECHNOLOGY FOR RAPID CHARACTERIZATION OF AGGREGATES

The Analytical Hierarchy Process (AHP) (Saaty 1980) was used to get expert input in order to choose the best technology through a systematic approach of selecting, weighting and applying criteria. All four members of the research team of the ICAR (International Center for Aggregate Research) project 503, "Rapid Test to Establish Grading of Unbound Aggregate Products" participated in this technology selection process. Laser profiling technology was divided into two different options: an off-the-shelf laser profiler and a customized laser profiler. This was decided because the two options could have huge differences in terms of cost, accuracy, etc. The AHP criteria for rapid characterization of aggregates can vary widely depending on the needs of the specific application. The criteria used in this research to judge the most promising technology include:

- *Accuracy and Reliability* – Demonstrated accuracy when compared to results from standard ASTM C 136 sieve analysis and ASTM D 4791 proportional caliper method, and reliability of results given variations in the material being processed (within the applicable range).
- *Processing period per sample* – The time required to acquire, prepare, and analyze a sample, then report data and clean-up for the next sample.
- *Applicable Range* – Ability to measure particles from a no. 8 mesh (2.36 mm) sieve to 50 mm in size.
- *Costs* – Initial equipment costs, maintenance and operation costs.
- *Shape* – Potential for measuring such characteristics as particle shape, angularity, and surface texture.
- *Degree of Automation* – Degree of operator intervention required, potential for continuous testing on a production line.
- *Material Preparation* - Degree to which material must be processed to separate particles, etc., prior to testing.
- *Robustness* – Likelihood that the test equipment could be designed to operate in an aggregate plant with little maintenance.

- *Potential for distributed deployment* – Adaptability to building a distributed network of scanning sensors at multiple locations in a production facility.

The AHP begins by weighing each criterion against each other using a Criterion vs. Criterion Matrix (Table 2.3). Reading across a row, each criterion is compared with the others designated by the column headings. Table 2.1 shows relative weighting values and their associated meaning for criteria comparison. For example, in Table 2.3 consider Accuracy and Reliability compared to Costs. Since it was felt that accuracy and reliability were weakly more important than cost, a weight of 3 is entered in row 1 (Accuracy and Reliability), column 4 (Cost). Each time a weight is recorded in a row cell, its reciprocal value is recorded in the corresponding column cell; thus in column 1, row 4, a weight of 1/3 is recorded. Next, each row is summed up, and the number is converted to a relative decimal value (criteria weighting). A criterion such as "accuracy and reliability" is considered to be more important in selecting the best technology method, as evidenced by a relatively high decimal value in the last column of Table 2.3.

Table 2.1: Weighting values for criteria comparison.

If row item is … as (than) column,	Weight number
Equally important	1
Weakly more important	3
Strongly more important	5
Very strongly more important	7
Absolutely more important	9

Next, in consideration of each criterion, the technology options are compared with each other by considering how likely each will be able to successfully fulfill the criterion. For each criterion, a matrix is created with all of the technology options on both the vertical and horizontal axes as shown in Tables 2.4 through 2.12. Table 2.2 shows the relative weighting values for technology comparison under each criterion. From this weighting, the relative decimal value (option rating) is obtained in the last column.

Table 2.2: Weighting values for technology comparison.

If row item is … as (than) column,	Weight number
Equally likely to satisfy criterion	1
Weakly more likely to satisfy criterion	3
Strongly more likely to satisfy criterion	5
Very strongly more likely to satisfy criterion	7
Absolutely more likely to satisfy criterion	9

Finally, overall ranking is performed by combining all criteria and technology options into a summary matrix. All criteria are listed on the horizontal axis (column headings), while all technology options are listed on the vertical axis. In each matrix cell, “criteria weighting” of each criterion is multiplied by the “option rating”, producing an “option score”. Each option score is added across all criteria for a row total. Then, each row total is divided by the grand total and converted to the final decimal value. The final results are tabulated in Table 2.14.

Table 2.3: Criterion vs. criterion.

	Criteria / Criteria	1	2	3	4	5	6	7	8	9	Row Total	Relative Value
1	Accuracy and Reliability	1	3	3	3	7	5	3	3	5	33.00	0.27
2	Processing period per sample	1/3	1	3	1	3	5	1	1	5	20.33	0.17
3	Applicable Range	1/3	1/3	1	1	1	3	1	1	3	11.67	0.10
4	Costs	1/3	1	1	1	1	5	3	1	3	16.33	0.13
5	Shape	1/3	1/3	1	1	1	3	1	1	1	9.67	0.08
6	Degree of Automation	1/5	1/5	1/3	1/5	1/3	1	1	1/3	1	4.60	0.04
7	Material Preparation	1/3	1	1	1/3	1	1	1	1	1	7.67	0.06
8	Robustness	1/3	1	1	1	1	3	1	1	3	12.33	0.10
9	Potential for deployment	1/5	1/5	1/3	1/3	1	1	1	1/3	1	5.40	0.04
									Grand Total		121.00	1

Table 2.4: Option vs. each criterion (accuracy and reliability).

	Accuracy and Reliability	A	B	C	D	E	F	Row Total	Relative Value
A	Automated Sieve Analysis	1	1/3	1	1/3	1	5	8.67	0.13
B	Laser Spectroscopy	5	1	3	1	3	5	18.00	0.27
C	Digital Image Analysis	1	1/3	1	1/3	1	5	8.67	0.13
D	Off-the-shelf Laser	3	1	3	1	5	7	20.00	0.30
E	Customized Laser	1	1/3	1	1/5	1	5	8.53	0.13
F	Water Column	1/5	1/5	1/5	1/7	1/5	1	1.94	0.03
						Grand Total		65.81	1

Table 2.5: Option vs. each criterion (processing period per sample).

	Processing period per sample	A	B	C	D	E	F	Row Total	Relative Value
A	Automated Sieve Analysis	1	1/5	1/9	1/7	1/7	1/3	1.93	0.02
B	Laser Spectroscopy	5	1	1/3	1	1/3	1	8.67	0.11
C	Digital Image Analysis	9	5	1	3	3	7	28.00	0.35
D	Off-the-shelf Laser	7	1	1/3	1	1	5	15.33	0.19
E	Customized Laser	7	3	1/3	1	1	5	17.33	0.22
F	Water Column	5	1	1/7	1/3	1/3	1	7.81	0.10
						Grand Total		79.07	1

Table 2.6: Option vs. each criterion (applicable range).

	Applicable Range	A	B	C	D	E	F	Row Total	Relative Value
A	Automated Sieve Analysis	1	7	5	7	5	5	30.00	0.39
B	Laser Spectroscopy	1/7	1	1/5	1/5	1/5	1/3	2.08	0.03
C	Digital Image Analysis	1/5	7	1	3	1	5	17.20	0.22
D	Off-the-shelf Laser	1/5	5	1/3	1	1	3	10.53	0.14
E	Customized Laser	1/5	5	1	1	1	1	9.20	0.12
F	Water Column	1/5	5	1/3	1/3	1	1	7.87	0.10
						Grand Total		76.88	1

Table 2.7: Option vs. each criterion (costs).

	Costs	A	B	C	D	E	F	Row Total	Relative Value
A	Automated Sieve Analysis	1	7	3	5	3	3	22.00	0.34
B	Laser Spectroscopy	1/5	1	1/5	1/3	1/5	1/5	2.13	0.03
C	Digital Image Analysis	1/3	5	1	3	1	1	11.33	0.17
D	Off-the-shelf Laser	1/5	5	1/3	1	1/3	1/3	7.20	0.11
E	Customized Laser	1/3	5	1	3	1	1	11.33	0.17
F	Water Column	1/3	5	1	3	1	1	11.33	0.17
						Grand Total		65.33	1

Table 2.8: Option vs. each criterion (shape).

	Shape	A	B	C	D	E	F	Row Total	Relative Value
A	Automated Sieve Analysis	1	1	1/7	1/9	1/9	1	3.37	0.03
B	Laser Spectroscopy	1	1	1/7	1/9	1/7	1	3.40	0.03
C	Digital Image Analysis	7	7	1	1/5	1/5	5	20.40	0.20
D	Off-the-shelf Laser	9	9	7	1	3	9	38.00	0.38
E	Customized Laser	9	9	5	1/3	1	7	31.33	0.31
F	Water Column	1	1	1/5	1/9	1/7	1	3.45	0.03
						Grand Total		99.95	1

Table 2.9: Option vs. each criterion (degree of automation).

	Degree of Automation	A	B	C	D	E	F	Row Total	Relative Value
A	Automated Sieve Analysis	1	1	1/5	1/5	1/5	1/3	2.93	0.04
B	Laser Spectroscopy	1	1	1/5	1/5	1/5	1	3.60	0.05
C	Digital Image Analysis	7	5	1	1	1	5	20.00	0.30
D	Off-the-shelf Laser	5	5	1	1	1	3	16.00	0.24
E	Customized Laser	5	5	1	1	1	5	18.00	0.27
F	Water Column	3	1	1/5	1/3	1/3	1	5.87	0.09
						Grand Total		66.40	1

Table 2.10: Option vs. each criterion (material preparation).

	Material preparation	A	B	C	D	E	F	Row Total	Relative Value
A	Automated Sieve Analysis	1	1	1/3	1/3	1/3	1/3	3.33	0.06
B	Laser Spectroscopy	1	1	1/5	1/5	1/5	1/3	2.93	0.06
C	Digital Image Analysis	3	5	1	1	1	1	12.00	0.23
D	Off-the-shelf Laser	3	5	1	1	1	1	12.00	0.23
E	Customized Laser	3	5	1	1	1	1	12.00	0.23
F	Water Column	3	3	1	1	1	1	10.00	0.19
						Grand Total		52.27	1

Table 2.11: Option vs. each criterion (robustness).

	Robustness	A	B	C	D	E	F	Row Total	Relative Value
A	Automated Sieve Analysis	1	3	1	3	1	3	12.00	0.27
B	Laser Spectroscopy	1/3	1	1/3	1	1	1	4.67	0.11
C	Digital Image Analysis	1	3	1	3	1	3	12.00	0.27
D	Off-the-shelf Laser	1/3	1	1/3	1	1	1	4.67	0.11
E	Customized Laser	1	1	1	1	1	1	6.00	0.14
F	Water Column	1/3	1	1/3	1	1	1	4.67	0.11
						Grand Total		44.00	1

Table 2.12: Option vs. each criterion (potential for deployment).

	Potential for deployment	A	B	C	D	E	F	Row Total	Relative Value
A	Automated Sieve Analysis	1	1	1/5	1/3	1/5	1	3.73	0.06
B	Laser Spectroscopy	1	1	1/5	1/5	1/5	1/3	2.93	0.04
C	Digital Image Analysis	5	5	1	3	1	5	20.00	0.30
D	Off-the-shelf Laser	5	5	1/3	1	1	5	17.33	0.26
E	Customized Laser	5	5	1	1	1	5	18.00	0.27
F	Water Column	1	3	1/5	1/5	1/5	1	5.60	0.08
						Grand Total		67.60	1

Table 2.13: Summary matrix (options vs. all criteria).

	Criteria (Weight) / Options	1	2	3	4	5	6	7	8	9	Row Total
		0.27	0.17	0.10	0.13	0.08	0.04	0.06	0.10	0.04	
A	Automated Sieve Analysis	0.13	0.02	0.39	0.34	0.03	0.04	0.06	0.27	0.06	
B	Laser Spectroscopy	0.27	0.11	0.03	0.03	0.03	0.05	0.06	0.11	0.04	
C	Digital Image Analysis	0.13	0.35	0.22	0.17	0.20	0.30	0.23	0.27	0.30	
D	Off-the-shelf Laser	0.30	0.19	0.14	0.11	0.38	0.24	0.23	0.11	0.26	
E	Customized Laser	0.13	0.22	0.12	0.17	0.31	0.27	0.23	0.14	0.27	
F	Water Column	0.03	0.10	0.10	0.17	0.03	0.09	0.19	0.11	0.08	
A	Criteria weight x Option Value	0.04	0.00	0.04	0.05	0.00	0.00	0.00	0.03	0.00	**0.16**
B	Criteria weight x Option Value	0.07	0.02	0.00	0.00	0.00	0.00	0.00	0.01	0.00	**0.12**
C	Criteria weight x Option Value	0.04	0.06	0.02	0.02	0.02	0.01	0.01	0.03	0.01	**0.22**
D	Criteria weight x Option Value	0.08	0.03	0.01	0.01	0.03	0.01	0.01	0.01	0.01	**0.22**
E	Criteria weight x Option Value	0.04	0.04	0.01	0.02	0.03	0.01	0.01	0.01	0.01	**0.18**
F	Criteria weight x Option Value	0.01	0.02	0.01	0.02	0.00	0.00	0.01	0.01	0.00	**0.09**
										Sum	1.00

Table 2.14: Conclusion.

Technologies	Value
Automated Sieve Analysis	**0.16**
Laser Spectroscopy	**0.12**
Digital Image Analysis	**0.22**
Off-the-shelf Laser	**0.22**
Customized Laser	**0.18**
Water Column	**0.09**

The assigned weights shown in Tables 2.3 through 2.12 were obtained by having all four members of the research team individually assign weights. This process began with a group discussion to clarify the definitions of the criteria and choices. The weights suggested for each item were averaged to resolve differences among the four evaluators. For example, if two of the weights were 3 and the other two were 7, the weight became 5. If two of the weights were 1 and the other two were 1/9, the weight became 1/5. If the average was exactly in the middle of two weight numbers, the weight became the larger one. For example, if two of the weights were 3 and the other two were 5, the weight became 5.

The AHP procedure formalizes selection of the "best" technology for the stated criteria. By selecting the various weights when comparing only two technologies with respect to one criterion, one is forced to focus on making a rational, unbiased judgment. The AHP procedure then leads to a ranked listing of best choices.

The result of the rankings ranged from a low of 0.09 for the fractionating water column method to a high of 0.22 for both digital image analysis and laser profiling (the customized laser profiler option). These conclusions seemed to be consistent with current research in the field, where most development efforts are centered around digital image analysis. Relatively less attention has been given to the use of a laser profiler, but the judgments indicated that this technology shows significant promise, especially in 3D measurement of morphological properties of aggregates. Since this research aimed to measure not only size parameters but also

other morphological parameters such as shape, angularity, and surface texture, laser profiling was chosen to acquire accurate 3D data of aggregates.

CHAPTER 3
LASER-BASED AGGREGATE SCANNING SYSTEM (LASS)

In an attempt to achieve accurate and rapid measurements of aggregate properties, a laser-based aggregate scanning system was developed (Figure 3.1). The Laser-based Aggregate Scanning System (LASS) is designed to provide maximum flexibility for the study of different lighting schemes, scanner velocities, and so on while repeatedly scanning the same field of aggregates spread out on a table. This chapter begins with the discussion of the laser profiling mechanism followed by a description of the hardware system architecture. Next, a 3D image creation method is introduced that is designed to store 3D particle data effectively without losing critical information.

Figure 3.1: The Laser-based Aggregate Scanning System (LASS).

3.1 THE LASER PROFILING MECHANISM

Figure 3.2 shows a simple representation of how laser profiling works. Laser profiling, also termed "structured lighting" or "laser triangulation", is similar to a passive stereo vision system with one of the cameras replaced by a laser source (Caspi and Kiryati 1998). With a laser source projecting a stripe on the surface of the object to be measured, a camera captures a digital image of the reflection on the image plane of the Charge Coupled Device (CCD). If the position and orientation of the laser source and camera are known, a laser plane can be defined geometrically and a mathematical line can also be defined that connects a point on the stripe of the object's surface with a CCD cell through the camera's focal point. Then, through the intersection of the laser plane and the image line, one 3D coordinate along the laser stripe on the surface of the object can be determined (Valkenburg and McIvor 1998). It is worth noting that the laser projection allowed this technique to avoid the correspondence problem in a passive stereo vision system, where it is not clear which point from one image corresponds to a point in a second image (Sonka et al. 1999). Collectively, the datum points along one stripe define a cross-sectional profile of the object; combining successive profiles then defines the three dimensional shape of the object's top surface.

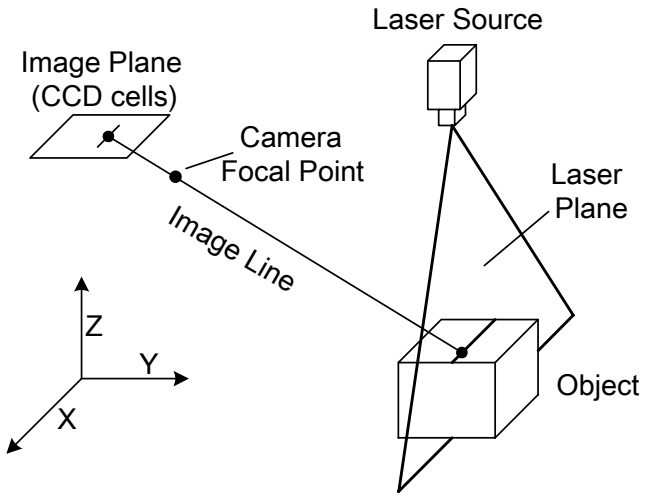

Figure 3.2: Schematic of laser profiling.

3.2 HARDWARE SYSTEM ARCHITECTURE

The LASS consists of a laser line scanner, a horizontal gantry system, and a personal computer (Figure 3.3). The laser scanner, which is mounted on the gantry system, passes over an aggregate sample, scanning it with a vertical laser plane. The laser line scanner can move approximately 1.5 m along the Y axis with a scan width of 120 mm and a scan height (Z axis) of 220 mm. Thus, anything that is within the range defined by the scanner travel distance, scan width, and scan height, can be scanned. From the accuracies of the horizontal gantry and the laser scanner, the LASS can also have resolutions of 0.3 mm, 0.1 mm, and 0.5 mm in X, Y, Z axes, respectively.

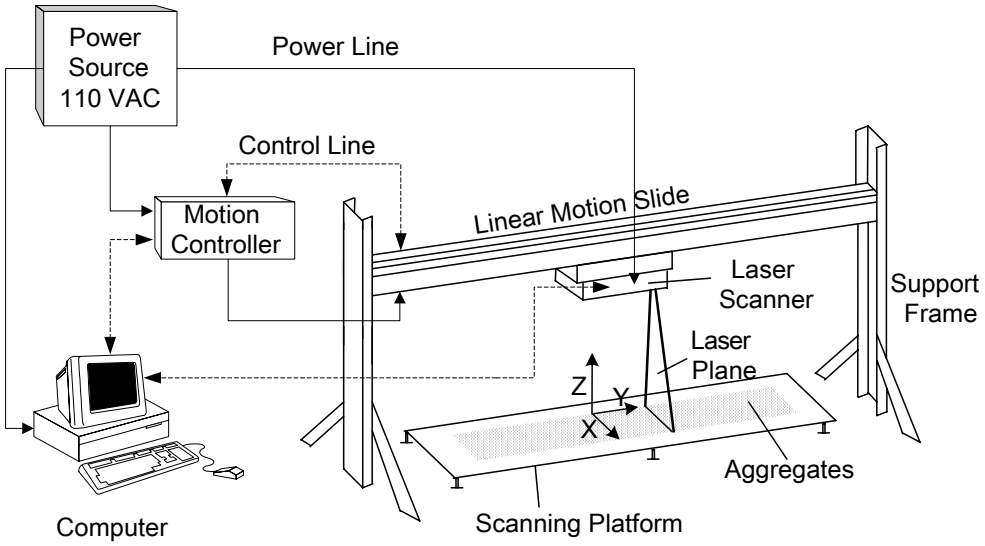

Figure 3.3: The LASS hardware architecture.

Detailed descriptions of the principal components are as follows:

- A computer-controlled, belt-driven, linear motion slide with a platform for mounting the scanner: This device is about 2.5 m long and can achieve controlled speeds up to 2.5 m/sec over a horizontal travel distance of about 1.5 m. The platform can move with an accuracy of 0.1 mm. This device was manufactured by Parker – Daedal Division.
- A laser line scanner: This scanner has a scan rate of 25 scans per second, scan width of 120 mm, scan height of 220 mm, 0.3 mm of X axis resolution, and 0.5 mm of Z axis resolution. This device was manufactured by MEL (Mikroelektronik GMBH, Germany).
- A personal computer: This computer is to interface with the scanning and motion control equipment.
- Customized software for integrated control of the linear motion slide and the laser line scanner: This software was written using the C++ programming language, LabView (a graphical programming language), the IMAQ Vision image processing tool, and the Wavelet and Filter Bank Design Toolkit. LabView, IMAQ Vision, and the Wavelet and Filter Bank Design Toolkit are all manufactured by National Instruments (Austin, Texas).

The scanner used for the LASS consists of a laser source and a camera in one unit. After an aggregate sample is spread across the scanning platform, the laser line scanner is passed over the sample to measure the profiles of the aggregate particles. Given the velocity of the scanner, relatively accurate shape data can be obtained by integrating the profiles.

The LASS has a 120 mm scan width, which means that as long as the aggregate particles are spread within that range, simultaneous scanning of multiple particles is possible. With a resolution of approximately 0.5 mm in three orthogonal directions, the LASS can scan 15 aggregate particles per second, assuming that the aggregate particles are less than 10 mm in their longest dimensions.

3.3 THREE-DIMENSIONAL (3D) IMAGE CREATION

3.3.1 Data Acquisition and Image Creation

The data acquisition routine in the LASS is composed of the following three subroutines:

- Linear motion slide control subroutine: This controls the motion of the linear motion slide platform, which is characterized by inputs describing the moving distance, speed, and direction.
- Laser scanner control subroutine: Using this subroutine, 566 height datum points are obtained from the scanner in every 1/25 second. A noise-canceling filter is used to eliminate excessively random noise in the raw data. This filter uses laser reflectance intensity as a criterion to evaluate the validity of each coordinate point. Invalid data are replaced by the base level value (zero height), and then examined and corrected using the non-linear filter and void filling process, which is described later.
- Subroutine for synchronizing scanning with the linear motion slide: This subroutine enables the scanner and the linear motion slide to start and stop

at the same time. Based on the amount of time that the linear motion slide is expected to operate, this subroutine calculates the number of scans needed to fill the travel distance. Through this subroutine, it is possible to obtain a uniform resolution in the data acquired along the direction of the scanner movement.

Because it is computationally more efficient to manipulate 2D data, it is beneficial to temporarily transform the 3D laser scan data into a 2D image format for some operations. Once the raw data are transformed into the "3D image", where the grayscale of each pixel represents the height of the datum point, conventional digital image analysis techniques can be applied. However, careful conversion from 3D raw data to 2D image format is required to prevent the loss of important data, with some adjustments of the raw 3D data required for true volumetric representations.

3.3.2 Image Adjustments and Corrections

In typical 2D digital image analyses, the horizontal (ΔX) and vertical (ΔY) physical dimensions of a pixel are constants. In the LASS data, however, the ΔX of each pixel is variable and depends on the pixel's height value (Z coordinate), while the ΔY is a constant determined by the scanning rate and the speed of the linear motion slide. Figure 3.4 (a) is a schematic that shows the scanning range and data points obtained with the laser scanner. Without adjustment, the resulting 3D image would be distorted along the X direction, as seen in Figure 3.4 (b), because of differences in the height of surface points in the image. To adjust for distortion and obtain an image like the one represented by Figure 3.4 (c), the following algorithm is used to adjust ΔX of each pixel:

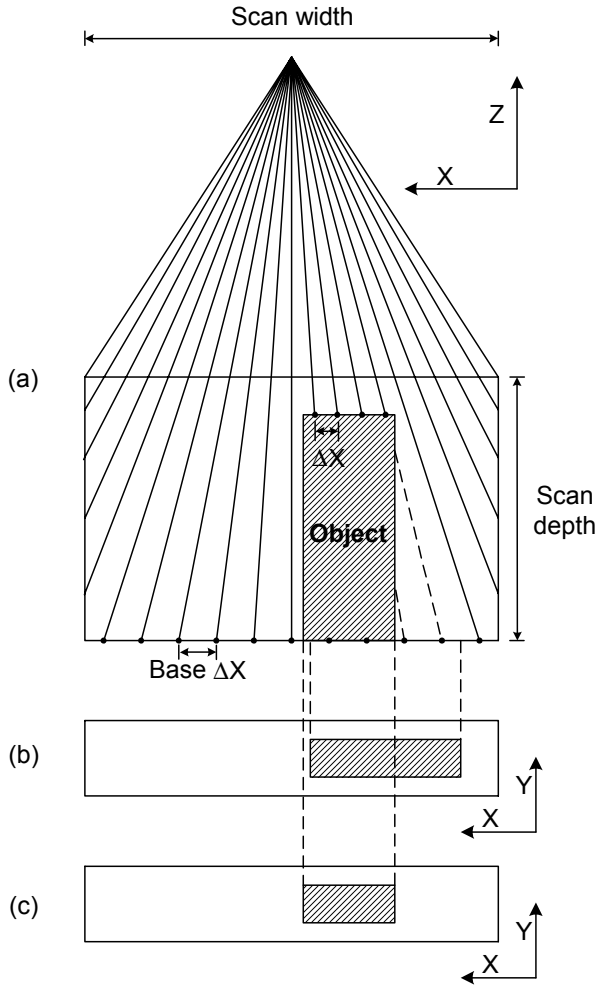

Figure 3.4: Effect of ΔX adjustment: (a) scanning range that shows different ΔXs depending on the heights of the datum points; (b) image of the object before ΔX adjustment; (c) image of the object after ΔX adjustment.

1. Calculate ΔX for the pixel assuming that there exists a linear relationship between the height and ΔX.
2. Calculate the difference between the calculated ΔX and the base level ΔX.
3. Calculate the X direction distance (number of pixels) of the pixel from the center of the image.
4. Multiply the difference in ΔX (calculated in step 2) by the X direction distance from the center (calculated in step 3).
5. Move the pixel toward the center of the image in the X direction by the number obtained in step 4.
6. If two adjacent pixels' adjusted locations have more than one pixel interval, the interval is filled with the grayscale value of the pixel that is located farther from the center than the other. This is to prevent the interval from being left unfilled with proper grayscale values.
7. Repeat steps 1 to 6 for all image pixels.

The ΔXs at a certain height are also variable, but the differences are negligible and it is assumed that all of the ΔXs at the same height are equal.

Since the data acquisition filter assigns a base level height value to invalid pixels, there can be some discontinuities in some regions of the image. Also, some noisy pixels that were not screened in the data acquisition process may exist in the grayscale image. To assign reasonable height values to the noisy pixels, a non-linear filter (Sonka et al. 1999) is used to assign the median height value of the

surrounding pixels. By choosing a proper number of neighboring pixels to consider, noisy data can be replaced by more reasonable height values.

CHAPTER 4
PARTICLE SEGMENTATION METHOD

In digital imaging of discrete particles, such as stone aggregates, segmentation is one of the most important processes. To accurately determine particle size and shape parameters, each particle region must be isolated and processed individually. Here, a method for segmenting a particle image acquired from laser profiling is developed using a Canny edge detector and a watershed transformation. Section 4.1 presents an overview of particle segmentation techniques while section 4.2 introduces the background relevant for the development of a particle segmentation algorithm including the Canny edge detector and the watershed transformation. Finally, section 4.3 presents the particle segmentation algorithm developed.

4.1 INTRODUCTION

Digital image analysis (DIA) is probably the most widely studied method for automated characterization of stone aggregate particles (Browne et al. 2001). In DIA, particle images are typically captured by one or more cameras, and the images are digitized and processed by computer to determine size distribution (gradation), shape parameters, and so on. In general, to determine gradation and shape parameters, each particle region in a digital image must be separated from the others so that the particle, or the region of interest (ROI), can be processed

individually. Without a robust segmentation technique, analyzing the data properly is almost impossible.

There are many ways of segmenting particles. Particles can be physically separated before they are captured in an image. In fact, several commercial grading devices that rely on 2D DIA utilize the natural separation of falling particles to minimize overlap. However, there are situations where this falling particle method is not feasible. For example, the camera or scanning device may not be fast enough to capture the falling particles. Moreover, while particles fall, they may tend to change orientation or rotate, an effect that may lead to inaccuracies. There also remains the potential for particles to overlap in a falling curtain arrangement.

Recently, three research efforts have applied computational particle segmentation to the area of civil engineering. Kemeny et al. (1993) developed a procedure for automatically segmenting rock fragments in 2D images. The procedure takes advantage of the background region between particles and the large grayscale differences that occur along the edges of touching fragments. Their algorithm analyzes the shapes of the background regions between particles and searches for large gradient paths in the region ahead of sharp convexities in the background region. That is, this method assumes that touching particles tend to form sharp convex regions that point in the direction of edges.

Wang (1998) developed an algorithm to separate touching aggregate in a binary 2D image. The algorithm first applied "polygonal approximation" to smooth particle boundaries on a certain scale and obtain significant concave

points. Second, the concave points were classified into different categories based on their probability of being part of the particle boundary. Lastly, the particle separation line was determined using a function in which a variable, such as shortest distance, is estimated from the identified concave points. Ghalib and Hryciw (1999) suggested watershed transformation, which will be explained later, as a way of segmenting soil particles in a digital image.

All three approaches were successful in their respective applications. However, none of them directly applies to images generated via laser profiling, which is being used to extract 3D particle information in this research. In many cases, it was found that touching particles in an image do not have sharp convexity or significant concavity. In addition, self-occlusion (Sonka et al. 1999), which can take place in laser profiling, makes the segmentation more difficult due to potential data loss.

4.2 BACKGROUND

This section reviews such image processing techniques as thresholding, convolution process, mathematical morphology, the Canny edge detector, and the watershed transformation.

4.2.1 Thresholding

If particles are spread in such a way that they do not touch each other in a digital image, a simple thresholding method can effectively separate particles. In

symbolic logic, a simple thresholding algorithm could be written as (Sonka et al. 1999):

$$IF \quad I(p) > Threshold \quad THEN \quad I(p) = 1 \quad ELSE \quad I(p) = 0 \tag{4.1}$$

where $I(p)$ is the grayscale level of pixel p, and $Threshold$ is a specified grayscale value. Unfortunately, physical separation of particles is often impractical. For instance, if particles were to be separated manually, the labor and time required would exceed the benefits gained from the automated system. On the other hand, sophisticated and costly machinery would be needed to perfectly separate every particle mechanically.

4.2.2 Edges in Digital Images

Since digital images are typically expressed as a 2D array of pixels with certain grayscale values, edges in digital images can be defined as pixels with grayscale values that are significantly different than those of their neighboring pixels. As a way of evaluating the grayscale differential, the following gradient operator (Sonka et al. 1999), which shows the rate of change in grayscale levels, can be used.

$$\nabla I(x, y) = \left(\frac{\partial I}{\partial x}, \frac{\partial I}{\partial y} \right) \tag{4.2}$$

where x and y are orthogonal coordinates, and I is the grayscale value of the pixel. However, a digital image is made up of discrete pixel values, so the gradient operator needs to be approximated as (Parker 1997):

$$\begin{aligned} \nabla_x I(x,y) &= I(x+1,y) - I(x-1,y) \\ \nabla_y I(x,y) &= I(x,y+1) - I(x,y-1) \end{aligned} \tag{4.3}$$

Then, the magnitude of the gradient is determined as (Sonka et al. 1999):

$$\left|\nabla I(x,y)\right| = \sqrt{\left(\frac{\partial I}{\partial x}\right)^2 + \left(\frac{\partial I}{\partial y}\right)^2} \tag{4.4}$$

Next, according to a specified threshold value, it can be determined whether the pixel is part of an edge. The direction of the gradient, which is perpendicular to the edge direction, is also determined as (Sonka et al. 1999):

$$\mathbf{n} = \frac{\nabla I}{\left|\nabla I\right|} \tag{4.5}$$

where $\mathbf{n}$ is a unit vector that represents the direction of the gradient. Figure 4.1 shows an image where the contour lines represent the same grayscale values. It is shown that gradient directions have 90° difference with edge directions.

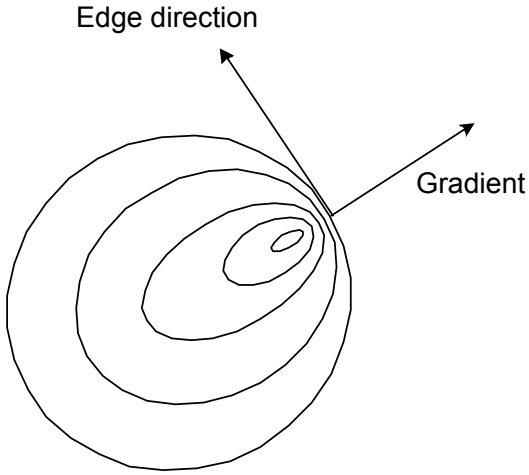

Figure 4.1: Edges in digital images.

4.2.3 Convolution and Gaussian Filter

The work of finding edges are conducted with a process called convolution (Sonka et al. 1999) defined as follows:

$$I'(x,y) = \int_{-\infty}^{+\infty} \int_{-\infty}^{+\infty} M(a,b) I(x-a, y-b) da db \tag{4.6}$$

where I' is a transformed image, M is a convolution mask or filter, I is an original image. This formula represents the idea of replacing all pixel values in the original image with a weighted sum of its neighbors. Each coefficient of a convolution mask is the weight which will be multiplied by its corresponding pixel value in the original image during the convolution process. Also, the size of

the convolution mask determines the size of neighborhood pixels that are included in the weighted sum. Figure 4.2 shows a convolution process where a 3 by 3 convolution mask is used to transform the original image. All the pixels in the image obtain new grayscale levels in the way the $I_{i,j}$ is transformed into $I'_{i,j}$.

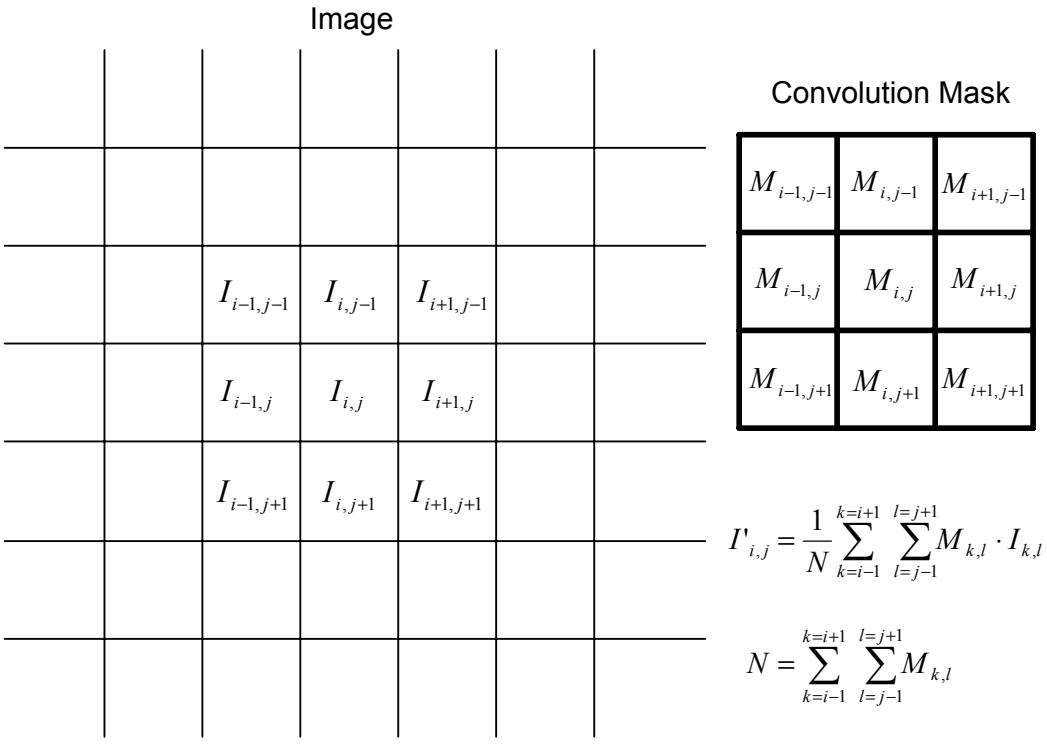

Figure 4.2: 2D convolution process.

A Gaussian filter (Sonka et al. 1999) is a type of convolution filter, which is generally used to suppress noisy pixels in an image. As the name, Gaussian,

indicates, the coefficients of the convolution mask have a normal distribution as shown in Figure 4.3. Thus, this method places bigger weights on the pixels that are close to the pixel of interest. This filter is represented as follows:

$$G = \exp\left(-\frac{x^2 + y^2}{2\sigma^2}\right) \tag{4.7}$$

4.2.4 Mathematical Morphology

Mathematical morphology (Dougherty 1993) in DIA refers to processes where the image is transformed based on non-linear algebra. Two basic morphological operations are binary dilation and erosion. Binary dilation means vector addition of two binary images of which pixel values are either 0 or 1. For example, if image X is the collection of pixels (0,0), (1,0), (0,1), and, (0,2), and image B is the collection of pixels (0,0), (0,1), then the transformed image X' is {(0,0), (1,0), (2,0), (0,1), (1,1), (0,2), (1,2)} as shown in Figure 4.4 (a). Mathematically, the dilation operator can be defined as (Sonka et al. 1999):

$$X \oplus B = \{p \mid p = x + b, x \in X \text{ and } b \in B\} \tag{4.8}$$

where p is a pixel that has horizontal and vertical coordinates, and $\oplus$ is the dilation operator. In contrast, the erosion operator means vector subtraction of two binary images. As shown in Figure 4.4 (b), when the two images are same as the above example, the transformed image becomes {(0,0)}. In mathematical morphology, the erosion operator can be defined as (Sonka et al. 1999):

1	1	2	2	2	1	1
1	2	2	4	2	2	1
2	2	4	8	4	2	2
2	4	8	16	8	4	2
2	2	4	8	4	2	2
1	2	2	4	2	2	1
1	1	2	2	2	1	1

(a)

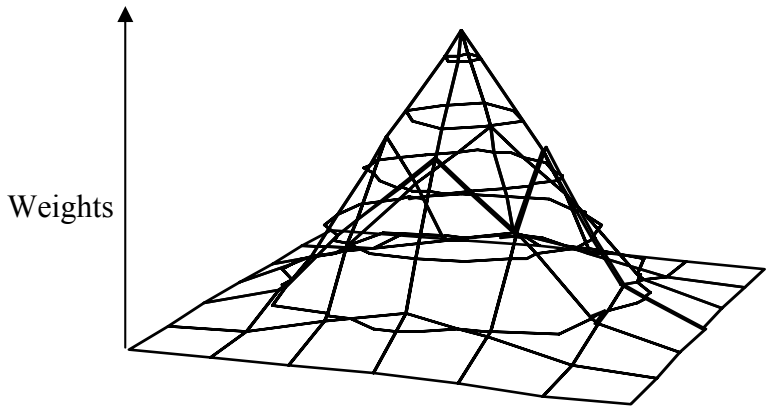

(b)

Figure 4.3: 7 by 7 Gaussian filter: (a) 2D representation; (b) 3D representation.

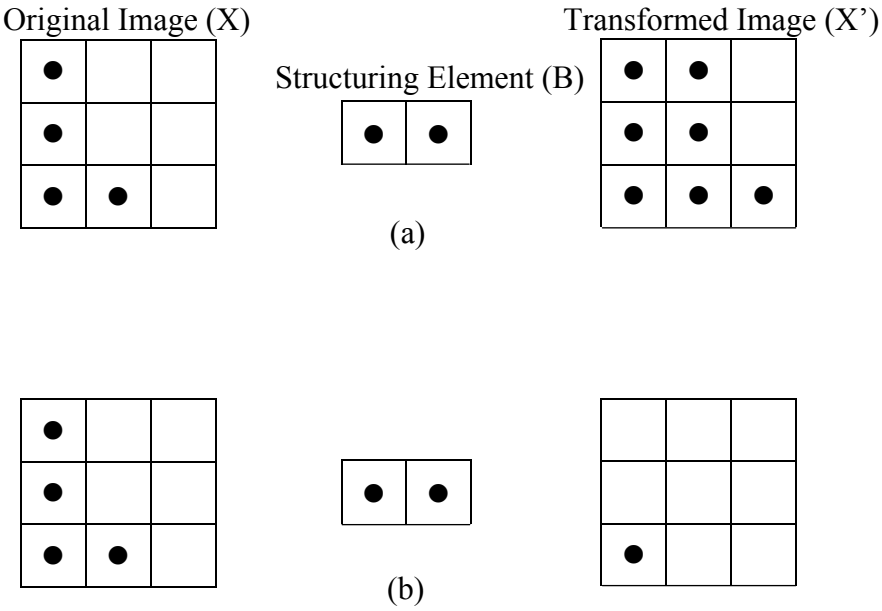

Figure 4.4: Mathematical Morphology: (a) binary dilation; (b) binary erosion.

$$X \Theta B = \left\{ p \in \varepsilon^2 \mid p + b = X, \text{ for every } b \in B \right\} \tag{4.9}$$

where Θ is the erosion operator. Since, depending on the shape of the small image B, various transforming effects can be made, image B is called the "structuring element". These binary dilation and erosion operators are effectively used to define the watershed transformation which is explained in the next section.

4.2.5 The Canny Edge Detector

Canny (1986) proposed the following three performance criteria to design a high-quality edge detector:

- Good detection: Important edges should be detected.
- Good localization: The location of the detected edge should be close to the true edge.
- Minimum spurious edges: Multiple responses to a single edge should be minimized.

Canny derived an edge detection filter based on the above three criteria, and found that the filter could be effectively approximated by the gradient of a Gaussian filter, expressed as:

$$G_n = \frac{\partial G}{\partial \mathbf{n}} = \mathbf{n} \cdot \nabla G \tag{4.10}$$

where G_n is the gradient of the Gaussian filter G. The gradient direction $\mathbf{n}$ can be estimated as:

$$\mathbf{n} = \frac{\nabla(G * I)}{\left|\nabla(G * I)\right|} \tag{4.11}$$

where * denotes convolution. The Gaussian convolution makes edges clearer by suppressing noise in the image. Since edge pixels can be considered to be local maxima in the image convolved with the operator G_n, the edge location can be found from the following equation:

$$\frac{\partial}{\partial \mathbf{n}} G_n * I = 0 \tag{4.12}$$

By substituting for G_n from Equation (4.10), Equation (4.12) becomes:

$$\frac{\partial^2}{\partial \mathbf{n}^2} G * I = 0 \tag{4.13}$$

Equation (4.13) shows that the edge location can be found by convoluting the image with the second derivative of the operator G in the direction $\mathbf{n}$. This operation is often called "non-maximum suppression" in the sense that pixels that are not local maxima are ignored. That is, a pixel can become an edge pixel if it has a larger gradient than its neighbors in the direction of the gradient. After the edge pixel is located, its magnitude is estimated as:

$$\left|G_n * I\right| = \left|\nabla(G * I)\right| \tag{4.14}$$

Given the pixel magnitudes from Equation (4.14), a specified threshold value can be used to determine whether or not each pixel is an edge. However, Canny suggested so-called "hysteresis thresholding" as an improved way of selecting edge pixels. Hysteresis thresholding has two threshold values: a high threshold value (T_H) and a low threshold value (T_L). Any pixel with a gradient larger than T_H becomes an edge pixel, and any pixel with a gradient larger than T_L that is connected to an edge pixel becomes an edge pixel. In other words, an edge line proceeds from the pixel that has a gradient higher than T_H in the gradient direction obtained from Equation (4.11), and ends when it meets a pixel that has a gradient lower than T_L. This procedure minimizes spurious edges. In this research, an off-the-shelf Canny edge detection routine in the IMAQ Vision image processing tool was used.

4.2.6 Watershed Transformation

Following the introduction of the watershed transformations by Beucher and Lantuejoul (1979), a lot of effort has gone into improving the performance of the method (Vincent and Soille 1991; Moga 1998; Pratikakis et al. 1999; Bleau and Leon 2000) and to apply it to various applications (Beucher 1991; Subers et al. 1997; Ghalib and Hryciw 1999). In the watershed transformation, digital images are considered to be topographic maps that have ridges or crest lines

dividing depressions or drainage areas. In this regard, grayscale images can be compared to 3D terrain mapping (Huber and Hebert 1999). The basic idea behind the watershed transformation is to use watersheds identified in the terrain map as boundaries that separate different regions.

In general, light-intensity based images, which are typically acquired from optical cameras, cannot be directly used with watershed transformations because they do not provide sufficient topographic relief as required to segment different regions. Therefore, to obtain images with good relief, either a gradient image or a distance map is typically used. While the gradient image is an image transformed by Equation (4.4), the distance map is an image made by a criterion of how far each pixel of a region of interest (ROI) is from other regions. For example, if the ROI is a circle and other regions in the image are background, the boundary of the ROI, (i.e., all the pixels that adjoin the background) will have a pixel value of 1. The closer the pixel is to the center of the ROI, the higher values it will have. This distance transformation (distance operator) is simply expressed using a binary erosion operator as (Sonka et al. 1999):

$$\forall p \in X, \quad D_X(p) = \min\{n \mid p \notin (X \Theta nB)\} \tag{4.15}$$

where X is the ROI, D_X is the distance function of the ROI X that designates the distance value of pixel p from other regions, n is 0 or a positive integer, B is a structuring element with one unit radius, and $X \Theta nB$ is the image transformed by the erosion operator n times with the structuring

element B. In other words, the distance transformation obtains the minimum number of erosions of the ROI X with the structuring element B that does not contain the pixel p.

Figure 4.5 (a) shows a distance map of a binary image of two touching particles. Figure 4.5 (b) is the cross-sectional view of Figure 4.5 (a) with distances shown as depths, where geographic concepts such as a catchment basin, regional minimum, plateau, and watershed are displayed. A catchment basin is a container that receives or holds water, and a regional minimum is the lowest part in the catchment basin. A watershed is then a line that divides two connected catchment basins. A technique suggested by Beucher (1991) called "immersion simulation" can locate watersheds in a digital image. Imagine that all regional minima are pierced, and the whole geographic surface is immersed into a lake at a slow constant speed. The water entering through the pierced holes will then start flooding the catchment basins. When the water in the two minima reaches the level of the plateau between the two catchment basins, the plateau will become inundated. Considering that the water levels will merge at the center of the plateau, it is reasonable to assume the location of merging as a border that divides the two adjacent regions.

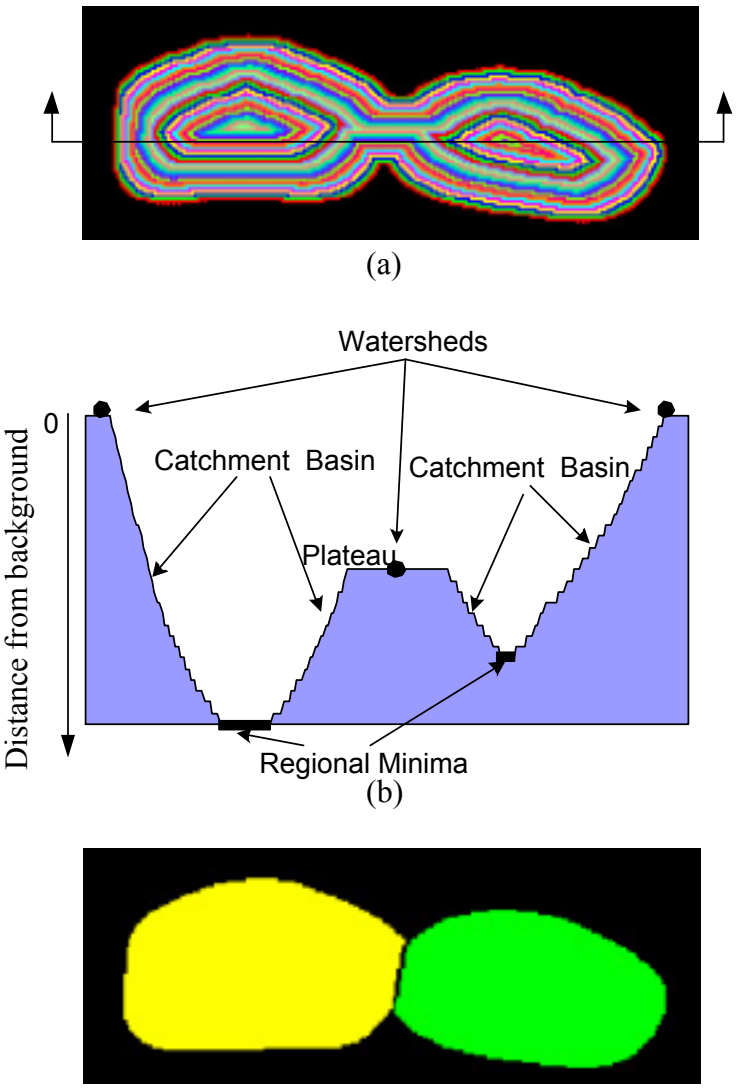

Figure 4.5: Watershed transformation: (a) distance map; (b) cross sectional view of the distance map (a); and (c) segmented image.

A regional minimum is defined with the introduction of a non-ascending path expressed as:

$$\forall p_i, p_{i+1}, \quad I(p_i) \geq I(p_{i+1}) \tag{4.16}$$

That is, if any two adjacent pixels in a specified path exist where the level of the first pixel is larger than or equal to that of the next pixel, the path is non-ascending. A regional minimum is then defined as pixels that do not have a non-ascending path starting from them.

Once regional minima are determined, watersheds can be found by the following algorithm expressed in the pseudo C programming code:

While (h = $h_{\max}$ to $h_{\min}$) {
    While (until $\forall p$ is filled where $I_D(p) == h$) {
        $\forall Z_i \oplus B$;
        Set $\forall p$ as Watershed where $D_{Z_i}(p) == 1$; } } (4.17)

where h is a pixel value, I_D is the transformed distance map, Z_i is a region connected to a regional minimum, $\oplus$ is the binary dilation operator, and D_{Z_i} is a distance operator of the ROI Z_i from other regions or the original background regions. This algorithm enables all of the identified regional minima to grow until they meet adjoining regions or the original background regions. In this research, the watershed transform routine was implemented using the C programming

language in conjunction with the distance map operator of the IMAQ vision image processing tool.

4.3 DEVELOPED SEGMENTATION ALGORITHM

Particle segmentation is a difficult and challenging process, especially when irregular materials like stone aggregates are the objects to be segmented. Since they vary greatly in terms of size, shape, and even surface texture, a systematic approach should be taken to obtain correct segmentation results. Moreover, in laser profiling, an algorithm needs to be incorporated into the segmentation method that recovers data loss that can be caused by self-occlusion, which is explained later in this section.

One way to increase the possibility of correct segmentation is to include as much useful information as possible. For example, while a distance map provides particle shape information, it does not show gradients of the image. On the other hand, while Canny edges are entirely relevant to the image gradients, they are not strongly related to particle shape. It is possible to obtain better segmentation results by combining these two non-redundant bits of information. In fact, this data fusion concept has been widely used as a way of reducing error in robotic and automated sensing systems. As an example, Haas (1990) integrated laser range data and video data for a fully automated road crack detection system.

To develop an effective segmentation method using a data fusion strategy, the following four criteria are first established:

1. Minimize over-segmentation: Minimize the situation where one particle is separated into multiple particles.
2. Minimize under-segmentation: Minimize the situation where multiple particles are grouped as one.
3. Minimize missing particles: Minimize the situation where a particle is erased during segmentation because the particle region does not have its own regional minimum.
4. Minimize incorrect border locations: Minimize the situation where a border between particle regions differs from where it should be.

The first three criteria relate to identifying appropriate regional minima so that only one regional minimum exists in a particle region. For example, if there are multiple minima in a particle region, this directly leads to over-segmentation. On the other hand, if there is only one regional minimum where multiple particles exist, under-segmentation or even particle loss can occur. As mentioned previously, regional minima are defined as pixels that do not have a non-ascending path. However, when this strict mathematical definition is applied to a digital image, too many or too few regional minima can be identified. Figure 4.6 (a) shows an example where two regional minima are located in a particle region. To avoid this situation, the idea of a search window with varying size is used.

In this method, the pixel of interest is compared with its neighboring pixels to determine whether it is a regional minimum or not. If the pixel's value is larger than any of its neighboring pixel values, it becomes a regional minimum. However, it remains a question of how to determine the appropriate size of the

search window. If the number of neighboring pixels (search window) is too large, under-segmentation can occur. Conversely, if the search window is too small, the possibility of over-segmentation increases. In the algorithm developed, as a reasonable way of determining the size of the search window, the pixel's height value is used. This approach can be expressed in symbolic logic as:

$$\begin{aligned} &IF\ (\ I_D(x,y) \geq \forall\ I_D(a,b)\ )\quad THEN\quad I_D(x,y)=1\quad ELSE\quad I_D(x,y)=0 \\ &\qquad \forall a \in [x-0.5\times(K\times H+C), x+0.5\times(K\times H+C)] \\ &\qquad \forall b \in [y-0.5\times(K\times H+C), y+0.5\times(K\times H+C)] \end{aligned} \tag{4.18}$$

where $I_D(x,y)$ is the distance value of the pixel (x,y), K and C are constants, and H is the height value of the pixel (x,y). That is, by using the search window of size $K\times H+C$, proper regional minima can be obtained. Figure 4.6 depicts examples where mathematical regional minima are ignored because of the selected search window.

The method of selecting regional minima by varying the size of search windows is a simple and effective method. However, it is easy to encounter a situation where the approach can lead to incorrect segmentation results. For example, if a particle is relatively flat, it is likely to have multiple minima because the search windows for the particle region will be smaller than needed, because the search window size depends on height data. On the other hand, if particles are densely grouped together and if the segmentation is based only on the distance map that is transformed from the binary image, then it may be difficult to extract accurate borders that correctly divide particles. These are why the edges detected

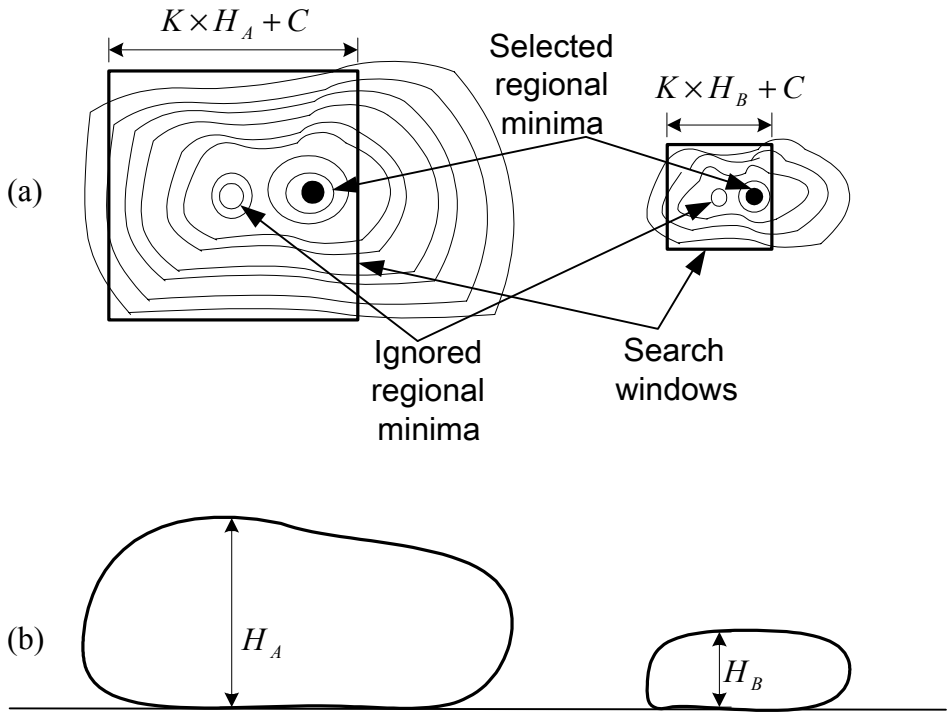

Figure 4.6: Method for finding appropriate regional minima: (a) distance map; (b) cross-sectional view showing heights of regional minima H_A and H_B.

by the Canny edge detection algorithm need to be fused with the watershed transformation.

The segmentation method developed in this section begins by first satisfying the fourth criterion by creating edges with the Canny edge detector with relatively rigorous high threshold value (T_H) and low threshold value (T_L). Since this rigorous standard is used, it is likely that only prominent grayscale discontinuities will be detected. Since it is also likely that the prominent gradients take place along the borders of touching particles rather than within a particle, the edge image is used to draw a rough outline of particles on the binary image that will be transformed into a distance map. This process can be expressed as:

$$IF\ (\ Canny_H(p) = 255\ ) \quad I_B(p) = 0 \tag{4.19}$$

where $Canny_H(p)$ is the value of pixel p in the edge image transformed by the Canny edge detector with relatively high T_H and T_L, 255 is the indication of an edge pixel in an 8 bit grayscale digital image, and $I_B(p)$ is the binary value of the pixel p in the binary image I_B obtained from thresholding the original grayscale image.

Second, to minimize over-segmentation, watersheds are compared with Canny edges detected with relatively low T_H and T_L. Since this generous standard is used, it is likely that almost all particle borders will be displayed in the edge image. Therefore, if there is a significant difference between the watershed and the Canny edge in terms of location, the watershed can be regarded as an

incorrect border that causes over-segmentation. Practically, this operation can be implemented as follows:

$$\begin{aligned} IF\ (\ \forall\ Canny_L(a,b) = 0\ ) \qquad & I_W(x,y) = R \\ \forall a \in [x - 0.5\times S, x + 0.5\times S] & \\ \forall b \in [y - 0.5\times S, y + 0.5\times S] & \end{aligned} \tag{4.20}$$

where $Canny_L(a,b)$ is the value of pixel (a,b) in the edge image transformed by the Canny edge detector with relatively low T_H and T_L, 0 is the indication of no edge, $I_W(x,y)$ is the pixel of interest of the watershed image, R is the identification value of any particle regions adjacent to the pixel, and S is the dimension of a search window. That is, if a pixel on watershed lines is close to the corresponding Canny edges, the pixel is considered to be on a real border. Otherwise, the pixel is allocated to any one of the adjacent regions, which results in merging of the different regions.

Figure 4.7 shows the overall flowchart of the segmentation algorithm. First, randomly spread particles (Figure 4.8 (a)) are scanned and thresholded into a binary image (Figure 4.8 (b)) using Equation (4.1). As seen in Figure 4.8 (b), several particles are connected, such that multiple particles appear as one. To draw rough particle outlines on the binary image, Canny edges (Figure 4.8 (c)) detected with a 5 by 5 Gaussian filter, and high T_H and T_L are used. After the "edge outlining" is conducted, the binary image is transformed into a distance map (Figure 4.8 (d)). This distance map is considered to be more representative of particle shapes than the one obtained directly from the binary image.

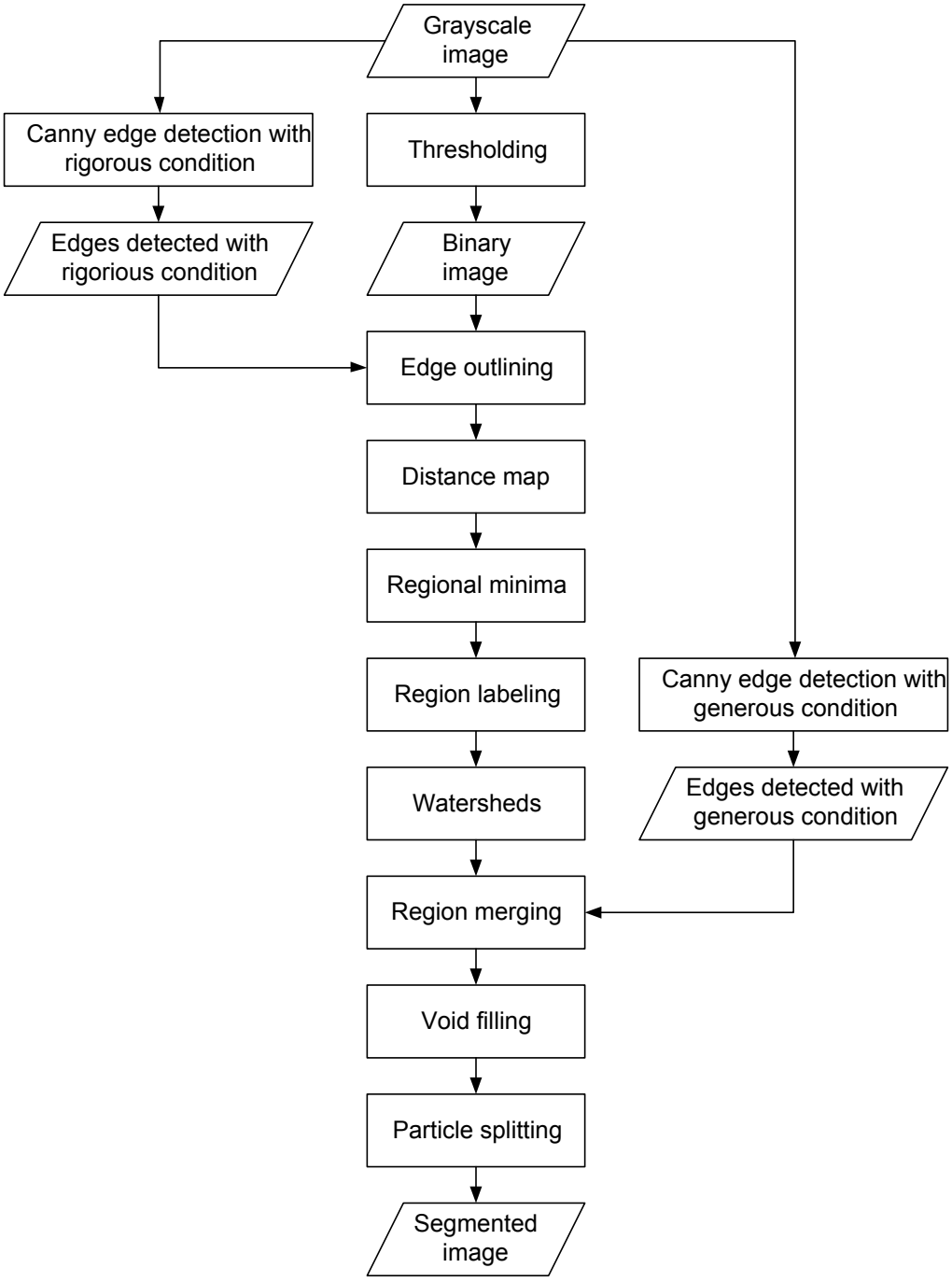

Figure 4.7: The segmentation algorithm developed.

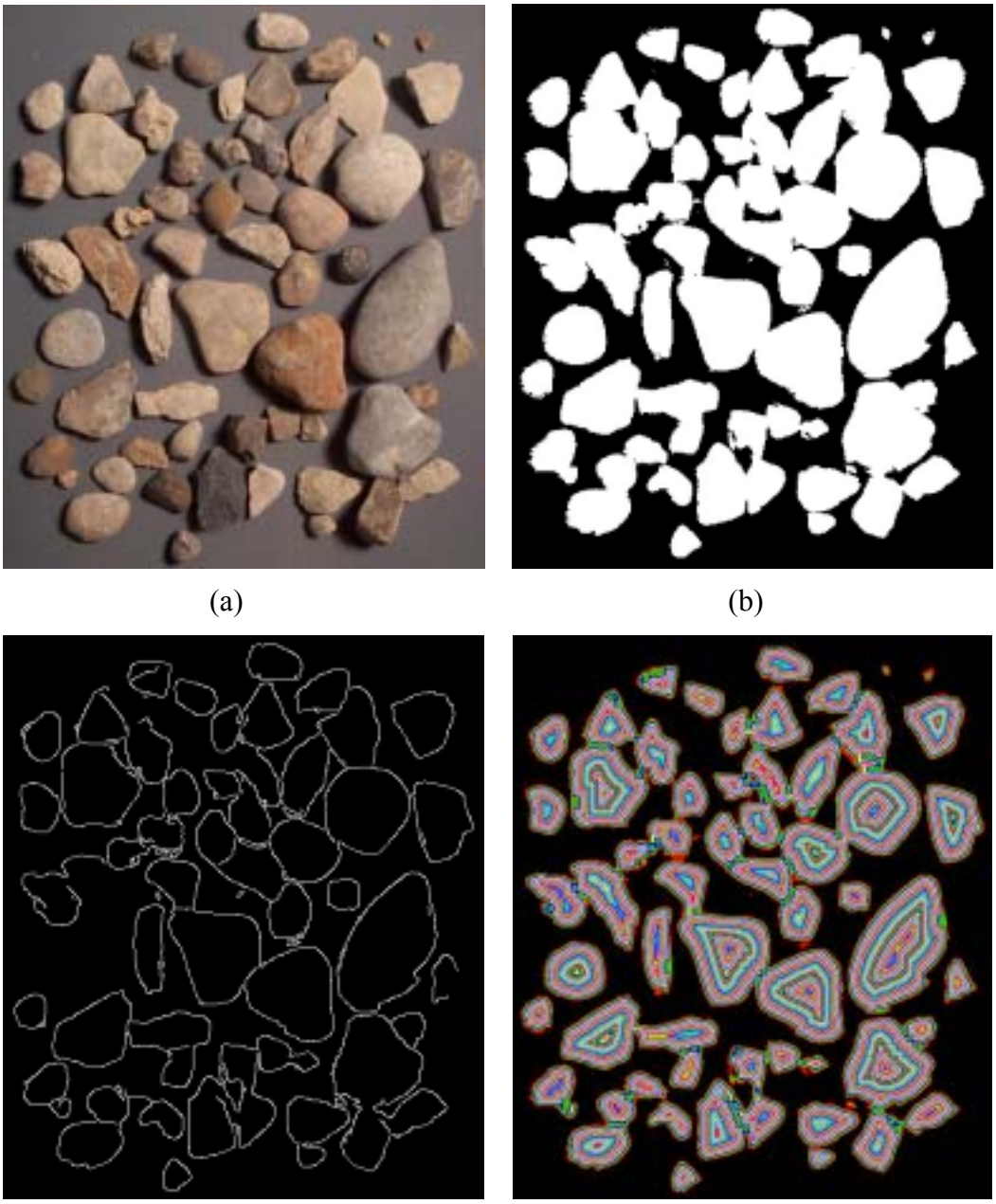

(a) (b)

(c) (d)

Figure 4.8: Images of each step of the segmentation method: (a) original particle picture; (b) thresholded image; (c) Canny edges with high T_H and T_L; (d) distance map.

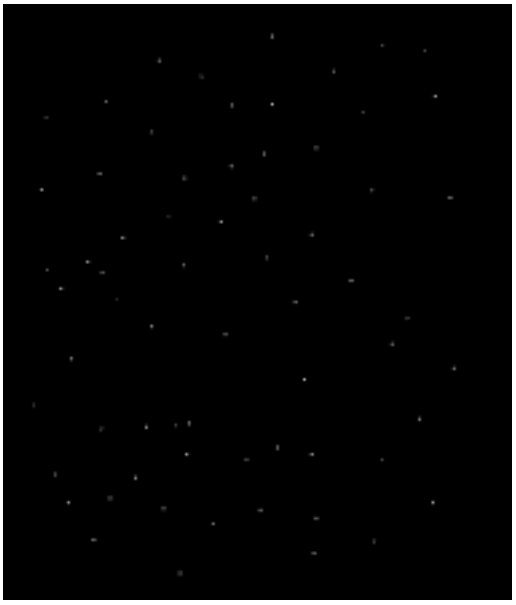

(e)

(f)

(g)

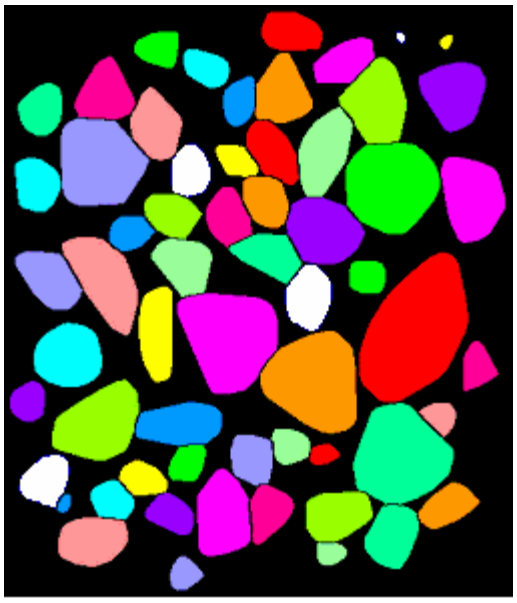

(h)

Figure 4.8 (Cont'd): Images of each step of the segmentation method: (e) regional minima; (f) segmented image with watersheds; (g) Canny edges with low T_H and T_L; (h) segmented image.

Subsequently, regional minima of the distance map are identified with the varying search window approach (Figure 4-8 (e)). As mentioned previously, the sizes of the search windows are determined based on the grayscale of the pixel of interest. Next, the regional minima are given unique labels by a region labeling process (Sonka et al. 1999), and they grow using a binary dilation process until they meet other regions including the original background regions in Figure 4.8 (b). When they meet other regions, the border becomes a watershed as shown in Figure 4.8 (f). Note that some of the particle regions are over-segmented. To check the validity of the watersheds, Canny edges are now detected with low T_H and T_L values (Figure 4.8 (g)). Through the comparison of the watersheds and the Canny edges, some over-segmented particle regions are merged.

After the region merging phase is finished, the particle void filling process starts. Figure 4.9 shows a situation where the reflected laser is blocked from reaching the image plane of the CCD cell detector by the shape and orientation of the object being scanned. If an object were a square pyramid with relatively steep slopes, as depicted in Figure 4.9 (a), the resulting grayscale image would be as shown in Figure 4.9 (b). This problem, called "self occlusion", is unavoidable with laser profiling, since the image plane and the laser source must be offset to provide sufficient accuracy. Even a short-range, single-axis laser ranging device will encounter this limitation, because this device uses the triangulation principle described earlier. To obtain Figure 4.9 (c), which is a more accurate 3D representation of the object, the void in Figure 4.9 (b) must be filled in a reasonable and robust manner. The void filling process marks the pixels that need

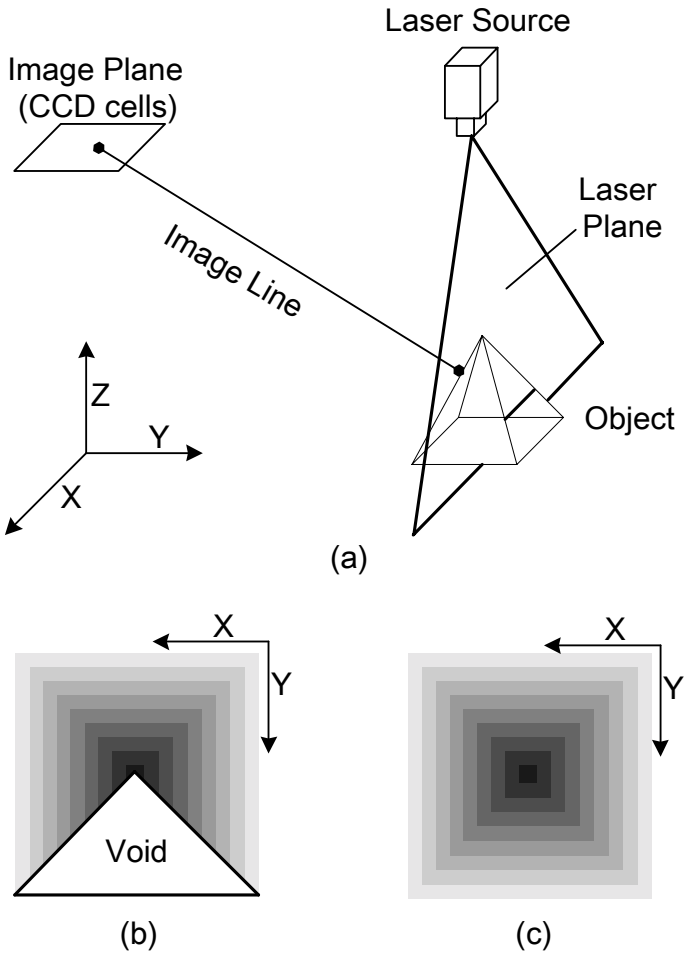

Figure 4.9: Self occlusion: (a) The situation where a reflected laser cannot reach the detector; (b) grayscale image of a square pyramid with an apparent void due to blocked laser reflections; (c) ideal grayscale image of the square pyramid.

to be assigned height values using a convex algorithm which creates the smallest region that contains the object, such that any two points of the region can be connected by a straight line, all points of which belong to the region (Sonka et al. 1999). As Figure 4.10 shows, compared to the actual particle image (Figure 4.10 (a)), the acquired binary image has artificial voids (Figure 4.10 (b)). To compensate for this, the voids are filled as in Figure 4.10 (c). However, since this void filling process can have an unintended effect on quantifying particle angularity and texture, for the application of wavelet-based particle descriptors in chapter 6, particles are scanned twice in opposite directions and the two images are merged to minimize the possible data loss.

Finally, after the void filling process, particle splitting follows. During the void filling process, it is possible for some particle regions to be expanded to the degree of meeting other particle regions. The particle splitting process separates the merged particles again by creating borders where two different particle ROIs meet. The completed segmented image is illustrated in Figure 4.8 (h). Comparing Figures 4.8 (a) and 4.8 (h), the algorithm appears to achieve reasonably correct segmentation. Comprehensive tests were conducted in conjunction with "virtual sieve" method, which is explained in the next chapter, in order to verify the validity of the segmentation algorithm and its assumptions.

(a) (b) (c)

Figure 4.10: Void filling: (a) original particle picture; (b) binary image before void filling; (c) binary image after void filling.

CHAPTER 5
VIRTUAL PARTICLE MEASUREMENT METHODS

This chapter presents particle measurement algorithms to produce analysis results comparable to those of the proportional caliper method (ASTM D 4791) and sieve analysis (ASTM C 136). Since the algorithms developed resemble the standardized methods in the way a particle is measured in a digital space, they are termed "virtual caliper" and "virtual sieve". Section 5.1 introduces previous research efforts to measure 3D particle shape. Section 5.2 then presents the virtual particle measurement and analysis methods developed given that a segmented particle image is now available by either the segmentation algorithm discussed in chapter 4 or a simple thresholding method. Experimental results and an evaluation are given in section 5.3.

5.1 BACKGROUND

A number of researchers have studied digital image analysis as a means of automating aggregate tests. Digital image analysis techniques usually rely on a single 2D image of each particle, where volume and thickness (the shortest dimension) are inferred from a 2D particle outline, as illustrated in Figure 2.6. Consequently, such systems cannot provide direct measurements of the three dimensions of an aggregate particle. To overcome this shortcoming in 2D digital image analysis different methodologies have been proposed.

Kuo et al. (1996; 1998) attached aggregate particles to transparent plastic trays with two perpendicular faces. After the initial projected particle images were captured, the sample trays were rotated 90° so that the particles were perpendicular to their original orientation. The dimensions of the aggregates in the new projected images were then captured and matched to the first orthogonal image. The longest, intermediate, and shortest particle dimensions obtained in this manner provide direct measures of the flatness and elongation ratio of the particles. Brzezicki and Kasperkiewicz (1999) used shadows of aggregate particles. With the particles placed on a special cylindrical carrier, a camera and two lighting sources were used to acquire an image of the perpendicular shadows of each particle. The perpendicular shadow images were processed to obtain the three principal dimensions of each particle.

Another approach for capturing 3D data involves the use of multiple digital cameras. Maerz and Lusher (2001) paraded individual particles on a mini-conveyor belt past two orthogonally oriented, synchronized cameras. Rao and Tutumluer (2000) also used particles on a conveyor belt, but employed three cameras. They argued that two camera images could miss important particle information that would lead to inaccurate assessments of shape for some particles. While both of these efforts were successful in capturing 3D data on particle shape, the scanning rate in these systems is limited by the need to arrange the aggregate particles in a single line, so that two or three images of a given particle can be taken simultaneously. In all cases, even when using three camera views, inferences must be made based on 2D projections of 3D objects.

In Sweden, Illerstrom (1998) and Tolppanen et al. (1999) built a device that can provide exceptionally detailed information on individual particles. They used a laser line scanner mounted on a three-axis coordinate-measuring machine. The particle being measured was flipped over manually to scan its underside. Although high-resolution data could be obtained with the scanner moving around a particle, considerable time and computing power were required to characterize just one particle with this system.

5.2 THE PARTICLE MEASUREMENT ALGORITHMS (VIRTUAL CALIPER AND VIRTUAL SIEVE)

The LASS particle measurement software architecture is outlined in Figure 5.1. The software converts the acquired data into a 3D image as discussed in Chapter 3, and various digital image processing algorithms are used to extract particle size and shape information from the image. Note in Figure 5.1 that before the image is segmented, the height data are stored separately. This is to preserve the height data essential to calculate volume and thickness of particles because the 3D grayscale image loses all its height data in the process of being segmented.

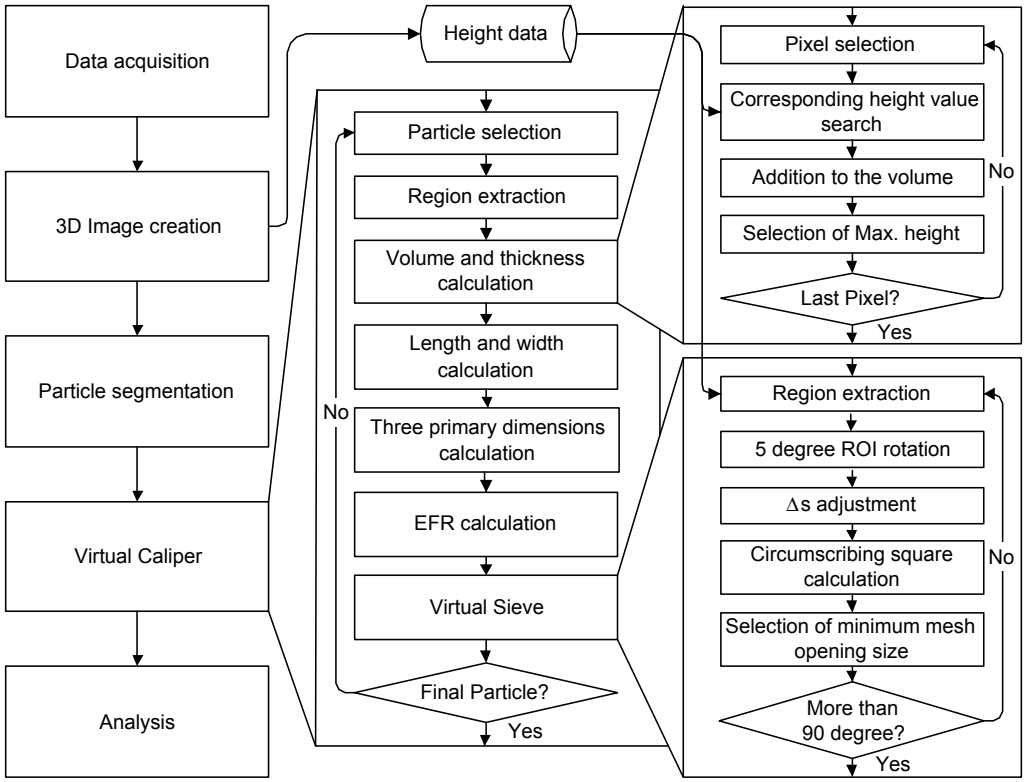

Figure 5.1: The LASS software architecture for the determination of shape and size parameters.

5.2.1 The Virtual Caliper

In the image segmentation process, the 3D image is segmented into particle regions with each particle being identified as a region of interest (ROI). The ROI data is used for length, width, and thickness measurements (Figure 2.1). An underlying assumption, which has been verified by manual inspection and the results presented later, is that particles overwhelmingly tend to fall flat when scattered on the scanning platform. Accordingly, the largest height value of the ROI can be considered as the thickness of the particle. Once the thickness is obtained, calculating length and width becomes a 2D problem. The assumption that the largest height value of the pixels that belong to the particle lying on the scanning bed corresponds to the particle thickness, conserves significant computing power because it transforms a 3D problem into a much simpler 2D problem.

First, the particle ROI is extracted creating a new image. The volume and thickness of the particle are then calculated using the previously stored height data. Next, the length and width of the particle are calculated by rotating the ROI incrementally to find the circumscribing rectangle with the smallest width. Finally, the three primary dimensions are reordered to find the longest, intermediate, and shortest dimensions in case the particle does not rest flat, and elongation and flatness ratios are calculated (Figure 2.1).

Just as one pixel corresponds to a unit square area in a 2D digital image, a volume element in a 3D image (called a “voxel”) corresponds to a unit volume. A pixel has an associated grayscale value whereas a voxel has a binary value. It is

either full or not full. Thus, calculation of the volume requires counting the number of full voxels that correspond to the particle ROI. The algorithm for the volume and thickness calculations is as follows:

1. Find the height value of each pixel in the particle ROI by referring to the stored height data. If the pixel is within a void as discussed in Chapter 4, use the height of the closest pixel in the horizontal X direction in the image. In this way, Figure 4.9 (c) can be inferred from the acquired image, Figure 4.9 (b). The search for the closest pixel is conducted only within the particle's ROI.
2. Multiply the pixel's height value in each full voxel by the unit volume of the voxel in mm^3 ($\Delta X \times \Delta Y \times \Delta Z$), and add the calculated number to the accumulated volume.
3. Compare the pixel's height value with the measured maximum height value so far. If the pixel's height value is larger than the maximum height value, it becomes the new maximum height value.
4. Repeat steps 1 through 3 for all pixels in the particle ROI. After all the pixels in the ROI have been considered, the accumulated volume and the maximum height value become the volume and the thickness of the particle, respectively.

As described in Chapter 2, the manual method for determining flatness and elongation ratios (ASTM D 4791) requires rotating each particle to determine whether the particle fits into the current caliper configuration. The LASS "length

and width calculation" algorithm simulates this manual procedure. One difference is that since the ΔX and the ΔY may be different every time the particle region is rotated, an updated ΔX and ΔY are calculated after each incremental rotation. The algorithm for length and width calculation is as follows:

1. Rotate the particle ROI by 5°.
2. Calculate the new ΔX and ΔY using the following formulae:

$$\Delta X = \frac{\Delta X_0 \cos\theta}{(\cos\theta + \sin\theta)} + \frac{\Delta Y_0 \sin\theta}{(\cos\theta + \sin\theta)} \tag{5.1}$$

$$\Delta Y = \frac{\Delta Y_0 \cos\theta}{(\cos\theta + \sin\theta)} + \frac{\Delta X_0 \sin\theta}{(\cos\theta + \sin\theta)} \tag{5.2}$$

   where ΔX and ΔY are the new ΔX and ΔY, respectively, ΔX_0 is ΔX at zero rotation angle, ΔY_0 is ΔY at zero rotation angle, and θ is the current rotation angle.
3. Find the circumscribing rectangle.
4. Calculate the width and length of the rectangle by multiplying the new ΔX and ΔY by the horizontal and the vertical pixel dimensions, respectively. If the width turns out to be longer than the length, they are interchanged.
5. Compare the rectangle's width with the minimum width measured so far. If the rectangle's width value is smaller than the minimum width, it becomes the new minimum rectangle width, and the length and the width are both stored. The new rotation angle θ is also stored in order to be used in the "virtual sieve" which is explained later.

6. Repeat steps 1 through 5 until the accumulated rotation angle is larger than 90°. Then, the selected minimum rectangle's dimensions become the width and the length.

5.2.2 The Virtual Sieve

If machine vision or laser imaging is used for gradation measurements, the data on a given particle must be analyzed to determine two parameters:

1. The smallest square mesh opening through which the particle could pass in any possible orientation.
2. The weight of the particle, which is generally computed from an estimate of particle volume and the average specific gravity of the aggregate material.

This correlation is depicted schematically in Figure 5.2. The smallest mesh opening through which a particle can pass is governed by the particle's smallest two dimensions, the width and thickness. Since the thickness information cannot be directly obtained in 2D DIA, correlation factors are generally used to make the results close to those of sieve analyses (Mora et al. 1998, Ghalib and Hryciw 1999).

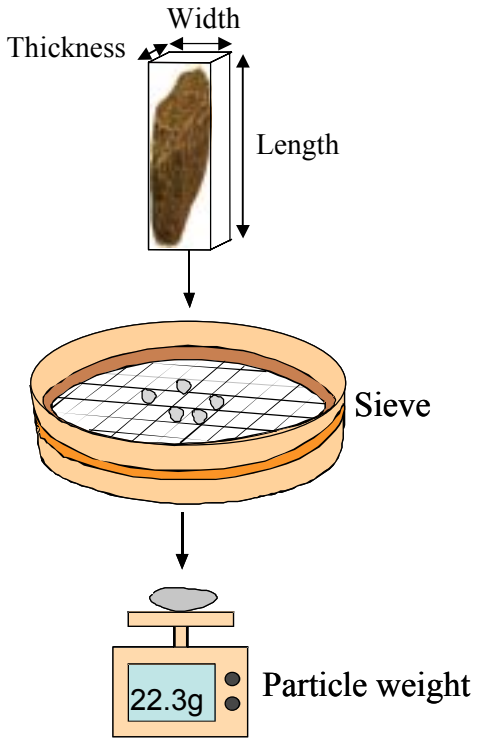

Figure 5.2: Relationship between the smallest two main dimensions of a particle and sieve data.

As illustrated in Figure 5.2, each particle's projected image along the longest dimension direction can be used to determine the equivalent sieve opening size through which the particle can pass. Just as the virtual caliper rotates the projected image of the particle along the shortest dimension's axis incrementally, virtual sieve analysis rotates the projected image along the length's axis. This approach conserves significant computing power again because it transforms a 3D problem into a far simpler 2D problem. The algorithm for the calculation of the equivalent sieve opening size is as follows:

1. Rotate the particle ROI by the stored angle θ in the virtual caliper process.
2. Calculate the new ΔX and ΔY using Equations (5.1) and (5.2), respectively.
3. Project all the height data, which were separately stored, of the ROI along the longest dimension direction creating a new binary image. Define the horizontal direction of the new image as the X direction, and the vertical direction as the Z direction.
4. Put a label on the particle region of the new projected image, identifying the region as a new ROI.
5. Rotate the new ROI by 5°.
6. Calculate the new ΔX and ΔZ using the following formulae:

$$\Delta X = \frac{\Delta X_0 \cos\theta}{(\cos\theta + \sin\theta)} + \frac{\Delta Z_0 \sin\theta}{(\cos\theta + \sin\theta)} \tag{5.3}$$

$$\Delta Z = \frac{\Delta Z_0 \cos\theta}{(\cos\theta + \sin\theta)} + \frac{\Delta X_0 \sin\theta}{(\cos\theta + \sin\theta)} \tag{5.4}$$

   where ΔX and ΔZ are the new ΔX and ΔZ, respectively, ΔX_0 is ΔX at zero rotation angle, ΔZ_0 is ΔZ at zero rotation angle, and θ is the current rotation angle.
7. Find the circumscribing square
8. Calculate the dimension of the square by multiplying the new ΔX or ΔZ by the pixel dimension of the square.

9. Compare the square's dimension with the minimum square dimension measured so far. If the square's dimension value is smaller than the minimum dimension, it becomes the new minimum square dimension.
10. Repeat steps 5 through 9 until the accumulated rotation angle is larger than 90°. Then, the selected minimum square's dimension becomes the equivalent mesh size.

However, in many cases a particle that cannot pass a certain mesh size in this computerized method can actually pass through that opening size in a slightly different orientation as shown in Figure 5.3. This is because the computerized method only uses projected images of particles, without attempting a complete random-vibration based sieve simulation for computational efficiency. The fact that particles' projected images rotate at every 5° interval instead of every 1° interval in the virtual sieve method also tends to make the equivalent sieve opening size a little bigger than the actual size. To correct for this effect, approximately 3000 particles were randomly selected from four different quarry sources (limestone river gravel, crushed traprock, crushed quartzite, and crushed granite), and their calculated equivalent mesh sizes were compared with those obtained from manual sieve analyses. A reduction factor (0.85), which was determined from these preliminary testing results, is used to estimate the actual mesh size through which the particle can pass.

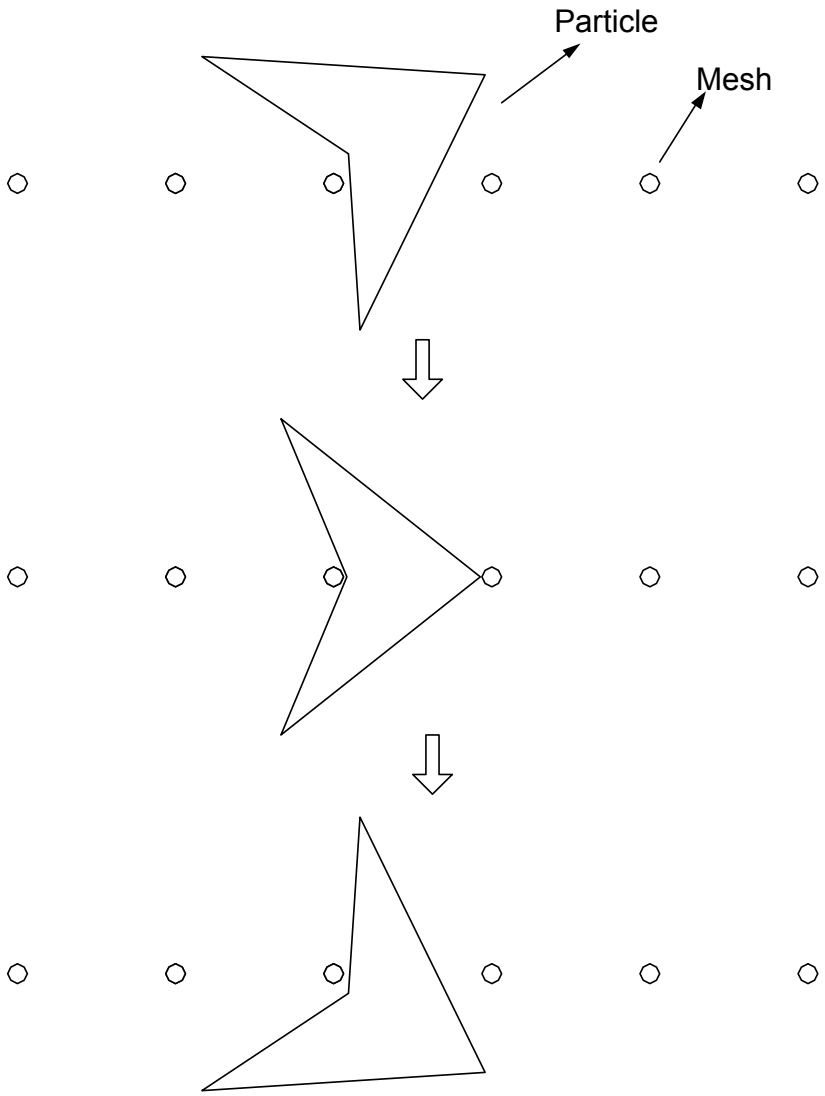

Figure 5.3: A particle passing through a mesh opening size by changing its orientation.

5.2.3 Analysis of Dimensional Ratios and Gradation

In Elongation and Flatness Ratio (EFR) and gradation tests, the percentage of particles in an aggregate sample that exceed or fall under a limiting ratio, or that fall under a size bracket is determined. To provide the weight-based information, which is preferred in both tests, the average specific gravity of the sample needs to be multiplied by each particle's volume. This is an attempt to match the results of the automated process with those of the standard methods. However, the volume-based representation of aggregates is more desirable because it provides a more rational indication of how aggregate particles interact with each other in three dimensions.

Figure 5.4 shows the relationship between measured and real volumes. The bottom of each particle cannot be scanned by the LASS, so the measured volumes ($A_U + A_D$ and $B_U + B_D$ in Figure 5.4) are larger than the real volumes (A_U and B_U in Figure 5.4). To obtain exact volumes, the hidden bottom portions (A_D and B_D in Figure 5.4) should be estimated and subtracted from the measured volumes. However, since only the particle percentage information is required in EFR and gradation tests, it is possible to characterize an aggregate sample without estimating the volume of the hidden part for each particle. This only requires the reasonable assumption that on average the volume of the hidden bottom of the particle is proportional to its actual volume, as indicated in Figure 5.4.

To illustrate, if an aggregate sample is divided into two groups, one with ratios larger than a:1 and the other with ratios smaller than a:1, the total measured volume can be expressed as follows:

$$V_M = \sum_{i=1}^{n} Va_{Mi} + \sum_{i=1}^{l} Vb_{Mi} \tag{5.5}$$

where V_M is the total measured volume, Va_{Mi} is the measured volume of particles with ratios smaller than a:1, and Vb_{Mi} is the measured volume of particles with ratios equal to or larger than a:1. If the two groups have almost the same proportion of hidden volume, the total measured volume can be expressed as follows:

$$V_M = (1+P)\sum_{i=1}^{n} Va_{Ri} + (1+P)\sum_{i=1}^{l} Vb_{Ri} = (1+P)\left(\sum_{i=1}^{n} Va_{Ri} + \sum_{i=1}^{l} Vb_{Ri}\right) \tag{5.6}$$

where Va_{Ri} is the real volume of particles with ratios smaller than a:1, Vb_{Ri} is the real volume of particles with ratios equal to or larger than a:1, and P is the average proportion of the particles hidden from the scanner. Consequently, the percentage of particles with ratios smaller than a:1 can be expressed with the measured volumes as follows:

$$\frac{\sum_{i=1}^{n} Va_{Ri}}{V_R} = \frac{\sum_{i=1}^{n} Va_{Ri}}{\sum_{i=1}^{n} Va_{Ri} + \sum_{i=1}^{l} Vb_{Ri}} = \frac{(1+P)\sum_{i=1}^{n} Va_{Ri}}{(1+P)\left(\sum_{i=1}^{n} Va_{Ri} + \sum_{i=1}^{l} Vb_{Ri}\right)} = \frac{\sum_{i=1}^{n} Va_{Mi}}{V_M} \tag{5.7}$$

where V_R is the total real volume. The validity of this assumption is verified in the next section.

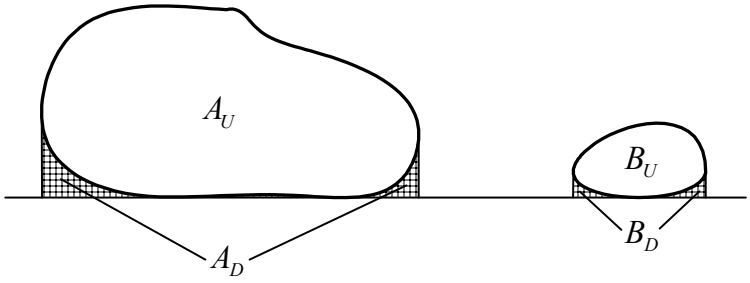

$$\frac{A_D}{A_U} \cong \frac{B_D}{B_U}$$

Figure 5.4: Depiction of the bottom portion of each particle (A_D and B_D) that is hidden from the laser scanner.

5.3 VERIFICATION

5.3.1 EFR Tests

To check the basic accuracy of particle dimensions determined by the laser scanner, a machined rectangular prism measuring 10 mm by 30 mm by 60 mm was scanned by the LASS. The observed errors in the determined longest, intermediate, and shortest dimensions were 3.0%, 3.3%, and -0.9%, respectively. The error in the measured volume was 0.01%. Note that the determination of the three primary dimensions of a particle requires finding the correct orientation for the smallest circumscribing rectangle. The search for this rectangle can introduce

some additional error into the LASS measurements, which probably explains the larger error associated with the measured longest and intermediate dimensions of the machined rectangular prism in this test.

To verify the applicability of the LASS results, a collection of stone particles were measured with a vernier caliper so that the LASS results could be compared with direct manual measurements. Altogether, 200 particles were numbered and measured, each with a longest dimension between 7 and 26 mm. The number of particles was selected to yield statistically valid results given that some variability, related to the positioning and orientation of particles in a particular scan, is expected. To get test samples with a range of particle colors and surface textures, aggregates were procured from four different quarries located across the United States. From each source, fifty particles were randomly selected to obtain a total of 200 particles. The four different aggregate sources and a description of the general characteristics of each material are given in Table 5.1.

Table 5.1: Summary of the shape characteristics of the tested particles.

Particle No.	Source	Description	Longest dimension (mm)			Shortest dimension (mm)		
			MAX	MIN	AVE	MAX	MIN	AVE
1~50	CA	Angular, medium gray granite with some black and white particles	23.74	8.83	14.09	8.98	4.08	5.98
51~100	SD	Very light red, angular quartzite	18.55	7.39	11.55	9.60	3.12	5.52
101~150	TX	Natural river gravel – various types of angular and rounded material	25.73	7.18	11.92	8.40	2.57	5.27
151~200	VA	Angular, dark gray traprock	23.26	8.81	14.74	9.12	3.22	5.62

To manually measure the three primary dimensions of each particle, the vernier caliper shown in Figure 2.2 (a) was used. The caliper had a 0.025 mm precision. Although these vernier caliper measurements are reasonably accurate, the 200 particles were also measured with the proportional caliper shown in Figure 2.2 (b) to permit direct comparisons with the standard ASTM D 4791 method. Measurements of the 200 particles with the vernier caliper required approximately four hours (approximately 50 particles per hour), with the aid of a computer spreadsheet program to calculate the elongation and flatness ratios. In comparison, measurements with the ASTM standard proportional caliper took four and a half hours.

To obtain a direct measurement of particle volume, a graduated cylinder with 0.1 ml (100 mm^3) divisions was used. Each particle was submerged in water in the cylinder to obtain the particle volume from the volume of displaced water.

Approximately seven hours were required to measure the 200 particle volumes in this manner.

After the manual measurements were completed, the 200 numbered particles were randomly spread on the LASS scanning bed, with some adjustments to ensure that no two particles touched one another. The particles were then scanned with the LASS and the data were processed using the virtual caliper method. Note that in this EFR test, the 3D image was segmented using a simple thresholding method because the particles were already well separated manually. The resolutions for the X, Y, and Z directions were 0.3 mm, 0.3 mm, and 0.5 mm, respectively. It took 70 seconds to scan all 200 particles, and 40 seconds to calculate elongation and flatness ratios (approximately 6000 particles per hour). Hence, the LASS device was approximately 150 times faster than the manual measurements with the ASTM D 4791 proportional caliper for this example.

Correlation analyses were then conducted to see how the LASS results compared to the manual measurements for the 200 test particles. Correlation coefficients obtained by correlation analyses show the degree to which two variables are linearly related. For example, if a correlation coefficient is 1, it means that there exists perfect positive linear relationship between the two variables, whereas a coefficient of zero means that there is no relationship between the two variables (Cangelosi et al. 1983). Comparisons of the three primary dimensions, elongation ratio, flatness ratio, and volume are shown in Figures 5.5 to 5.8. The correlation coefficients for the longest, intermediate, and

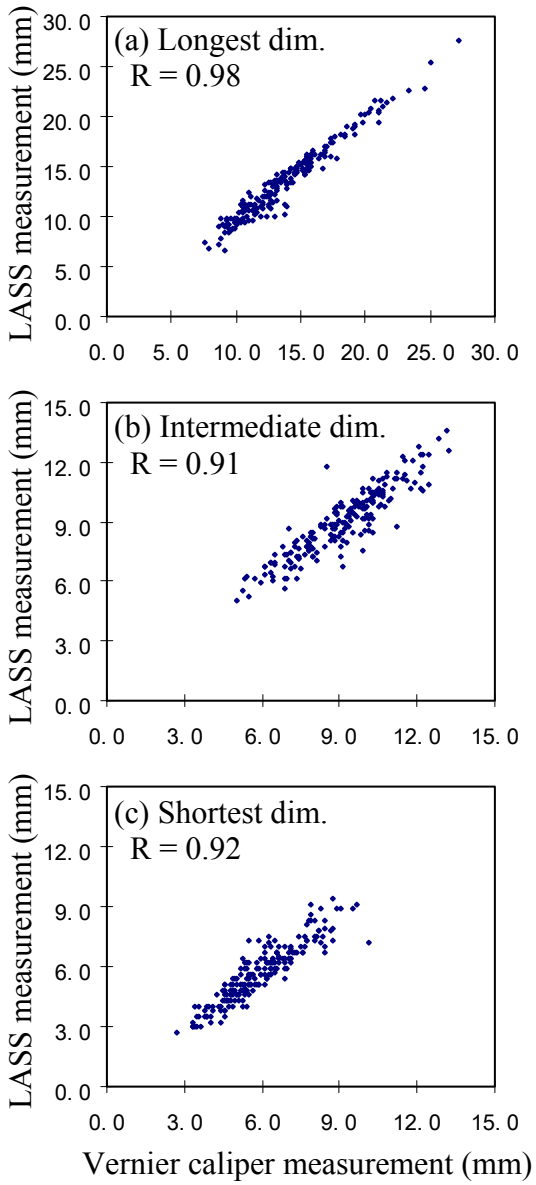

Figure 5.5: Comparison of the three primary dimensions measured manually and with the LASS (N = 200): (a) longest dimension; (b) intermediate dimension; (c) shortest dimension.

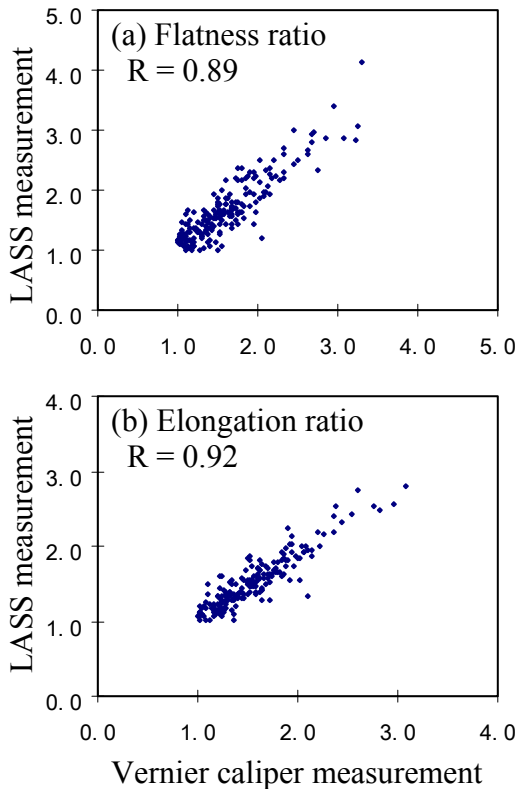

Figure 5.6: Comparison of the dimensional ratios measured with the vernier caliper and with the LASS (N = 200): (a) flatness ratio; (b) elongation ratio.

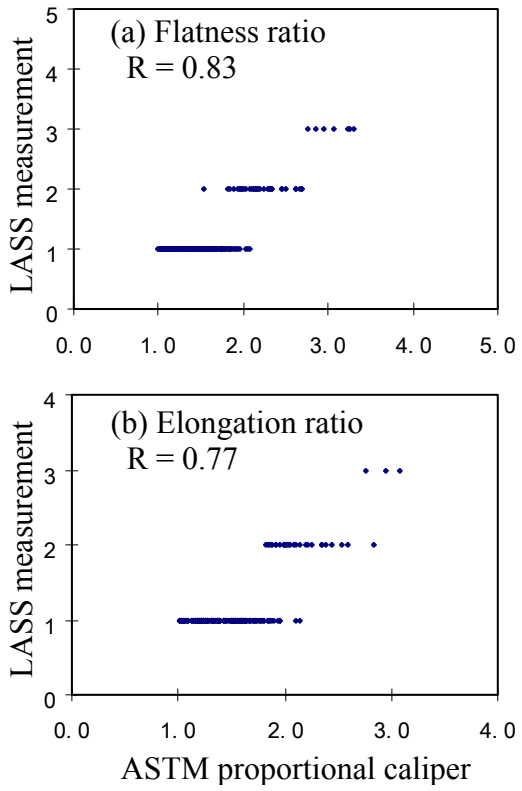

Figure 5.7: Comparison of the dimensional ratios measured with the ASTM proportional caliper and with the LASS (N = 200): (a) flatness ratio; (b) elongation ratio.

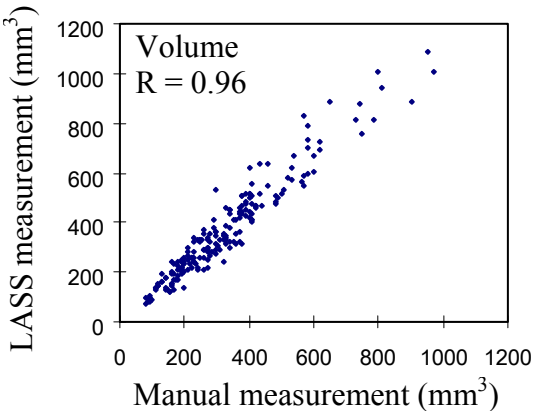

Figure 5.8: Comparison of the volume measurement between the manual process and the LASS (N = 200).

shortest dimensions were 0.98, 0.91, and 0.92, respectively (Figure 5.5). All three statistics show that there exists very strong correlation between the vernier caliper and the LASS measurements. Note that the correlation for the longest dimension is relatively higher than for the intermediate and shortest dimensions. This result was unexpected considering that, for the machined prism, the measurement error was the lowest for the shortest dimension. One possible explanation for this may be that it is more difficult to manually measure the intermediate and shortest dimensions of a particle than to measure the longest dimension. Consider that one must visualize the smallest rectangular prism that circumscribes the particle before measuring the three primary dimensions by hand. In the manual measurements, the technician typically measures the longest dimension of the particle first, and then tries different orientations to measure the intermediate and shortest dimensions. In rotating the particle, the circumscribing rectangular prism originally visualized by the technician may become skewed, which will lead to errors in the measured intermediate and shortest dimensions. In other words, the measurement error may reside with the technician rather than the LASS.

The flatness ratios and elongation ratios obtained from the LASS also correlated strongly with the manual measurements. As seen in Figure 5.6, the correlation coefficients based on the vernier caliper measurements were 0.89 and 0.92 for the flatness ratios and elongation ratios, respectively. The correlation for the flatness ratio is relatively lower because the measured intermediate and shortest dimensions, which had the slightly lower correlation than the measured longest dimension, are used to calculate the flatness ratio.

In comparison, the LASS measurements of the flatness and elongation ratios correlated relatively poorly with the ASTM proportional caliper measurements, as indicated in Figure 5.7. This is expected because the proportional caliper provides data only on selected, limiting ratios, and does not directly determine the actual dimensional ratios of each particle.

As can be seen in Figure 5.8, the volume measurements obtained from the LASS correlate strongly with the manual measurements (correlation coefficient of 0.96). As mentioned previously, the graduated cylinder that was used for the manual volume measurements had 100 mm^3 (0.1 ml) divisions. Considering that the average volume of the 200 particles was 325 mm^3, the precision of these manual measurements are fairly low, which should contribute to a significantly lower correlation. However, the comparatively strong correlation observed for the volume measurements may result from the fact that there is no need to find a virtual circumscribing rectangular prism, a requirement that makes it more difficult to accurately assess the primary particle dimensions.

In addition, the strong correlation with the manual measurements of particle volume provides strong support for the appropriateness of the assumption made with regard to the hidden bottom portion of each particle. As discussed in reference to Figure 5.4, the LASS algorithm assumes that every particle has approximately the same proportion hidden from the scanner. If this assumption were not valid, the strong correlation in the volume measurements would not have been obtained.

From the particle shape data obtained, a variety of statistics can be calculated to express the shape characteristics of an aggregate sample. For example, the percentage of particles whose flatness ratios are larger than 5:1 can be calculated. Also, the percentage of particles whose flatness ratios are between 5:1 and 4:1 can be obtained. However, the true nature of the shape characteristics of the sample can be best represented by a continuous ratio curve. Figures 5.9 show examples of a continuous flatness ratio curve (a) and a continuous elongation ratio curve (b). Using the continuous ratio curves, one can better comprehend the true profile of the shape characteristics of the sample and extract needed information. The ability to develop a continuous ratio curve like those obtained with the LASS is another advantage of performing automated measurements. It is worth noting that the LASS measurements correlate strongly with the manual measurements of the elongation ratio and the flatness ratio in Figure 5.9.

As previously mentioned, many efforts have been made to develop an automated method to measure particle dimensional ratios. While the previous research methods were successful capturing and analyzing particle data, the LASS has the following advantages over other approaches: much less human intervention, the capability of measuring multiple particles at a time, and the high level of accuracy of the measurement, which is inherent to true 3D measurement technique. These advantages make the LASS very promising.

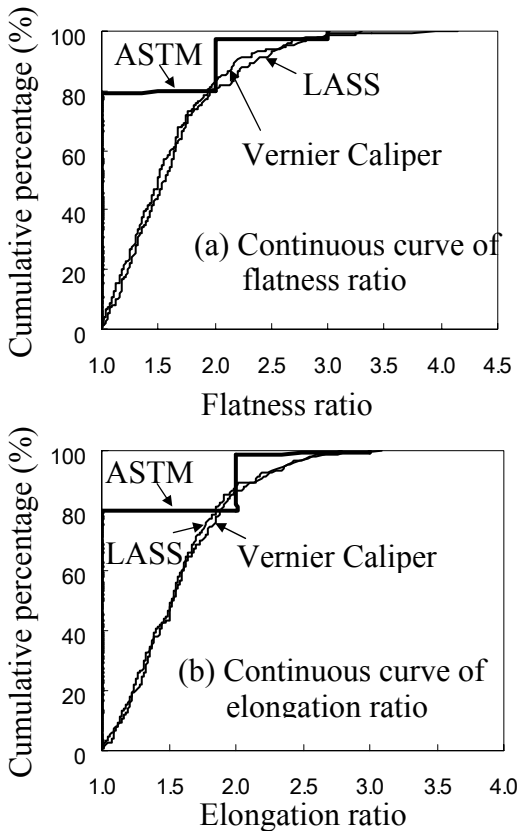

Figure 5.9: Comparison of the dimensional ratios between the proportional caliper, the ASTM proportional caliper, and the LASS measurements by continuous curve: (a) continuous curve of flatness ratio; (b) continuous curve of elongation ratio.

5.3.2 Gradation Tests

To verify the applicability of the LASS in determining particle size distribution, ten aggregate samples were manually sieved in order to compare the results with those from the LASS. The evaluation test samples were formed using aggregate from the four material sources listed in Table 5.1. The ten samples were prepared to three different gradations. The test samples were obtained by sieving larger quantities of stone into distinct size ranges, then manually re-mixing them to achieve the desired gradations. The sample designations and details are given in Tables 5.2 and 5.3.

After the aggregate particles were manually spread on the platform, they were scanned and processed to determine the grading of each sample. Note that unlike the elongation and flatness ratio test, a fairly large number of particles need to be tested to provide one gradation result. This makes it almost impossible to manually spread particles, such that no two particles touch one another. Therefore, particles were roughly spread on the platform, and the segmentation algorithm discussed in Chapter 4 was used to separate particles. Scanning and sizing took approximately 5 to 8 minutes per kg of sample. Figure 5.10 shows the results of the comparison between the LASS and the sieve analysis data. As can be seen from the figure, excellent agreement is exhibited between the manual sieve and the LASS analyses. Note also that the LASS provides a continuous gradation curve across the full range of particle sizes, as opposed to the discrete sieve data representing only the quantity of particles in given size ranges.

Table 5.2: Description of aggregate samples for gradation tests.

Gradation designation	Description of gradation	Sample size (kg)	Material source			
			TX	VA	CA	SD
C-STD	Coarse standard, with most particles larger than 4.75 mm (no. 4 mesh)	6.0	•	•	•	•
C-SM	Similar to C-STD but with proportionally more smaller particles	6.0	•	•	•	•
C-LG	Similar to C-STD but with particles up to 38 mm (1.5 inch)	15.0	•			
C-RND	Same as C-LG but with mostly rounded particles	15.0	•			

Table 5.3: Gradations of the test samples.

Sieve opening	Cumulative percent passing (%)		
	C-LG / C-RND	C-SM	C-STD
1.5” (38.1mm)	100.0	100.0	100.0
1.25" (31.8mm)	93.3	100.0	100.0
1” (25.4mm)	73.3	100.0	100.0
3/4" (19.1mm)	46.7	90.0	83.3
1/2" (12.7mm)	20.0	56.7	31.7
3/8” (9.53mm)	10.0	31.7	11.7
No. 4 (4.75mm)	3.3	6.7	1.7
No. 8 (2.36mm)	0.0	0.0	0.0

The *CANWE* (Cumulative And Normalized Weighted Error) statistic, based on a weighted mean of the errors observed across the full range of particle sizes in a sample, was developed by Browne, one of the research team members of the ICAR project 503, “Rapid Test to Establish Grading of Unbound Aggregate Products”, to give a better indication of machine accuracy (Browne 2001). *CANWE* is defined as:

$$CANWE = \frac{\sum_{i=1}^{N}\left[\left|f_m - f_s\right|_i \cdot \left(\frac{f_m}{d_{med}^{\ 3}}\right)_i \cdot (d_{\max} - d_{\min})_i\right]}{\sum_{i=1}^{N}\left[\left(\frac{f_m}{d_{med}^{\ 3}}\right)_i \cdot (d_{\max} - d_{\min})_i\right]} \qquad (5.8)$$

where

- N: Number of sieve size fractions used in the analysis (e.g., if a stack of six sieves are used in a conventional test with a pan to capture the finest material, then N = 6 + 1 = 7)
- f_s: Percent by weight retained in a sieve fraction, as measured in a standard sieve test
- f_m: Percent by weight retained in a sieve fraction, as measured by a rapid gradation machine
- d_{min}: Smallest sieve opening size corresponding to the lower limit of a sieve fraction
- d_{max}: Largest sieve opening size corresponding to the upper limit of a sieve fraction
- d_{med}: Median sieve opening size in a sieve fraction, $d_{med} = ½ (d_{min} + d_{max})$

In this measure of gradation accuracy, the absolute value of the error $|f_m - f_s|$ in each size fraction is weighted by two factors. The particle count weighting factor, ($f_m/d_{med}^{\ 3}$), was derived by assuming that the particles in a given size range are spherical with a uniform diameter equal to the median mesh size. This weighting factor gives more weight to errors in size fractions with more particles, which tends to emphasize errors in the smaller size ranges where many more particles are required to form a given percentage of the sample weight. The second weighting factor in Equation 5.8 is ($d_{max} - d_{min}$), which gives more weight to measurement errors over more widely spaced size fractions. In a typical sieve

analysis, where more widely spaced mesh sizes are used at the larger size fractions, this weighting factor will tend to emphasize errors in characterizing the largest sample particles. Multiplying the two weighting factors tends to compensate for these effects at both ends of the sample size range. *CANWE* is also normalized with respect to the weighting factors to obtain a dimensionless statistic (Browne 2001).

The CANWE statistic was used to compare the accuracy of the LASS to the 2D DIA based commercial grading machines listed in Table 5.4. The same aggregate test samples used for the LASS were transported to various locations for testing the five commercial grading machines. The commercial machine tests were conducted mainly by Browne between July 2000 and January 2001. New test samples were prepared or re-mixed for evaluating each device, to ensure that the benchmark sample gradations were consistent for all tests. The weight of material in each sample met the minimum requirements set forth in ASTM C136 (1999). More detailed information on how those commercial grading machines were tested can be found in Browne (2001). The results are plotted in Figure 5.11. Note that CANWE is an error statistic, such that smaller values indicate better accuracy. In Figure 5.11, the magnitude of CANWE is plotted downward to enhance the perception that shorter bars (closer to zero) indicate better performance. The conclusion reached from Figure 5.11 is that the LASS shows the best performance in almost every case, with a few exceptions.

Table 5.4: Commercial grading machines evaluated.

Device	Developer	U.S. Sales Representative
VDG-40 Videograder	Laboratoire Central des Ponts et Chaussées, France	Emaco (Canada) Ltd./LTEE
Computerized Particle Analyzer (CPA)	Haver & Boecker	W.S. Tyler
OptiSizer PSDA™ 5400	Danfoss Videk Co.	Micromeritics Instrument Corp.
Video Imaging System (VIS)	John B. Long Co.	John B. Long Co.
Particle Size Distribution Analyzer (PSDA)	Clarkson University	Buffalo Wire Works Co., Inc.

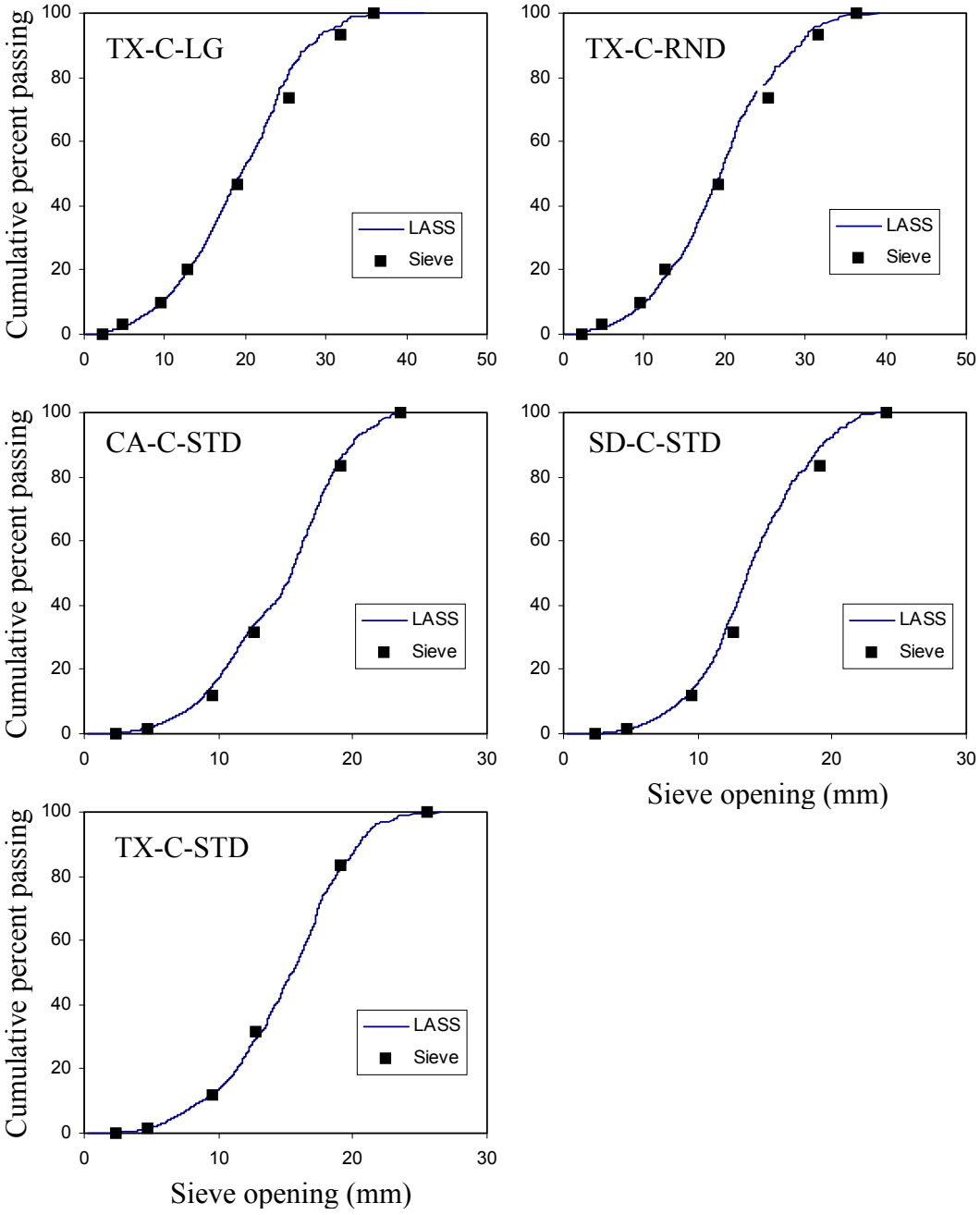

Figure 5.10: Comparison of size distribution results between manual measurement and the LASS measurement.

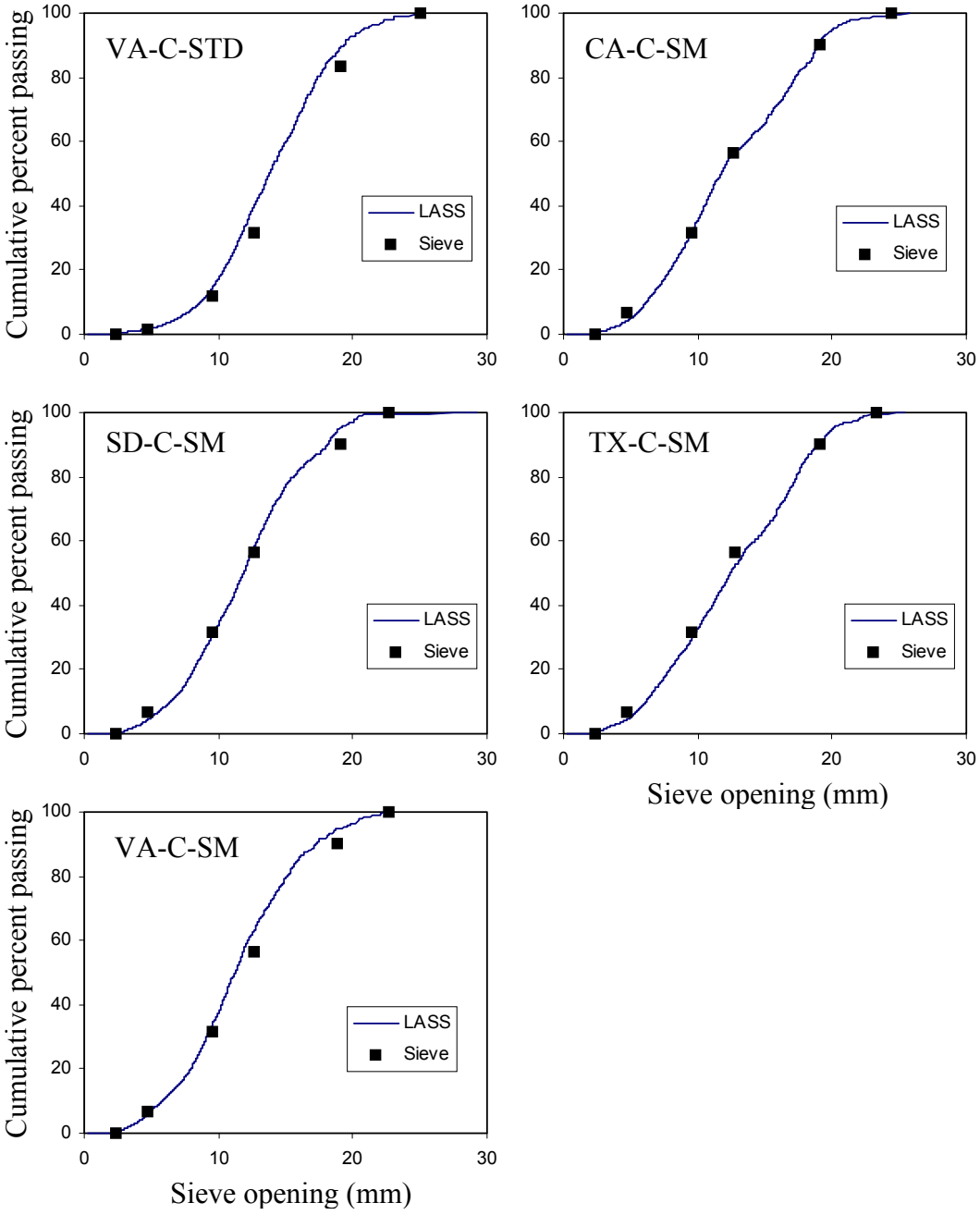

Figure 5.10 (Cont'd): Comparison of size distribution results between manual measurement and the LASS measurement.

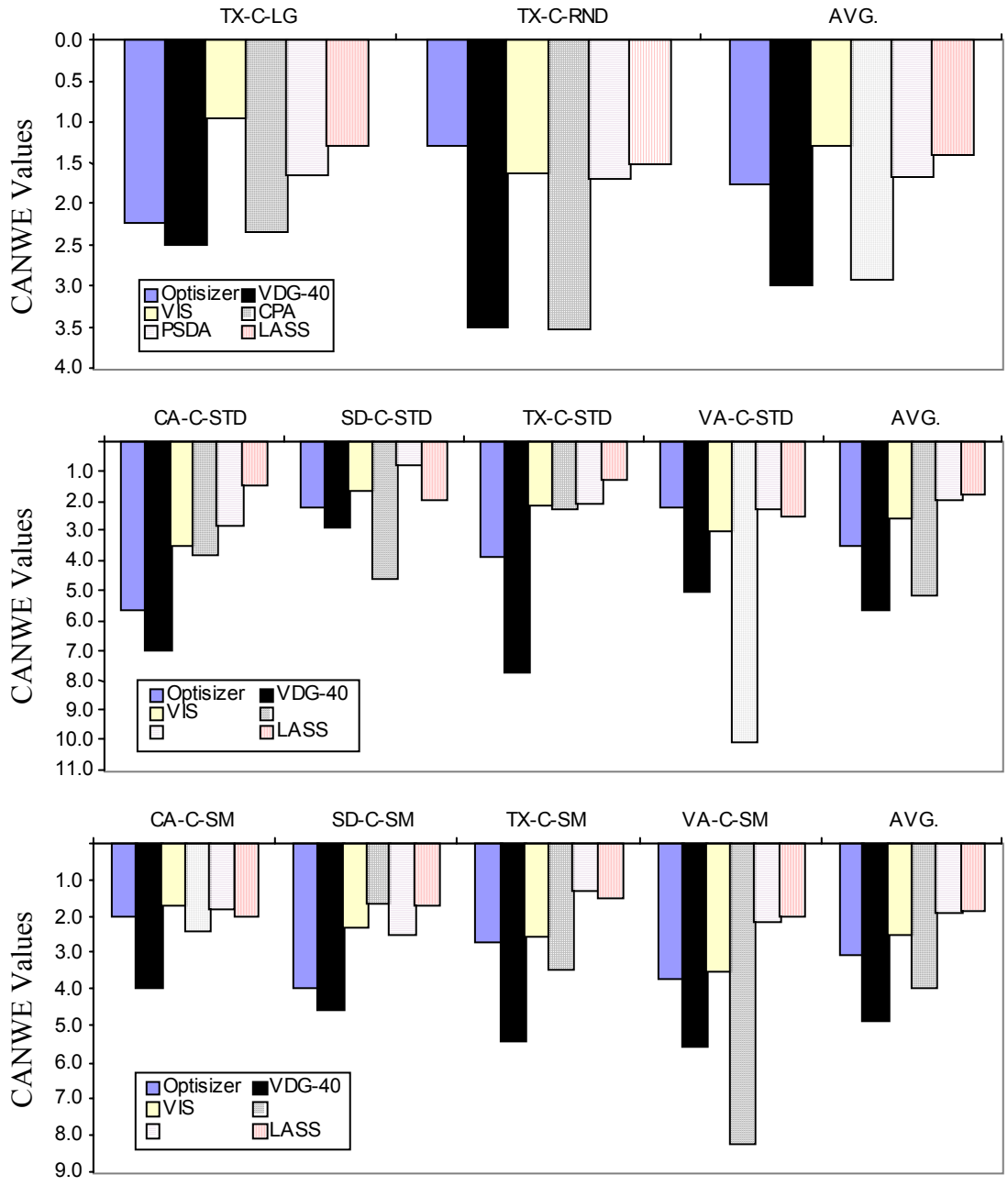

Figure 5.11: Comparison of machine accuracies based on CANWE statistic.

CHAPTER 6
WAVELET-BASED 3D DESCRIPTORS OF AGGREGATE PARTICLES

Morphological characteristics of stone aggregates, including particle shape, angularity, and surface texture, have a significant impact on the performance of HMA materials. To accurately identify and quantify these critical aggregate characteristics, well-defined particle descriptors are essential. Moreover, because a large number of irregular particles must be assessed to adequately characterize an aggregate material, descriptors that can be quantified with automated machines are preferred. In processing true 3D data from a laser scanner, wavelet-based 3D particle descriptors are developed as a way to characterize individual stone particles. Although there is a variety of ways to explain wavelets, a wavelet may be best described as a function with finite length designed to measure variations in a signal. By comparing the wavelet with each part of the signal, the level of fluctuation in the signal can be obtained. Most importantly, the size of the wavelet can be changed to measure different scales of fluctuations in the signal. Aided by this multi-resolution analysis feature of the wavelet transform, the developed descriptors provide a generalized, comprehensive, and objective way of describing aggregates. This chapter first establishes the motivation for development of new 3D particle descriptors along with the introduction of related prior research efforts in section 6.1. Sections 6.2 and 6.3 then review the technologies that can be used for developing particle descriptors with the main focus on wavelet transform. Next, the descriptors are

defined, and their physical meanings are discussed in section 6.4. Finally, the descriptors are applied to various properties of aggregates to demonstrate their applicability to particle characterization in section 6.5.

6.1 INTRODUCTION

Studies (Ahlrich 1996, Barksdale and Samir 1989, Kuo et al. 1998, National Stone Association 1993) have shown that the performance of hot mix asphalt (HMA) materials is significantly impacted by the aggregate's morphological properties, including particle shape, angularity, and surface texture. It is generally recognized that aggregates with equidimensional, angular shapes and rough surfaces increase the strength and durability of HMA. These concepts were incorporated into the current Superpave specification. For example, flatness and elongation ratios (ratios of principal particle dimensions) are used to quantify the shape of coarse aggregate using the ASTM D 4791 test method. For quantifying coarse aggregate angularity, the number of fractured faces on the aggregate particles is used (ASTM D 5821). These standardized methods were selected for their simplicity and the availability of the needed tools. However, these test procedures are labor-intensive, time-consuming, and subject to human errors. Above all, important properties of aggregates may not be captured using these simple measurement methods.

Much research has been conducted to address this problem. Several investigators have utilized 2D DIA to extract various aggregate shape characteristics (Wang et al. 1997, Mora et al. 1998, Ghalib and Hryciw 1999, Kuo

and Freeman 2000, Masad et al. 2000, Masad et al. 2001). These studies have shown that DIA is a promising technique that can identify connections between morphological properties and HMA performance. Some researchers have attempted to extract 3D information from 2D particle images to gain a more comprehensive understanding of the morphological properties (Kuo et al. 1998, Brzezicki and Kasperkiewicz 1999, Rao and Tutumluer 2000, Maerz and Lusher 2001). This is accomplished by capturing and analyzing one or more orthogonal 2D images of the aggregate particles. However, these studies were focused on 3D shape (dimensional ratios) information rather than a complete 3D characterization of angularity and surface texture.

Figure 6.1 shows the process of design and construction improvement, motivated by technological advancements. The technological advancements initiate the process by enabling the discovery of new properties or objective quantification of already known properties in construction materials. This leads to research efforts to establish correlation between the new quantified properties and performances of the construction materials or structures in which they are used. If it turns out that strong correlation exists, new design and construction methods can be developed based on the research results. Since it is now possible to identify positive and negative characteristics, even a new way of producing construction materials can be established to ensure the production of materials with only positive characteristics. As previously mentioned, morphological properties are known to have a great impact on HMA mixes. However, it is not still clear how they do as evidenced by the conflicting results in the literature (Kuo et al. 1998).

Therefore, there is a strong need for well-defined particle descriptors that can accurately identify and quantify critical aggregate characteristics, in order to initiate this design and construction improvement process in HMA.

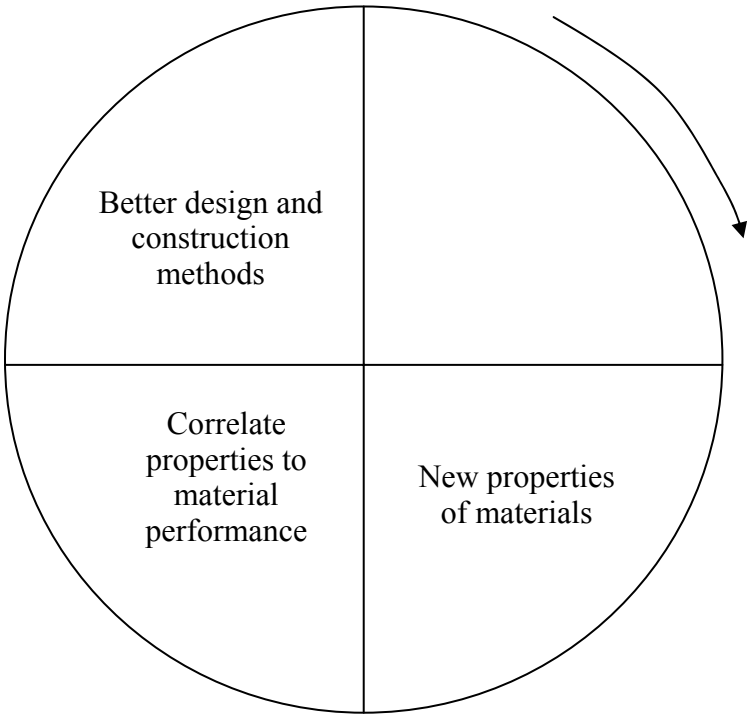

Figure 6.1: Design and construction method improvement process.

6.2 TEXTURE QUANTIFICATION METHODS

In the machine vision field, texture is defined as "something consisting of mutually related elements" (Sonka et al. 1999). Namely, texture can mean a combination of texture elements and the relation between each element. In an attempt to identify the best method that can be used to objectively quantify the

morphological properties of aggregate particles, the following machine-vision-based texture quantification (or classification) methods were investigated:

1. Statistical moments: Each pixel of the image is represented by one of the statistical moments in a region. Statistical moments include mean grayscale level, the standard deviation, skewness, and kurtosis, which are the first, second, third, and fourth order moment, respectively (Parker 1997). This is one of the simplest texture classification methods.
2. Co-occurrence: The co-occurrence matrix method of texture description is based on the repeated occurrence of some grayscale level configuration in the texture (Sonka et al. 1999). Various texture descriptors can be extracted from the co-occurrence matrices such as maximum probability, moments, contrast, homogeneity, entropy, and so on. Gotlieb and Kreyszig (1990) combined several representative co-occurrence descriptors and showed the usefulness of the combined descriptors. Argenti et al. (1990) developed a fast algorithm for the co-occurrence matrix to alleviate the problem of high computational cost. It is known that the co-occurrence matrix does not consider primitive (texture element) shape (Sonka et al. 1999).
3. Edges: Since a texture has large numbers of primitives, it is possible to characterize the texture based on some properties of the primitives. Edge is one of the primitive properties. Direction and the grayscale level gradient of the edge are widely used to segment textures (Parker 1997).

Almost all edge detectors can be used for texture segmentation (Sonka et al. 1999).

4. Laws' Energy: Laws devised a collection of convolution masks to distinguish between different textures. Laws' texture energy measures are derived from three simple vectors, L = (1,2,1), E= (-1,0,1), and S = (-1,2,-1), which represent average grayscale level, edges, and spots, respectively (Wu et al. 1992). By convoluting each of the three vectors with itself or with each other, five vectors of length 5 are obtained. Then, Laws' 5 by 5 convolution masks can be obtained by multiplying the column vectors of length 5 by row vectors of the same length (Wu et al. 1992). By convoluting the Laws' masks with a texture image and calculating energy statistics, a feature vector is derived that can be used for texture description (Sonka et al. 1999).
5. Surfaces: This method is based on a view of the grayscale level image as a 3D surface, so that each pixel has its own small surface. The normal to each plane is a vector, and the normals' direction distribution about the local mean normal characterizes the texture (Parker 1997). Peet and Sahota (1985) used a polynomial surface to better approximate the image.
6. Fractal: Fractal geometry has been used to discriminate between textures. Pentland (1984) showed that a correlation exists between texture coarseness and fractal dimension. However, Wu et al. (1992) demonstrated that a single fractal dimension is not sufficient for description of textures. Thus, Fractal description of textures is typically

based on determination of two factors: fractal dimension and a second-order statistic called lacunarity (Sonka et al. 1999).

7. Mathematical morphology: In order to quantify a particle surface texture, Kuo and Freeman (2000) used the ratio between the perimeter and the convex perimeter. The convex perimeter is the perimeter of the bounding polygon, which is the approximation of feature boundary without surface texture. Such morphological operations as binary erosion and dilation were also used to quantify particle surface texture (Masad 2001).
8. Fourier transform: The Fourier spectrum is ideally suited for describing the directionality of periodic or almost periodic two-dimensional patterns in an image (Gonzalez and Wintz 1987). Day and Rogers (1996) applied the Fourier transform to the analysis of a bread slice. Features extracted from the spectrum were shown to correlate with measures used in the baking community for describing the crumb grain of bread. Taylor and Costello (1999) applied the Fourier transform to the image taken of the cytoplasm of human lenses, and concluded that some nuclear cataracts do not contain large spatial fluctuations in the cytoplasm.

Some of the texture quantification methods are considered as data compression methods. For example, the discrete cosine transform, which is similar to the Fourier transform, forms the basis of the Joint Photographic Experts Group (JPEG) image compression method (Sonka et al. 1999). The discrete cosine transform uses cosine functions as its base functions, instead of

combinations of sine and cosines functions as in the Fourier transform, to convert a signal in time (space) domain into that of frequency domain. Typically, data compression starts with this kind of linear time-frequency transform process. Then, the data in the frequency domain are rounded off to a set of predefined values. At this stage, some information can be lost, but they are, in general, not recognizable by human perception. Finally, the transformed data are codified such that more frequently used grayscale values (or symbols) are expressed with shorter code words while less frequently used ones are expressed with longer code words. In this way, the data can be represented in a more reduced form. A comprehensive treatment of data compression methods can be found in Mallat (1999).

6.3 WAVELET TRANSFORM

A wavelet transform decomposes a signal into a group of linear combinations with each combination having different resolutions. This transform is conducted using a finite length of a basis function called a "mother wavelet". When compared to the signal being analyzed, the length and location of the mother wavelet are changed (dilation and translation) to find where and how much each dilated and translated version of the mother wavelet coincides with the signal. The dilation and translation mechanism of the mother wavelet enables not only the production of localized information in space and frequency domains, but also provides an effective representation of the signal, making the wavelet transform superior to other texture quantification methods in particle

characterization. The following sections review 1D and 2D wavelet analyses and are based on the work presented in Bachman et al. (2000), Blatter (1998), Burrus et al. (1998), Chui (1992), Daubechies (1992), Mallat (1999), Newland (1993), Oppenheim et al. (1999), and Rao and Bopardikar (1998).

6.3.1 One-dimensional Wavelet Transform

Wavelet analysis can best be explained with the intrinsic characteristic of Multiple-Resolution Analysis (MRA). Figure 6.2 shows a schematic of how a wavelet transform decomposes a signal into a group of linear combinations. V_0, V_1, and V_2 are vector spaces such that V_0 is a subspace of V_1, and V_1 is a subspace of V_2. W_0 and W_1 are "difference" vector spaces between V_0 and V_1, and V_1 and V_2, respectively. These relationships can be expressed as:

$$V_0 \oplus W_0 = V_1 \tag{6.1}$$

$$V_1 \oplus W_1 = V_2 \tag{6.2}$$

where $\oplus$ represents vector addition.

Figure 6.2 also shows that the vector spaces V_0, W_0, and W_1 are mutually orthogonal. If all of the available vector spaces are shown in Figure 6.2, the most accurate approximation of a signal $f(t)$ can be obtained by projecting it on V_2, which is f_{V_2}. Likewise, if more approximations are needed for the signal, f_{V_1} and f_{V_0} (projections on V_1 and V_0, respectively) would minimize the information loss. This implies that the signal can be represented with various

levels of approximation, minimizing possible information loss in each. That is, depending on the degree of accuracy required, various levels of the difference vector (f_{W_0}, f_{W_1}, and so on) can be added to the initial approximation f_{V_0} to better represent the signal. As an example, the signal f_{V_2} can be expressed as:

$$f_{V_2} = f_{V_0} + f_{W_0} + f_{W_1} \tag{6.3}$$

Expansion of the vector spaces can generalize Equation (6.3) to:

$$f(t) = f_{V_0} + \sum_{j=0}^{\infty} f_{W_j} \tag{6.4}$$

Since f_{V_0} and f_{W_j} can also be represented as a linear combination of basis functions, Equation (6.4) can be expressed as:

$$f(t) = \sum_{k=-\infty}^{\infty} c_{0,k}\varphi_{0,k}(t) + \sum_{j=0}^{\infty}\sum_{k=-\infty}^{\infty} d_{j,k}\psi_{j,k}(t) \tag{6-5}$$

where $\varphi_{0,k}(t)$ and $c_{0,k}$ are basis functions and their corresponding coefficients for f_{V_0}, respectively, and $\psi_{j,k}(t)$ and $d_{j,k}$ are basis functions and their corresponding coefficients for f_{W_j}, respectively. Here, the basis function $\varphi_{0,k}(t)$ for the initial approximation of a signal is called the "scaling function", and the basis function $\psi_{j,k}(t)$ for the difference vectors is called the "wavelet". Note that as the level of difference vector space increases, better resolution is obtained in Figure 6.2. This implies that as *j* increases, the length over which the wavelet

$\psi_{j,k}(t)$ exists is reduced. This is the multi-resolution aspect of wavelet analysis, which enables an efficient representation of a signal in the sense that high frequency parts of the signal are represented with better resolution than low frequency parts.

By expanding the area of j to negative infinity, Equation (6.5) becomes:

$$f(t) = \sum_{j=-\infty}^{\infty} \sum_{k=-\infty}^{\infty} d_{j,k} \psi_{j,k}(t) \tag{6.6}$$

Therefore, if wavelets $\psi_{j,k}(t)$ are orthonormal to each other, wavelet coefficients $d_{j,k}$ are expressed as:

$$d_{j,k} = < f(t), \psi_{j,k}(t) > = \int_{-\infty}^{\infty} f(t) \psi_{j,k}(t) dt \tag{6.7}$$

where <x, y> means the inner product of x and y. Equation (6.7) is called the wavelet transform.

Wavelets are obtained by scaling and translating the so-called "mother wavelet" in the following manner:

$$\psi_{j,k}(t) = \frac{1}{\sqrt{j}} \psi\left(\frac{t-k}{j} \right) \tag{6.8}$$

where ψ is the mother wavelet, and j and k are scale and translation coefficients, respectively. The mother wavelet can be compared with any part of the signal

with any expanded format by choosing various *j*'s and *k*'s. In Equation (6.8), $\frac{1}{\sqrt{j}}$ is used to make the norm of $\psi_{j,k}(t)$ equal to 1. Also, note that *j* is the inverse concept of frequency. The mother wavelet is a compactly supported (finite length) function that has the following properties:

$$\int_{-\infty}^{\infty} \psi(t)dt = 0 \tag{6.9}$$

$$\|\psi\| = 1 \tag{6.10}$$

where $\|x\|$ is the norm of x; i.e., $< x, x >$. In most cases of discrete wavelet transform, the mother wavelet is transformed and dilated as follows:

$$\psi_{j,k}(t) = 2^{j/2}\psi\left(2^j t - k\right) \tag{6.11}$$

where *j* and *k* are integers. These compactly supported wavelets enable wavelet coefficients $d_{j,k}$ to drop off rapidly, thereby allowing for efficient representation of the signal. In conclusion, wavelet analysis transforms a 1D signal into a 2D time (space)–frequency domain showing where and how much the dilated and translated versions of the mother wavelet correlate with the signal.

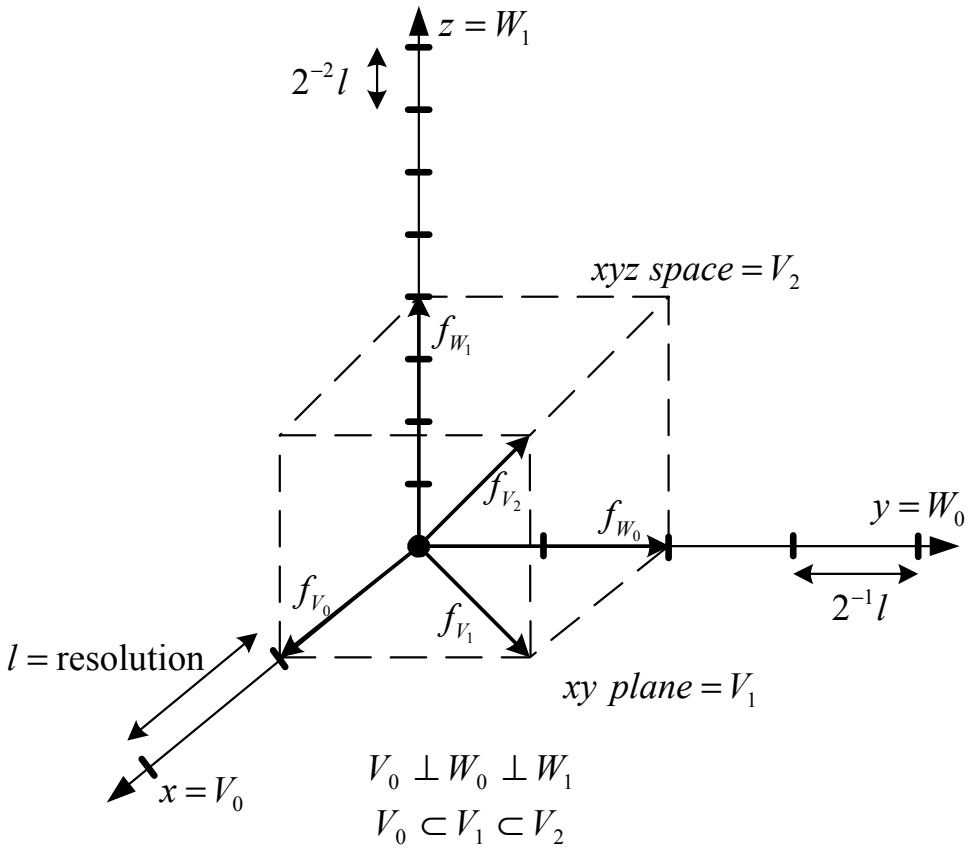

Figure 6.2: Decomposition of a signal $f(t)$ using wavelet transform.

6.3.2 Two-dimensional Wavelet Transform

Two-dimensional wavelet analysis begins by defining 2D basis functions as the tensor product of scaling functions $\varphi(x)$ and $\varphi(y)$. Then, from the orthonormal characteristic of the 2D basis functions, a signal $f(x, y)$ (2D image) can be represented as:

$$f_1(x,y) = \sum_{i=-\infty}^{\infty} \sum_{j=-\infty}^{\infty} a_1(i,j)\varphi(2x-i)\varphi(2y-j) \tag{6.12}$$

in V_1. Since $\sum_{i=-\infty}^{\infty} a_1(i,j)\varphi(2x-i)$ in Equation (6.12) is a 1D signal and can be represented as a sum of the approximation in V_0 and the difference vector in W_0, it becomes:

$$\sum_{n=-\infty}^{\infty} a_{0,j}(n)\varphi(x-n) + \sum_{n=-\infty}^{\infty} b_{0,j}(n)\psi(x-n) \tag{6.13}$$

Substituting Equation (6.13) in Equation (6.12),:

$$\begin{aligned} f_1(x,y) = & \sum_{j=-\infty n=-\infty}^{\infty} \sum_{a_{0,j}}^{\infty} (n)\varphi(x-n)\varphi(2y-j) \\ & + \sum_{j=-\infty n=-\infty}^{\infty} \sum_{b_{0,j}}^{\infty} (n)\psi(x-n)\varphi(2y-j) \end{aligned} \tag{6.14}$$

Likewise, if $\sum_{j=-\infty}^{\infty} a_{0,j}(n)\varphi(2y-j)$ and $\sum_{n=-\infty}^{\infty} b_{0,j}(n)\varphi(2y-j)$ in Equation (6.14) are decomposed into their approximations and difference vectors,:

$$
\begin{aligned}
f_1(x,y) = & \sum_{i=-\infty}^{\infty}\sum_{j=-\infty}^{\infty} c_0(i,j)\varphi(x-i)\varphi(y-j) \\
& + \sum_{i=-\infty}^{\infty}\sum_{j=-\infty}^{\infty} d_{0,0}(i,j)\varphi(x-i)\psi(y-j) \\
& + \sum_{i=-\infty}^{\infty}\sum_{j=-\infty}^{\infty} d_{0,1}(i,j)\psi(x-i)\varphi(y-j) \\
& + \sum_{i=-\infty}^{\infty}\sum_{j=-\infty}^{\infty} d_{0,2}(i,j)\psi(x-i)\psi(y-j)
\end{aligned}
\tag{6.15}
$$

Thus, by adding an infinite number of difference vectors to the initial approximation, $f(x,y)$ is obtained as follows:

$$
\begin{aligned}
f(x,y) = & \sum_{j=-\infty}^{\infty}\sum_{k=-\infty}^{\infty} c_0(j,k)\varphi(x-j)\varphi(y-k) \\
& + \sum_{i=0}^{\infty}\sum_{j=-\infty}^{\infty}\sum_{k=-\infty}^{\infty} d_{i,0}(j,k)\varphi(2^{-i}x-j)\psi(2^{-i}y-k) \\
& + \sum_{i=0}^{\infty}\sum_{j=-\infty}^{\infty}\sum_{k=-\infty}^{\infty} d_{i,1}(j,k)\psi(2^{-i}x-j)\varphi(2^{-i}y-k) \\
& + \sum_{i=0}^{\infty}\sum_{j=-\infty}^{\infty}\sum_{k=-\infty}^{\infty} d_{i,2}(j,k)\psi(2^{-i}x-j)\psi(2^{-i}y-k)
\end{aligned}
\tag{6.16}
$$

Therefore, using the orthonormal characteristic of 2D basis functions, wavelet coefficients can be obtained as follows:

$$
d_{i,j,k,l} = < f(x,y), W_{i,j,k,l}(x,y) > = \int_{-\infty}^{\infty} f(x,y) W_{i,j,k,l}(x,y)\,dxdy \tag{6.17}
$$

$$
i, j, k \in Z,\ l \in [0,2]
$$

where $W_{i,j,k,0} = \varphi(2^{-i}x - j)\psi(2^{-i}y - k)$, $W_{i,j,k,1} = \psi(2^{-i}x - j)\varphi(2^{-i}y - k)$, and $W_{i,j,k,2} = \psi(2^{-i}x - j)\psi(2^{-i}y - k)$.

6.3.3 Computation of Wavelet Transform

In practical discrete wavelet transform calculations, a signal is passed through a High Pass Filter (HPF) and a Low Pass Filter (LPF), with coefficients that are associated with each wavelet system. If the output signal passed through the HPF is down-sampled by two (i.e., only alternate samples are retained), the remaining signal corresponds to $d_{0,k}$ in Equation (6.5). Likewise, if the outputs of the LPF are down-sampled by 2, the results become $c_{0,k}$ in Equation (6.5). That is, it is possible to calculate wavelet coefficients without directly dealing with wavelet and scaling functions. This signal processing scheme is expressed as:

$$c_{j,k} = \sum_m l[2k - m]c_{j+1,m} \tag{6.18}$$

$$d_{j,k} = \sum_m h[2k - m]c_{j+1,m} \tag{6.19}$$

where $l[2k - m]$ is the LPF, and $h[2k - m]$ is the HPF. As Equations (6.18) and (6.19) imply, this is a recursive way of calculating wavelet coefficients. Thus, a signal can be decomposed into various resolutions of detail by repeating this process.

A 1D wavelet transform using Finite Impulse Response (FIR) filters can be extended to a 2D wavelet transform explained in the previous section. First, all

the rows of the 2D signal (image) are passed through a HPF and a LPF, and down-sampled by two. This divides the image into two sub-images. Second, all columns of each sub-image are filtered using the HPF and LPF and down-sampled by two. That is, a 2D wavelet transform is conducted by treating each row and column of the image as a 1D signal. As shown in Figure 6.3, the image is divided into four different sub-images by one-level decomposition of the 2D wavelet transform. While c_i is simply an approximation of the image, $d_{i,0}$, $d_{i,1}$, and $d_{i,2}$ show vertical, horizontal, and diagonal edge information at the corresponding resolution, respectively. As in the 1D case, by decomposing the sub-image c_i repeatedly, MRA results can be obtained. Figure 6.4 shows a three-level decomposition of an image.

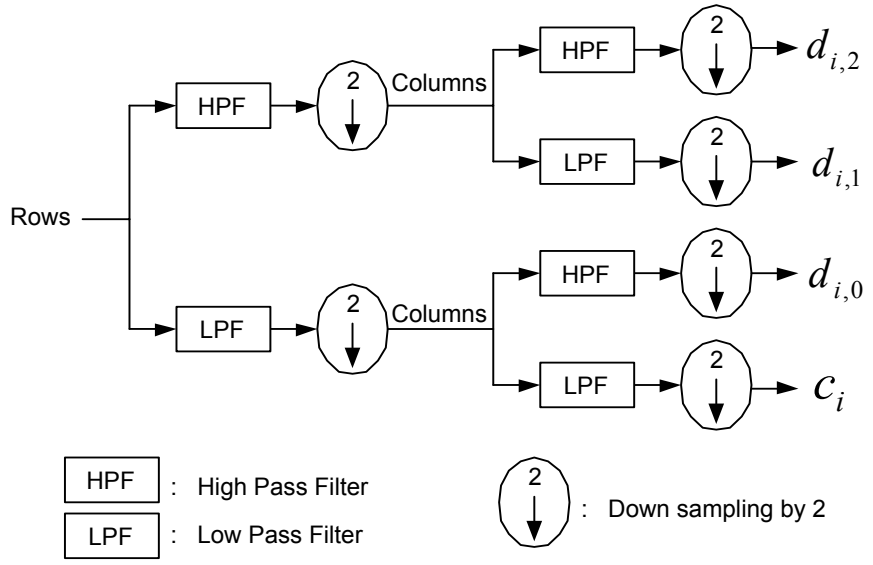

Figure 6.3: One-level wavelet transform of a 2D signal $f(x, y)$ using signal processing.

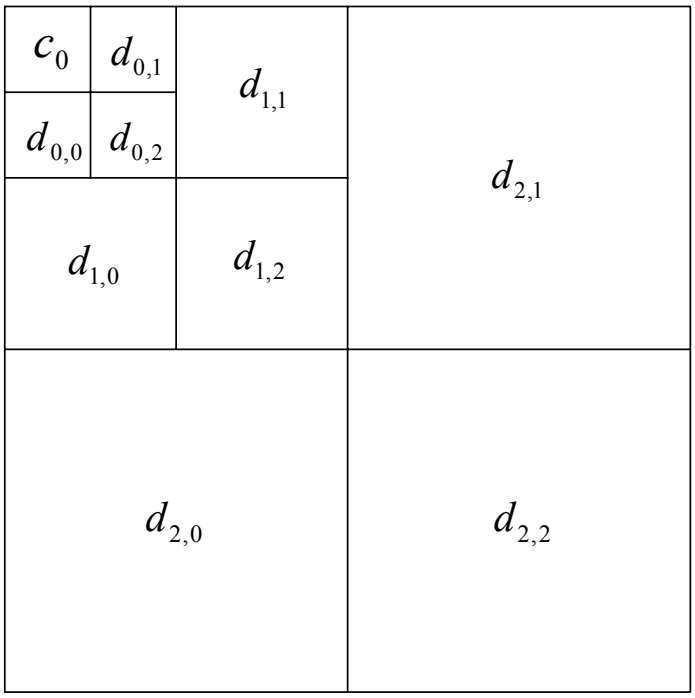

Figure 6.4: Three-level decomposition of a 2D signal $f(x, y)$ using wavelet transform.

6.4 THE PARTICLE DESCRIPTION METHOD DEVELOPED

6.4.1 Coordinate Conversion Algorithm

The 3D Cartesian coordinate data obtained with the LASS is converted into polar coordinates, which allows for a generalized description of 3D particle data, using a coordinate conversion algorithm. This algorithm also interpolates missing data such as the bottom portion of each particle, which is hidden from the scanner. As shown in Figure 6.5, the horizontal angle (α) spans from 0° to 360°, while the vertical angle (β) ranges from -90° to +90°, both with a resolution of

one degree. Thus, the polar coordinate domain can be considered a 181 by 361 2D array of which elements represent radius values at different horizontal and vertical angles. The algorithm is briefly explained subsequent to the definition of the following five conditions:

- Condition A: The element of interest, $f(\alpha, \beta)$ is zero, where α is the horizontal angle and β is the vertical angle.
- Condition B: There exists at least one non-zero element within certain horizontal and vertical angle distances from the element of interest. Determination of an appropriate range for the distances considers that as the vertical angle is close to either -90° or +90°, the number of datum points per unit area tends to be relatively high.
- Condition C: β of the element of interest is larger than or equal to 0.
- Condition D: When the element of interest is $f(\alpha, \beta)$, $f(\alpha, \beta+1)$ is nonzero.
- Condition E: $|f(\alpha, \beta+1)\sin\beta| > (Particle\ Thickness/2)$ when condition D is met (Figure 6.6 (c)).

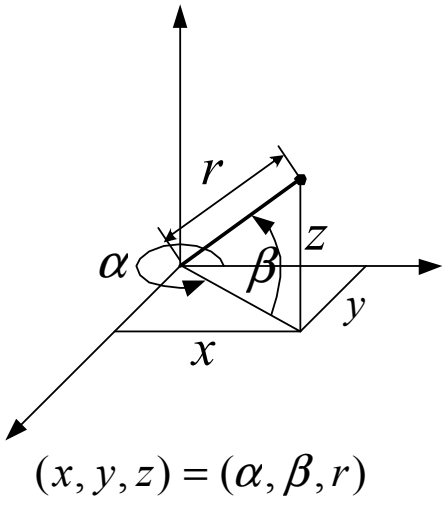

Figure 6.5: Relationship between Cartesian coordinate and polar coordinate system.

1. After initializing all the elements of the polar coordinate domain to zero, transform the recorded data in the Cartesian coordinate domain into the polar coordinate domain using the relationship depicted in Figure 6.5. The center point of the particle length, width, and height is chosen as the origin for the polar coordinate domain.
2. Fill all the elements that have $90\,\beta$, $f(\alpha,90)$, with a transformed value that has the highest β.
3. Fill all the elements that have negative $90\,\beta$, $f(\alpha,-90)$, with the value of $(Particle\ Thickness / 2)$.
4. Make all the elements with $0\,\alpha$, $f(0,\beta)$, the same as their corresponding elements with $360\,\alpha$, $f(360,\beta)$.
5. If condition A is true and the element of interest, $f(\alpha,\beta)$, is within a horizontal angle distance of $x/2$ from the horizontally closest transformed element, then $f(\alpha,\beta)$ is filled with the value of the transformed element, where $x = \dfrac{C}{\cos(\beta)}$ and C is an integer value based on the data resolution of the Cartesian coordinate system. This takes into account the effect mentioned in condition B.
6. If conditions A, B, and D are true, fill $f(\alpha,\beta)$ with a linearly interpolated value calculated based on $f(\alpha,\beta+1)$ and the non-zero value from condition B.
7. If conditions A, C, and D are true and B is false, then:

$$f(\alpha,\beta) = f(\alpha,\beta+1)\frac{\cos(\beta+1)}{\cos(\beta)} \tag{6.20}$$

This operation is based on the assumption that $f(\alpha,\beta)$ is part of a vertical wall (Figure 6.6 (a)).

8. If condition A and D are true and B, C, and E are false, then:

$$f(\alpha,\beta) = f(\alpha,\beta+2\gamma) \tag{6.21}$$

where γ is the vertical angle difference between β and the lowest vertical angle at which a nonzero transformed element, $f(\alpha,\beta+\gamma)$, exists. The hidden underside of a particle that is not scanned is given the values of its symmetrical surface counterparts by this operation (Figure 6.6 (b)).

9. If condition A, D, and E are true and B and C are false, fill $f(\alpha,\beta)$ with a linearly interpolated value calculated based on $f(\alpha,\beta+1)$ and $f(\alpha,-90)$. This operation keeps the vertical projection of $f(\alpha,\beta)$ within the range of half the particle thickness.

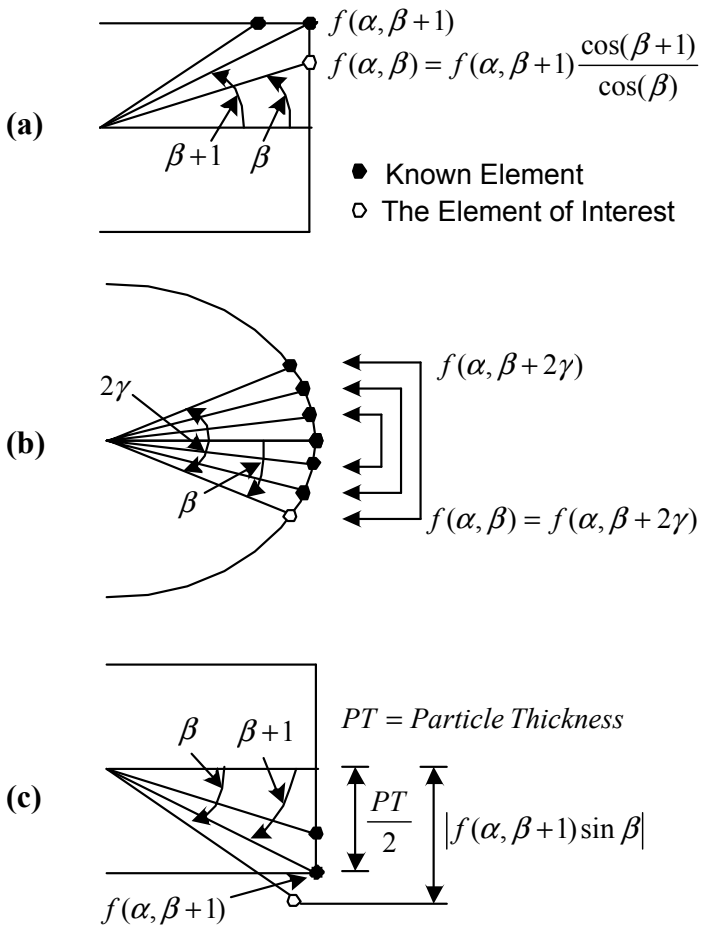

Figure 6.6: Strategies for filling zero elements in the coordinate conversion algorithm: (a) Step seven; (b) Step eight; (c) Condition E.

6.4.2 Wavelet-based 3D Particle Descriptors

Most of the research on individual particle characterization has involved attempts to measure particle properties on different scales. For example, surface texture is measured on the finest scale while angularity and shape are measured on moderate and coarse scales, respectively. However, there have been significant inconsistencies in the way properties on different scales are measured. In general, smoothness of the particle surface texture has been determined by the uniformity of the measured values. Elongation and flatness ratios (EFR), widely used indicators of particle shape, only measure proportions of the three principal dimensions of a particle and disregard all other information. To overcome this shortcoming and to provide a more generalized approach to 3D particle characterization, wavelet-based 3D particle descriptors are developed. Essentially, these morphological parameters make use of the degree of correlation between wavelets on different scales and the particle to be inspected in order to measure particle shape, angularity, and surface texture.

If the polar coordinate system (Figure 6.5) is used, 3D particle data can be expressed as:

$$f(\alpha,\beta)=\sum_{i=-\infty}^{\infty}\sum_{j=-\infty}^{\infty}\sum_{k=-\infty}^{\infty}\sum_{l=0}^{2}d_{i,j,k,l}W_{i,j,k,l}(\alpha,\beta) \tag{6.22}$$

$$i,j,k\in Z,\ l\in[0,2]$$

where i indicates different decomposition levels, j are scale coefficients, k are translation coefficients, $W_{i,j,k,0}=\varphi(2^{-i}\alpha-j)\psi(2^{-i}\beta-k)$, $W_{i,j,k,1}=$

$\psi(2^{-i}\alpha - j)\varphi(2^{-i}\beta - k)$, $W_{i,j,k,2} = \psi(2^{-i}\alpha - j)\psi(2^{-i}\beta - k)$, and $f(\alpha, \beta)$ is the length of the radius vector at angle α and β. Wavelet coefficients are then obtained as follows:

$$d_{i,j,k,l} = < f(\alpha,\beta), W_{i,j,k,l}(\alpha,\beta) > = \int_{-\infty}^{\infty} f(\alpha,\beta) W_{i,j,k,l}(\alpha,\beta) d\alpha d\beta \qquad (6.23)$$

$$i, j, k \in Z,\ l \in [0,2]$$

As described previously, the wavelet transform compares a mother wavelet to the signal to determine how well the signal coincides with dilated and translated versions of the mother wavelet. As a result, coefficients obtained using fine scale wavelets represent particle surface texture, whereas coefficients from larger scale wavelets correspond to either angularity or shape, depending on the expansion degree of the mother wavelet. Therefore, by measuring the magnitude of the wavelet coefficients on each scale, particle shape, angularity, and surface texture can be quantified in a consistent way. The following descriptors are thus defined:

$$Shape\ Index = \frac{E(d_{0,j,k,l}) + E(d_{1,j,k,l})}{Average\ Radius} \qquad (6.24)$$

$$Angularity\ Index = \frac{E(d_{2,j,k,l}) + E(d_{3,j,k,l})}{Average\ Radius} \qquad (6.25)$$

$$Texture\ Index = \frac{E(d_{4,j,k,l}) + E(d_{5,j,k,l})}{Average\ Radius} \qquad (6.26)$$

where E means energy (summation of absolute values of all the elements) and $d_{i,j,k,l}$ are wavelet coefficients at a decomposition level i. The above descriptors are based on the assumption that the raw 3D particle data are available at every degree interval. For the shape quantification, the energy of the first and second decomposition level wavelet coefficients ($d_{0,j,k,l}$ and $d_{1,j,k,l}$, respectively) are added together. Angularity is measured with the summation of the energy of the next two finer level wavelet coefficients, $d_{2,j,k,l}$ and $d_{3,j,k,l}$. Finally, the finest two levels of wavelet coefficients, $d_{4,j,k,l}$ and $d_{5,j,k,l}$, are used to quantify the texture of the particle surface in the same manner. In other words, after six levels of wavelet transforms are conducted, the two coarsest levels of coefficients are used for shape, the two middle levels for angularity, and the two finest levels for surface texture. If a perfectly smooth sphere were measured with this method, all the descriptors would be zero because there would be no variation in the radius vectors on any scale, that would be captured by wavelets.

Differences in the concept of data resolution in different coordinate or dimensional spaces deserve consideration. Here, "resolution" is used to express the separation between adjacent points on the surface of a particle. In 2D DIA, resolution is typically defined as the number of pixels in a unit length or unit area, such as 10 pixels/mm or 100 pixels/mm^2. Similarly, resolution in a 3D Cartesian coordinate system can be expressed as the number of datum points (voxels) in a unit volume. In a polar coordinate system, however, resolution is not so easily defined because the distance between surface data points varies with the associated angle and radial distance.

Note that the wavelet-based descriptors are computed using angles (degrees) and that the average particle radius is used to normalize all three descriptors. Using a polar coordinate system to define the indices provides several advantages over using a Cartesian coordinate system. First, different resolutions are automatically determined with respect to the size of each particle. It is evident that characterizing small particles will require higher resolutions than larger particles. For example, the resolution needed to characterize a golf ball should be much higher than that required to characterize the moon. Since the distance between two adjacent data points on the surface depends on the particle's size in the polar coordinate system, the wavelet-based descriptors are applicable to characterizing any size particle without changing the index definitions. However, care must be exercised in converting the raw 3D data, acquired in a Cartesian coordinate system, to those in a polar coordinate system. The resolution of the raw 3D data must be high enough to validate the converted polar coordinate data.

Second, the same number of decomposition levels can be used irrespective of particle size. The aforementioned ability to determine the proper resolution according to the particle size also allows for the use of the same decomposition levels. However, it remains to be seen if the six levels of decomposition are sufficient to adequately capture the particle properties desired. More or fewer decomposition levels may be needed to produce meaningful interpretations of particle properties. It may also be necessary to use the six different levels of particle information separately for more complete particle characterization.

Questions of this kind can only be answered with more research aimed at connecting the quantified particle characteristics to the behavior of HMA mixes.

Finally, the average radius used to normalize the particle indices yields particle properties that are independent of size. It is likely that large particles have more variations in their radius data than small particles. As a result, if the indices were not normalized by the average radius, the large particles would tend to have higher particle indices than small particles. Thus, it is essential to normalize the indices to eliminate the impact related to particle size. Figure 6.7 shows this particle characterization scheme in a 2D manner. Note that Figure 6.7 serves only as a schematic explanation of the developed descriptors; the number of wavelets used in the developed descriptors is much larger than depicted and only every third wavelet is described. As shown in Figure 6.7, the area that the mother wavelet covers from one location is expanded as the scale goes up, which enables larger scale measurements. Theoretically, $d_{5,j,k,l}$, $d_{4,j,k,l}$, $d_{3,j,k,l}$, $d_{2,j,k,l}$, $d_{1,j,k,l}$, and $d_{0,j,k,l}$ are obtained on every interval of 2, 4, 8, 16, 32, and 64 degrees, respectively, due to the down-sampling process. However, in practical applications, to convolute the first or last part of the signal with a finite impulse response (FIR) filter, the signal may be extended depending on the length of the FIR filter. The developed method uses Daubechies' D4 wavelet (Daubechies 1992), which is known to work well with natural images. As a result, $d_{0,j,k,l}$ is obtained on approximately every 35°.

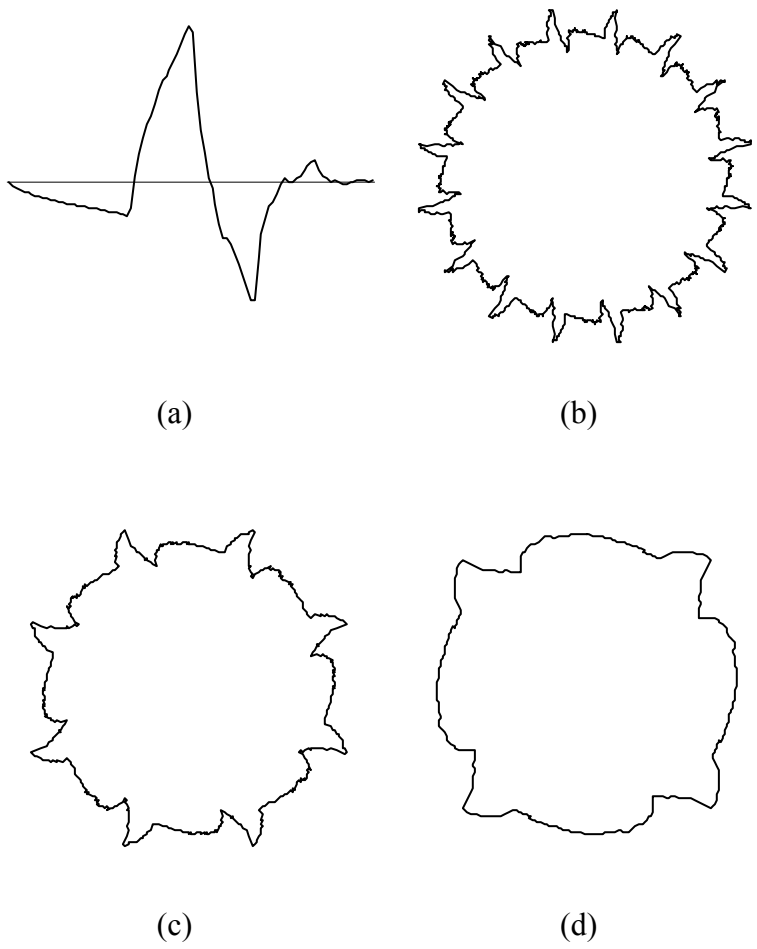

Figure 6.7: A particle characterization scheme with wavelet transform: (a) Daubechies' D4 mother wavelet; (b) Surface measurement; (c) Angularity measurement; (d) Shape measurement.

The wavelet-based particle descriptors developed enable more representative characterization of an individual particle, in the sense that the original particle data can be reconstructed with the wavelet coefficients. These descriptors also establish a consistent way of measuring particle characteristics, irrespective of the type of property, by always measuring the energy of the wavelet coefficients at each scale. In addition, virtually all particle information is incorporated into these descriptors because all consecutive levels of wavelet coefficients are used. Figure 6.8 illustrates the comprehensiveness of the particle descriptors developed. The three indices – texture, angularity, and shape – cover the entire particle information (although it is theoretically impossible to represent the exact particle surface), while the Elongation and Flatness Ratios (EFR) and the spatially sampled texture index cover just a small portion of what they are supposed to cover. The EFR may be a more intuitive measure, but their capacity to absorb the shape information is confined to a certain measurement scale as shown in Figure 6.8. (Note that the EFR span over the entire space range in Figure 6.8 because the three principal dimensions (length, width, and thickness) required to calculate the EFR circumscribe the entire particle.) As a result, if the corresponding angularity index does not incorporate the shape information that is not covered by the EFR, some important shape information can be lost. In the same manner, if a small portion of the particle surface is spatially sampled to calculate the texture index, the index may not be representative of the entire particle surface texture. Therefore, both the EFR and the sampled index can be considered arbitrary enough to miss other important particle information. This is

why the wavelet-based particle descriptors are developed in order to produce generalized, comprehensive, and accurate particle characterizations. In conjunction with the average radius of the particle, they are expected to quantify particle characteristics objectively.

6.5 EXPERIMENTAL RESULTS

The LASS was used to obtain 3D data on stone particles taken from samples of rounded limestone river gravel, crushed limestone, crushed quartzite, and crushed granite. The size of the particles used for these tests ranged from 22 to 58 mm in their longest dimension. Each tested particle was scanned twice in opposite directions by the LASS; the two data sets were then merged to minimize possible data loss resulting from self occlusion (as discussed in Chapter 4). For 20 particles, it took approximately 7 to 10 minutes for the data acquisition and merging process and approximately 25 seconds to analyze the data. A 0.3 mm/pixel resolution was obtained and signal noise was not removed in order to keep the raw data as intact as possible. The 3D particle data obtained in this way were analyzed using custom software developed with the C programming language, LabView (a graphical programming language sold by National Instruments), and the Wavelet and Filter Bank Design Toolkit (a wavelet analysis toolkit sold by National Instruments). Properties of the test particles were quantified using the wavelet-based 3D particle descriptors (i.e., shape, angularity, and texture indices) to verify their applicability in characterizing aggregate materials.

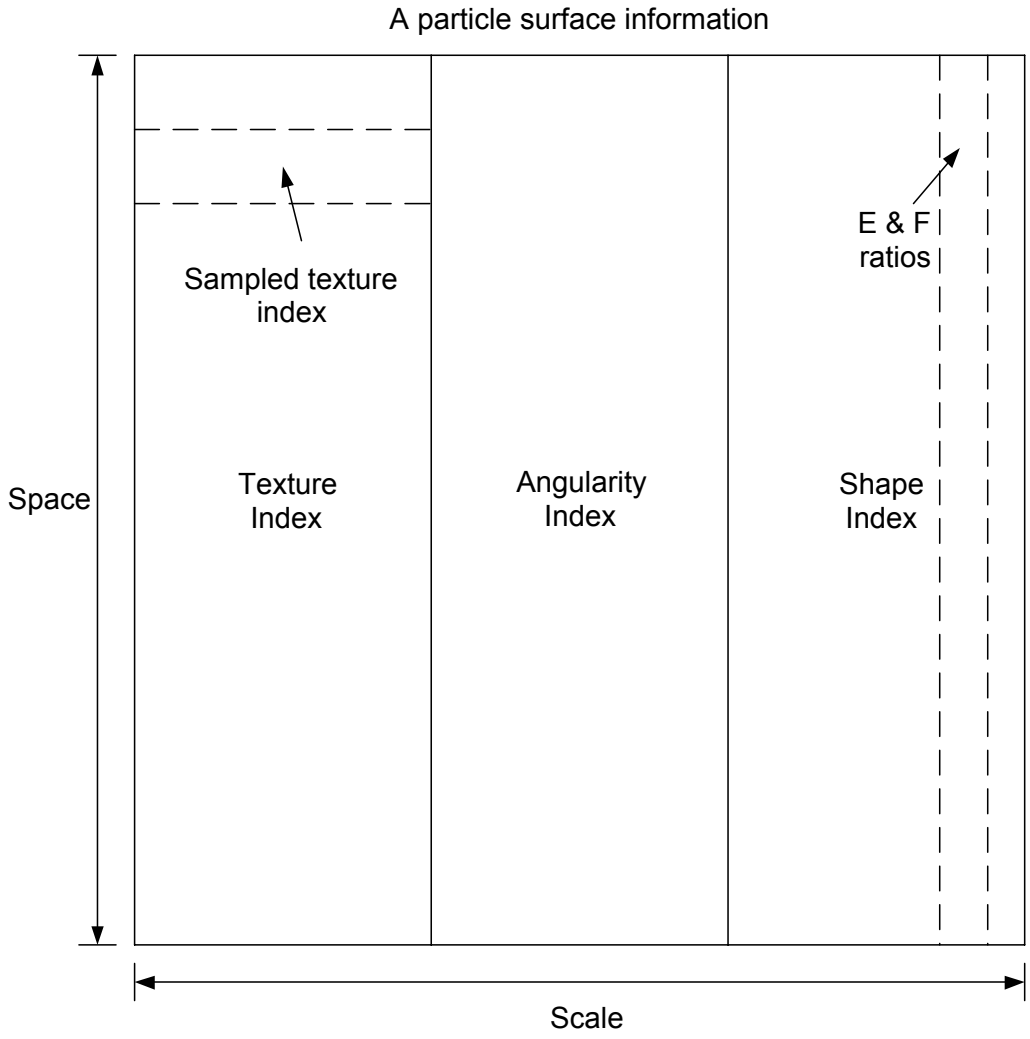

Figure 6.8: A particle information represented by the developed particle descriptors, elongation and flatness ratios, and a sampled texture index.

First, to test the shape index (Equation 6.24), the three principal dimensions of a particle were used to visually classify particles in terms of shape. Twenty particles were identified as equidimensional and another 20 particles as flat or elongated. The average flatness and elongation ratios of the equidimensional group were both 1.3 and 1.3, while those for the flat or elongated group were 2.5 and 2.2, respectively. Figure 6.9 (a) and (b) show a particle of the equidimensional group and a particle of the flat or elongated group, respectively. After the wavelet transform was conducted on data from the 40 particles, the shape indices were calculated for each particle. Figure 6.10 shows excellent correlation between the wavelet shape indices and the visual classifications based on the flatness and elongation criteria. To test the angularity index (Equation 6.25), 20 round particles and 20 angular particles were selected. Particles that had sharp edges and relatively plane sides with unpolished surfaces (as defined in ASTM D 2488) were classified as angular, whereas particles with no apparent edge were considered round. Figure 6.11 (a) and (b) show a round particle and an angular particle, respectively. As can be seen in Figure 6.12, the angularity indices show strong agreement with this visual perception of angularity. The same approach was taken in evaluating the surface index (Equation 6.26). Based on the visual inspections with such criteria as the degree of fineness and uniformity, two groups of 20 particles each were formed: one was smooth and the other was rough. Figure 6.13 (a) and (b) show a smooth particle and a rough particle, respectively. Figure 6.14 also shows high correlation between the surface indices

and visual classifications, demonstrating that the wavelet-based descriptor is a promising tool to measure particle surface texture.

One feature that is common to Figures 6.10, 6.12, and 6.14 is that there are large ranges of particle indices that belong to one group of particles. For example, as can be seen in Figure 6.9, the largest angularity index (3918) in the angular particle group is twice as high as the smallest angularity index (1954) in the same group. This implies that although all these particles were visually classified as angular, big differences exist in angularity. While the angularity index appears to capture this variation, it is difficult to rank the particles using only human visual perception. This indicates that the developed indices can quantify properties that are not recognizable by human visual perception.

(a) (b)

Figure 6.9: Test samples for shape index: (a) An equidimensional particle; (b) A flat and elongated particle.

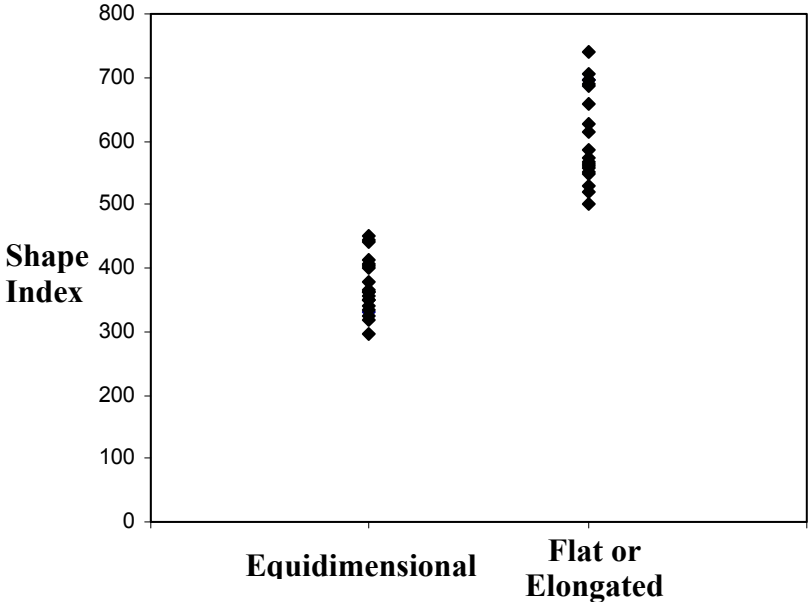

Figure 6.10: Correlation between shape index and visual inspection of shape.

(a) (b)

Figure 6.11: Test samples for angularity index: (a) A round particle; (b) A angular particle

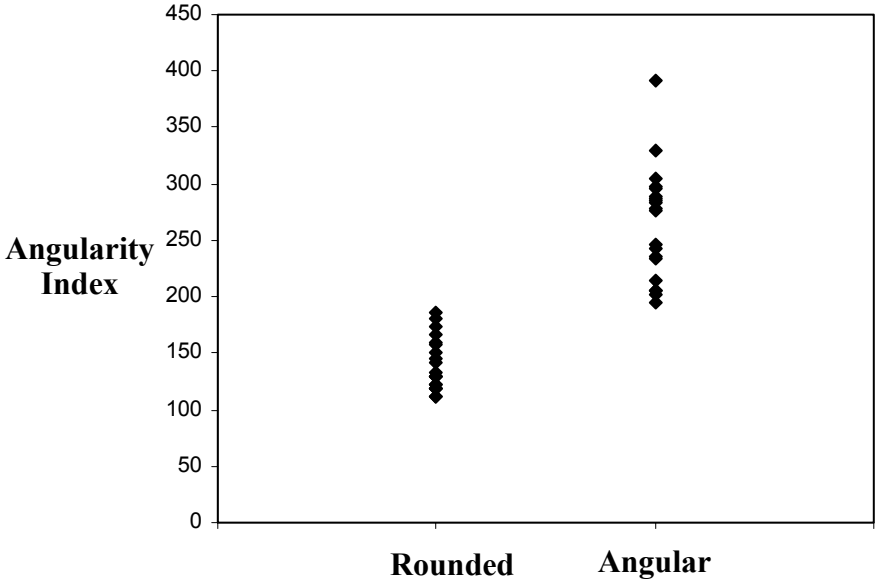

Figure 6.12: Correlation between angularity index and visual inspection of angularity.

(a) (b)

Figure 6.13: Test samples for texture index: (a) A smooth particles; (b) A rough particles

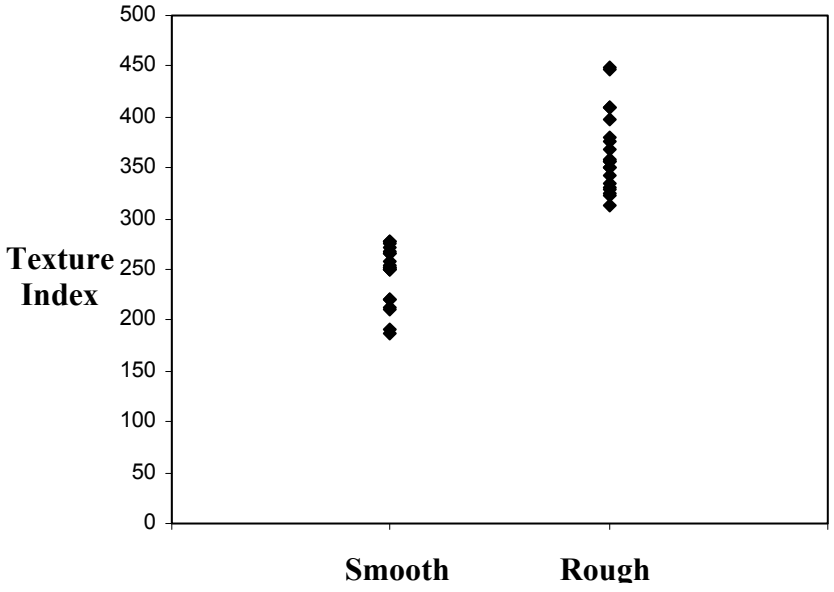

Figure 6.14: Correlation between texture index and visual inspection of texture.

CHAPTER 7
IMPLEMENTATION STRATEGIES

In this chapter, several aspects of implementing a rapid aggregate characterization system are addressed. Section 7.1 first reviews common layouts of aggregate, asphalt, and concrete plants to develop a better idea of how fast aggregate characterization technology could be incorporated with conventional processing equipment. Section 7.2 then suggests a modular system architecture that provides the flexibility needed to easily integrate an automated characterization system into a wide variety of plant applications, while section 7.3 identifies advantageous locations for obtaining aggregate samples and positioning data acquisition units in different aggregate handling plants. Finally, this chapter discusses several advantages of a fast aggregate characterization system in section 7.4.

7.1 DISCUSSION OF AGGREGATE, ASPHALT, AND CONCRETE PLANTS

7.1.1 Aggregate Plants

There is no single distinctive arrangement for aggregate crushing and sorting plants. Configurations of these plants depend on the quarry site environment, properties of aggregate material, selection of equipment, and so on. An example of a segmented fractionating plant, which can produce 500 tons per hour (tph) is illustrated as a flow diagram in Figure 7.1. A fractionating plant is designed to produce separate aggregate piles with nearly equal aggregate sizes in

each pile. A fractionating plant is one of the better processing alternatives for controlling segregation (National Stone Association, 1993).

As seen in Figure 7.1, the raw aggregate, obtained through either quarry blasting or natural aggregate extraction, goes through a vibrating grizzly feeder where unsound material is separated. Particles that pass through the grizzly feeder proceed to a jaw crusher at the primary station. Then, the aggregates go though a series of screening and crushing units to separate and produce particles of different sizes. Aggregates are transported from one station to another using belt conveyors, elevators, and/or screw conveyors.

Several surge piles and surge bins are shown in Figure 7.1. The purpose of an in-process surge pile is to isolate the systems on both sides from each other. Without a surge pile, the erratic production rate coming from the primary station can at moments exceed the secondary station's capacity, and later feed it nothing (National Stone Association 1993).

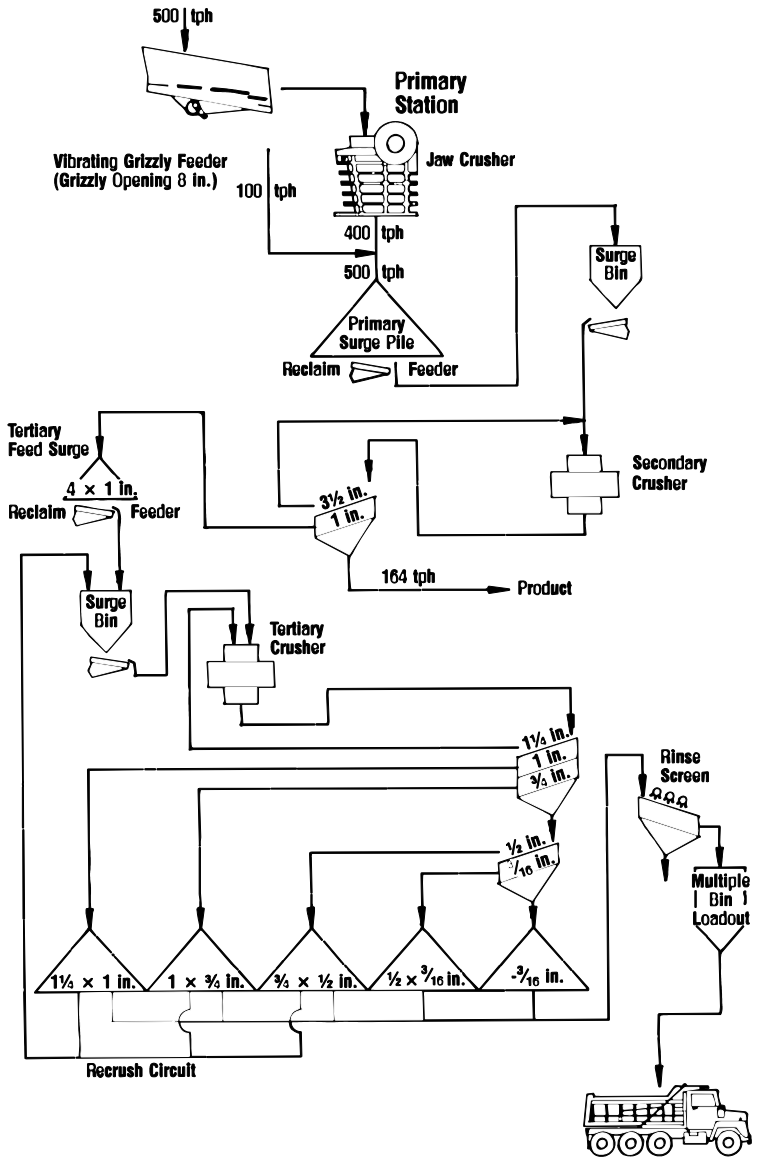

Figure 7.1: Segmented fractionating plant for producing graded, unbound aggregate (National Stone Association 1993).

Selection of the crusher type can be customized according to the aggregate material, the size of aggregate product, the production rate, and so on. There are basically four types of crushers: jaw crushers, gyratory crushers, roll crushers, and impact crushers. Basically, jaw, gyratory, and roll crushers are compression-type machines that apply a compressive force to rock trapped between their crushing surfaces, whereas impact crushers apply a high speed impact force to the feed rock. It is generally conceded that impact and gyratory crushers can provide relatively cubic products that are favored in the construction industry.

Aggregate processing usually includes washing to remove salt, clay, dirt, or crusher dust particles. In general, high-pressure spray nozzles are used effectively to rinse coarse aggregate over a vibrating, inclined screen. When rinsing alone is insufficient to clean the aggregate, screw washers, log washers, or rotary scrubbers can be used.

7.1.2 Hot-Mix Asphalt Plants

There are three basic types of hot-mix asphalt plants currently in use in the United States: batch plants, drum mix plants, and continuous plants. As depicted in Figure 7.2, asphalt concrete batch plants consist of five major components: aggregate feed system, aggregate dryer, asphalt cement supply system, mixing tower, and emission-control system. The aggregate feed system begins with cold bins containing batches of aggregate in various size ranges. The contents of each bin are proportioned into the mix by the size of the cold feed gate opening at the base of the bins or by use of a variable-speed belt feeder. The combined

aggregates taken from the cold bins go to the cold elevator that carries the mix up to the dryer. After the aggregate passes through the dryer, the material is fed via a hot elevator to screening units, where the aggregates are separated into the hot bins according to size. Next, the correct proportion of each aggregate is fed into the weigh box, and the aggregates go to the pugmill where they are mixed with asphalt cement.

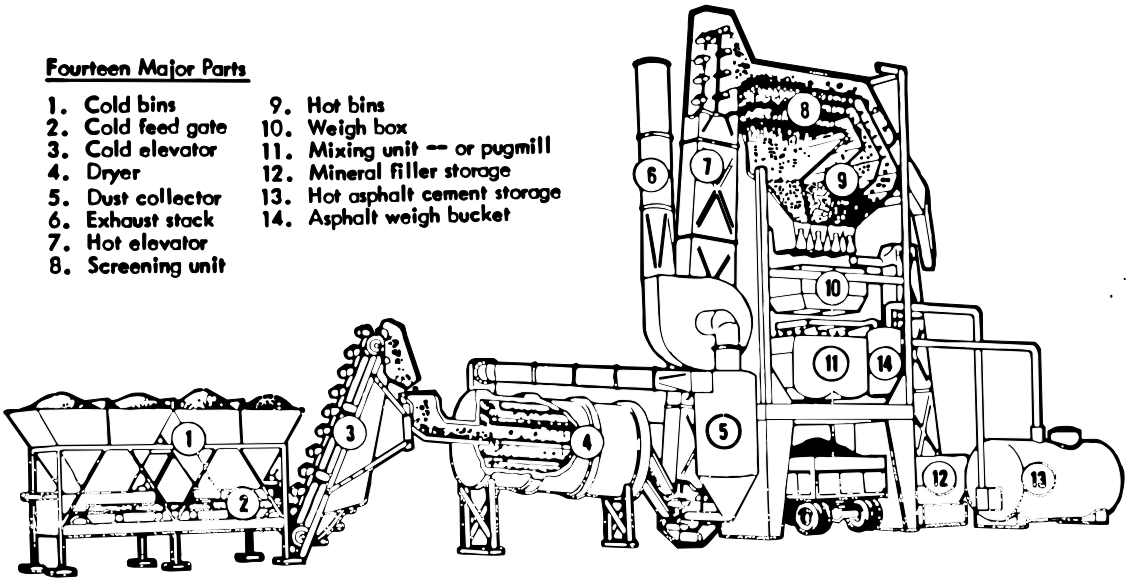

Figure 7.2: Batch asphalt concrete plant (Asphalt Institute 1986).

Figure 7.3 shows a continuous mix plant. This type of plant is similar to the batch plant except that the aggregate is continuously removed from the hot bins and transported to the pugmill, without a weigh box.

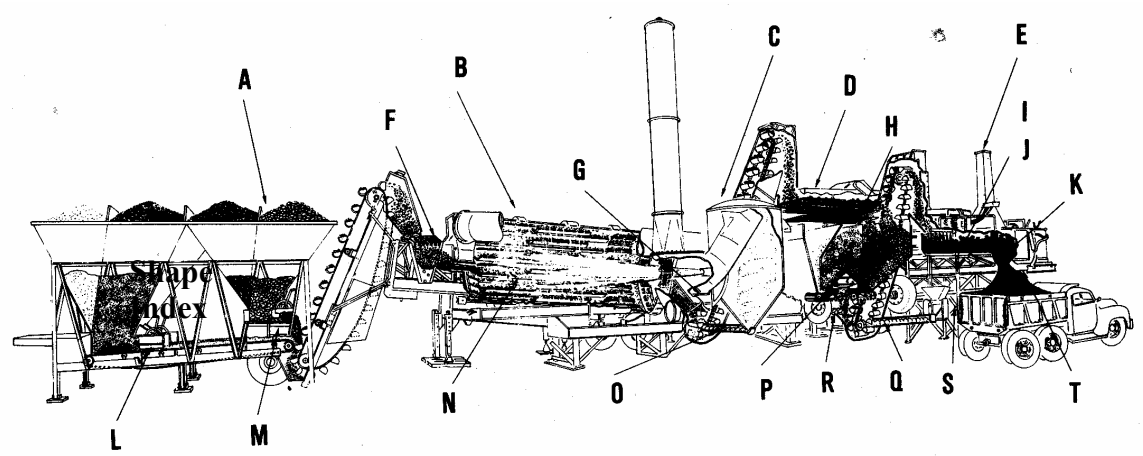

A Cold aggregate storage and feed; B Dryer; C Dust collector; D Gradation control unit; E Mixer; F Grizzly; G Fan; H Vibrating screen; I Transfer pump; J Pugmill; K Pugmill jacket; L Belt feeder; M Reciprocating feeder; N Flights; O Collected fines; P Gates; Q Mineral filler feed; R Aggregate sample point; S Metering pump; T Discharge Hopper

Figure 7.3: Continuous mix asphalt concrete plant (Asphalt Institute 1986).

A drum mix plant (Figure 7.4) does not have hot aggregate screens, hot bins, or a pugmill mixer. The components of this plant include a cold feed system, a rotating drum dryer, an asphalt proportioning and dispensing system, and a mix surge silo. The aggregate is dried, heated, and mixed with asphalt cement in the drum mixer. As shown in Figure 7.4, aggregates of selected sizes are taken from the cold feed bins and transferred to the cold feed conveyor for transport to the drum mixer. Proportioning of different aggregate sizes in the mix is controlled by the rate of withdrawal from each cold feed bin. The feed material is not thoroughly mixed prior to entering the drum mixer. The weight and speed of the moving aggregates are measured on the charging conveyor to compute the production rate. Elimination of aggregate screens, hot bins, and the pugmill mixer is to increase productivity significantly (Asphalt Institute 1986).

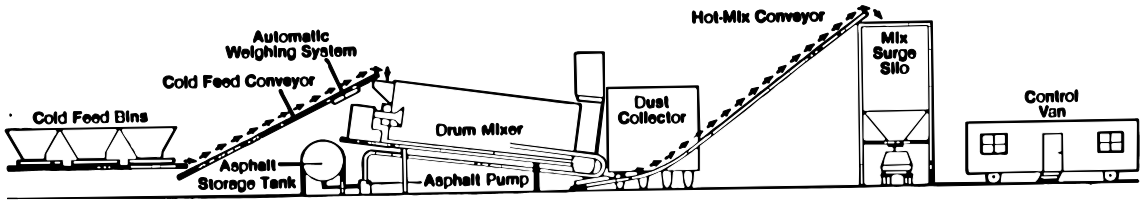

Figure 7.4: Drum mix asphalt concrete plant (from Asphalt Institute, 1986)

7.1.3 Portland Cement Concrete Plants

There are many ways to classify portland cement concrete plants. First, concrete plants can be categorized into mass concrete, paving concrete, ready-mix concrete, or concrete products plants, based on the material produced. Second, whether or not the concrete is mixed before discharge into vehicles divides concrete plants into dry plants (truck mix plants) (Figures 7.5 and 7.6) and wet plants (central mix plants) (Figure 7.7). Dry plants feed the batched materials to truck mixers where water is added and mixed, whereas wet plants produce thoroughly mixed concrete. Third, plants can be divided into permanent and mobile plants. Finally, depending on the location of the aggregate bins in the plant, concrete plants are classified as gravity plants (tower plants) (Figure 7.5) or low-profile plants (Figures 7.6 and 7.7). In gravity plants, materials flow continuously downward as they are processed, whereas in low-profile plants, the aggregates are elevated by conveyor after proportioning (Dobrowolski 1998).

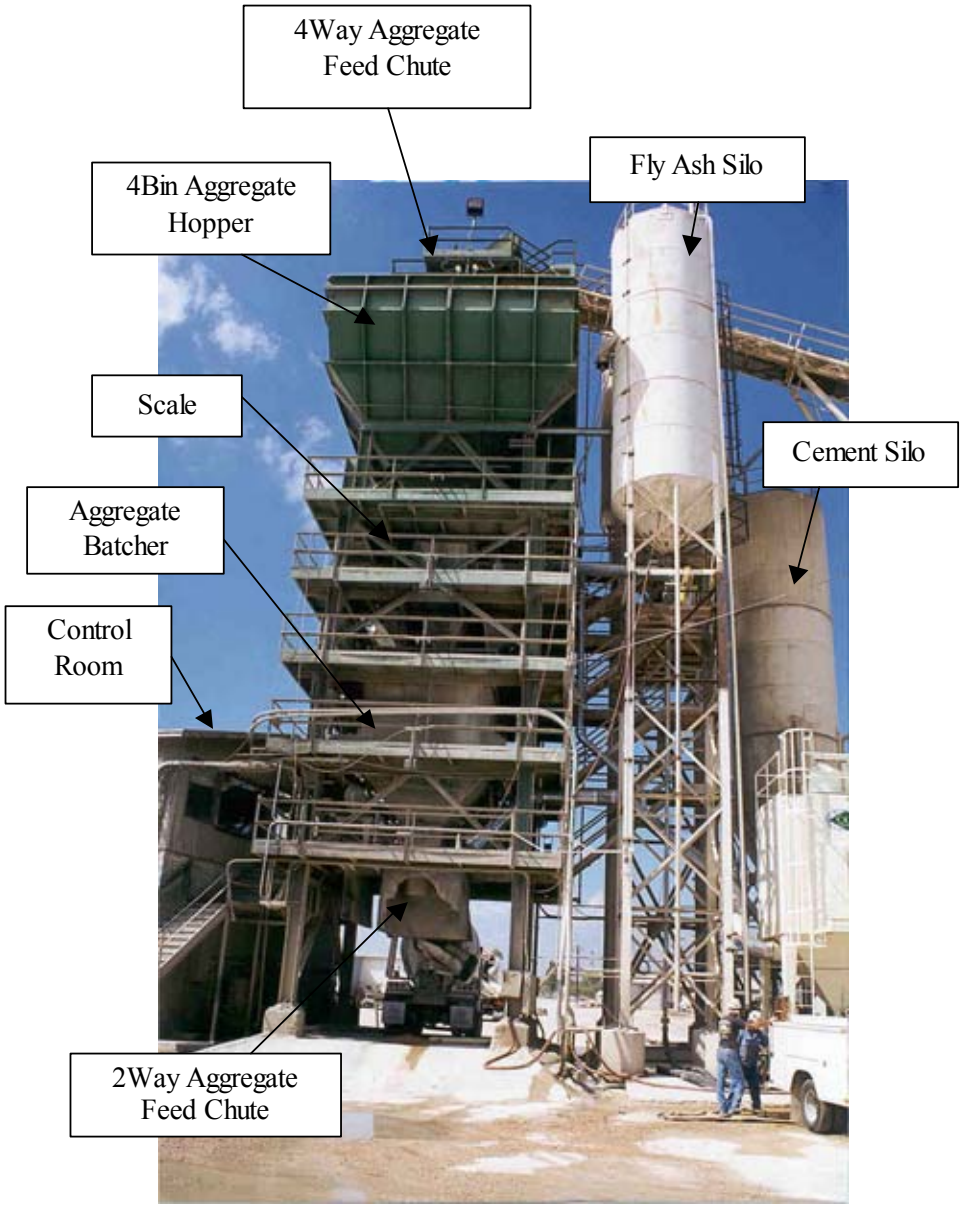

Figure 7.5: Gravity fed dry portland cement concrete plant (Capital Aggregates of Austin, Texas 1999).

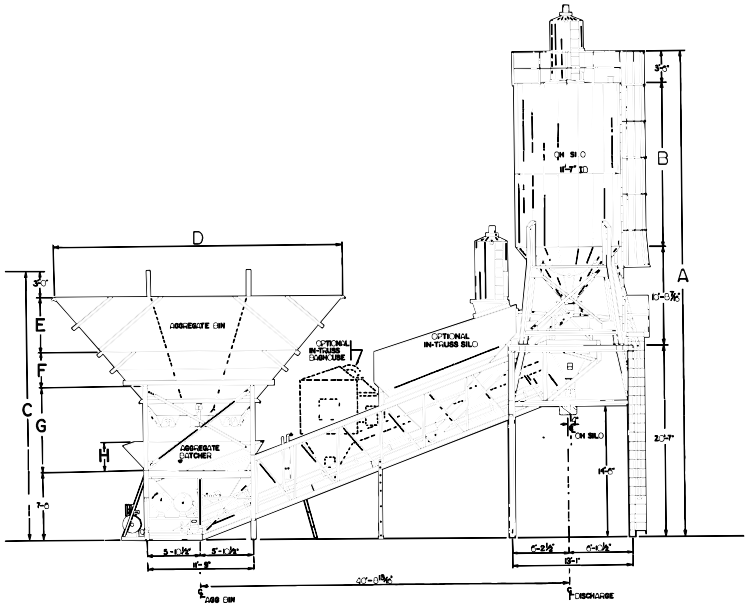

Figure 7.6: A low profile dry concrete mix plant (Vince Hagen Company 1999).

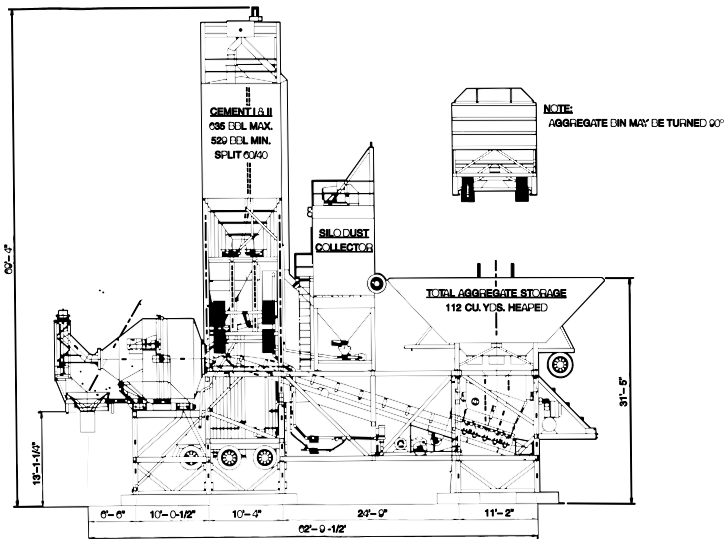

Figure 7.7: A low profile wet concrete mix plant (Concrete Equipment Company 1999).

7.2 MODULAR SYSTEM ARCHITECTURE

Automated characterization systems should be designed to allow for optimum performance in a variety of aggregate plant installations. Efforts should be focused on developing components with enough flexibility to allow simple customization to a given plant configuration. The sampling process also seems to be essential in order to effectively characterize the whole aggregate which is transported by conveyor belts at a speed of up to 80 m per minute (National Stone Association 1993). A good approach would be to design a system based on a Data Acquisition Unit (DAU) that incorporates the sample preparation and scanning functions in one unit. As indicated in Figure 7.8, the sample acquisition and data analysis functions would be accomplished outside of the DAU. This basic architecture is used in the PPMS system built by Scientific Industrial Automation (Dumitru and Browne 1999).

In an industrial application, aggregate samples would be acquired from a selected position and delivered to the DAU. The arrangement of the sample acquisition and delivery system will depend on the plant configuration, but can be easily designed and customized using off-the-shelf aggregate equipment. For example, a simple diversion chute could be used to capture periodic samples of material being transferred from one conveyor belt to another. Alternatively, a belt sweep sampler might be used. Because sample acquisition and delivery is handled separately, the DAU could be more readily incorporated into the unique constraints of a wide variety of potential industrial applications. Furthermore, the

same DAU could be easily adapted for use in the laboratory with samples obtained manually.

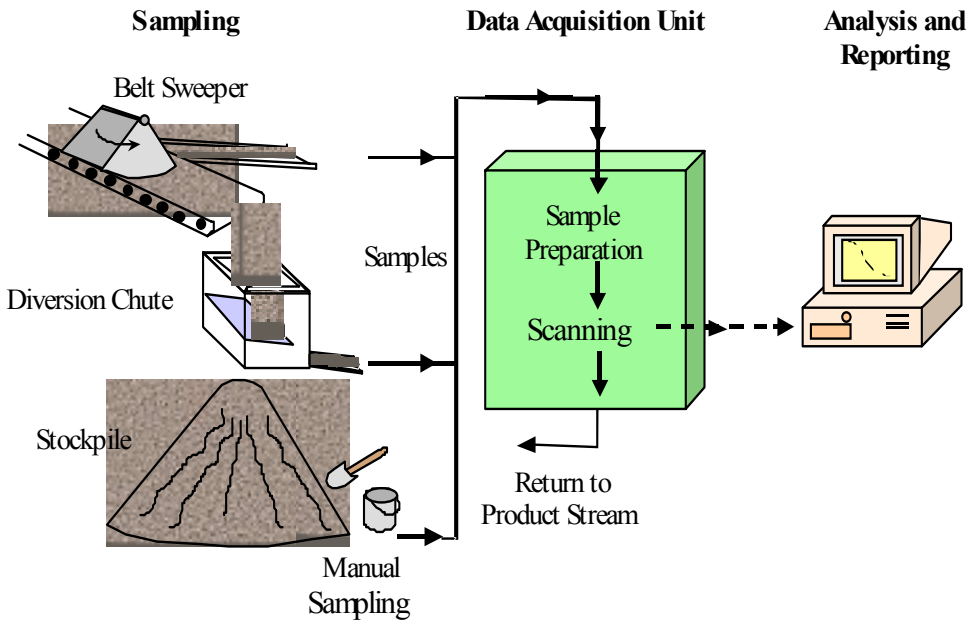

Figure 7.8: Schematic overview of a rapid system for measuring aggregate properties based on the concept of DAU.

Inside the DAU box, the aggregate sample would be processed and scanned as suggested in the conceptual design shown in Figure 7.9. Material would enter the DAU through a chute, possibly dried, spread out for scanning, passed before the scanning device, and dumped into a discharge chute. In Figure 7.9, scanners are shown in two possible locations for scanning material spread out on a conveyor belt or scanning material as it drops through the air. Only one scanner location would probably be used in a given DAU but the choice of the

equipment layout may depend on the type of scanner used and the range in size of the particles being scanned.

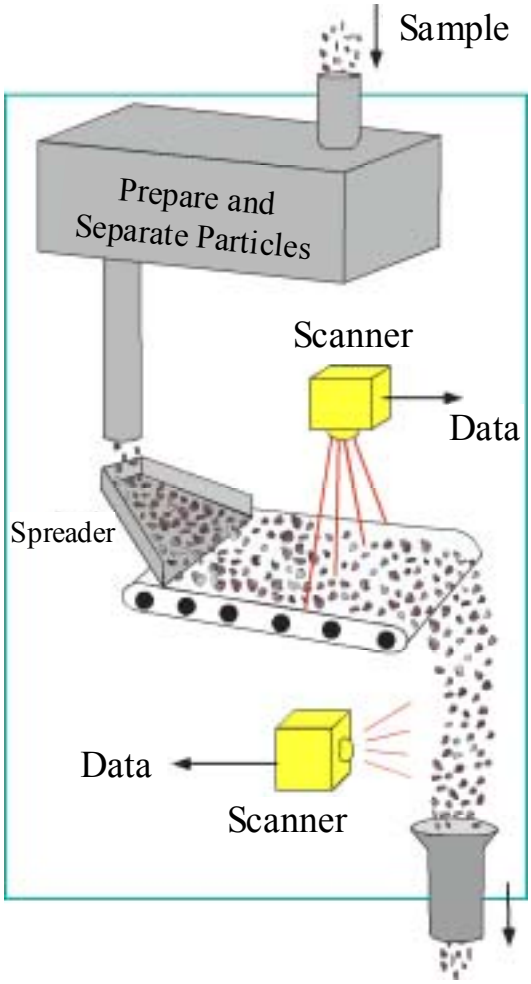

Figure 7.9: Conceptual design of a DAU showing two possible arrangements for rapidly scanning aggregate particles.

One may need two different DAU designs; one optimized for scanning fine aggregates and a second optimized for scanning coarse aggregates. The basic layout of these two DAUs may be very similar, or may incorporate two different types of scanners. For example, the LASS can be used for the quality control of coarse aggregates where dimensional ratios of the aggregates need to be monitored, while a 2D digital image based system can be used to mainly control the size of fine aggregates. If one needs to determine the gradation of mixed aggregate products, two separate DAUs could be installed side-by-side, with a simple screening device used to split the material by size between the two DAUs. The resulting data could then be re-combined automatically to yield the composite grain size distribution.

As indicated in Figure 7.10, data from multiple DAUs at different locations in a plant would be transmitted to a single computer to perform the data analysis and reporting. The result would be a distributed network of devices, with a central data collection/processing unit to monitor various sectors of a plant. In Figure 7.10, a network of three DAUs at a mixing plant is depicted. Here, the DAUs are positioned to measure the gradation of material being delivered to three charge bins. This conceptual system would also have the capability to actively control and adjust the mixed product by controlling the ratios of material being withdrawn from each charge bin.

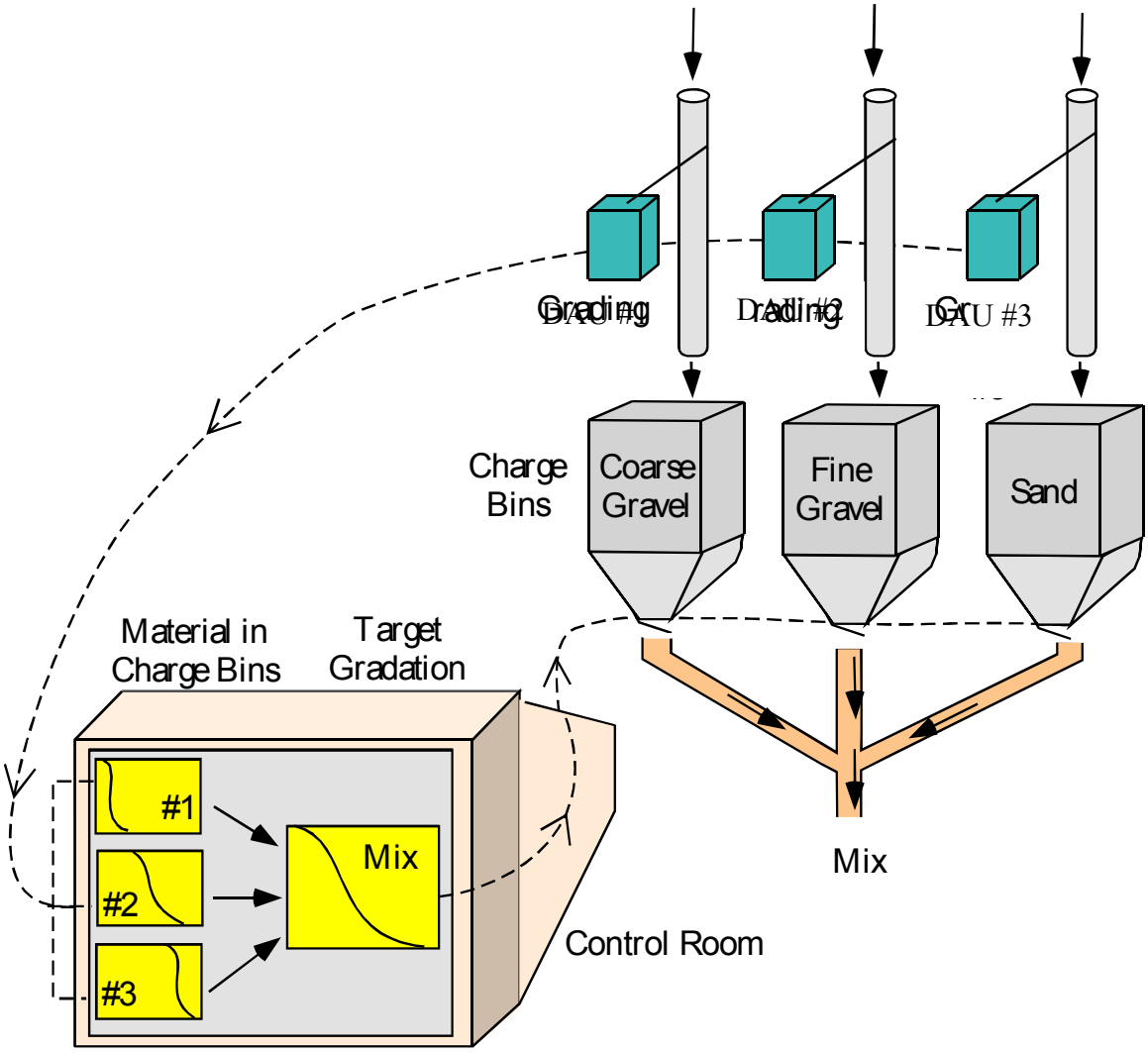

Figure 7.10: A distributed network of three DAUs used to actively adjust the mixture of material from three aggregate charge bins.

7.3 SAMPLING LOCATION

As pointed out above, it may not be feasible to design a single DAU that can accurately scan aggregates over a very wide range of particle size. Hence, when a rapid characterization device is needed to scan the range of material produced by a crusher, it may be necessary to first split the sample into appropriate size ranges and feed this material into two or more DAUs working in parallel. On the other hand, many aggregate plants, as well as most portland cement concrete and asphalt concrete plants, use a weight batching system to control the gradation of a given mixed product. As long as the weight or flow rate (weight per time) of a certain constituent is known, the desired mix can be achieved by controlling the blend of the different constituents. Hence, these plants process aggregates that have been sorted into somewhat narrow ranges of particle size. In these operations, an automated characterization device can take advantage of the narrower size ranges found in the sorted material being processed.

Given a very wide variety of layouts for different aggregate processing plants, the two most advantageous sampling locations appear to be:

- after final screening as unbound aggregates are sent to sorted stockpiles, and
- where sorted aggregates are fed to a mix plant, either from stockpiles or charge bins.

These potential sampling locations in an aggregate sorting plant, a ready-mix concrete plant, and a hot-mix asphalt plant are depicted in Figure 7.11.

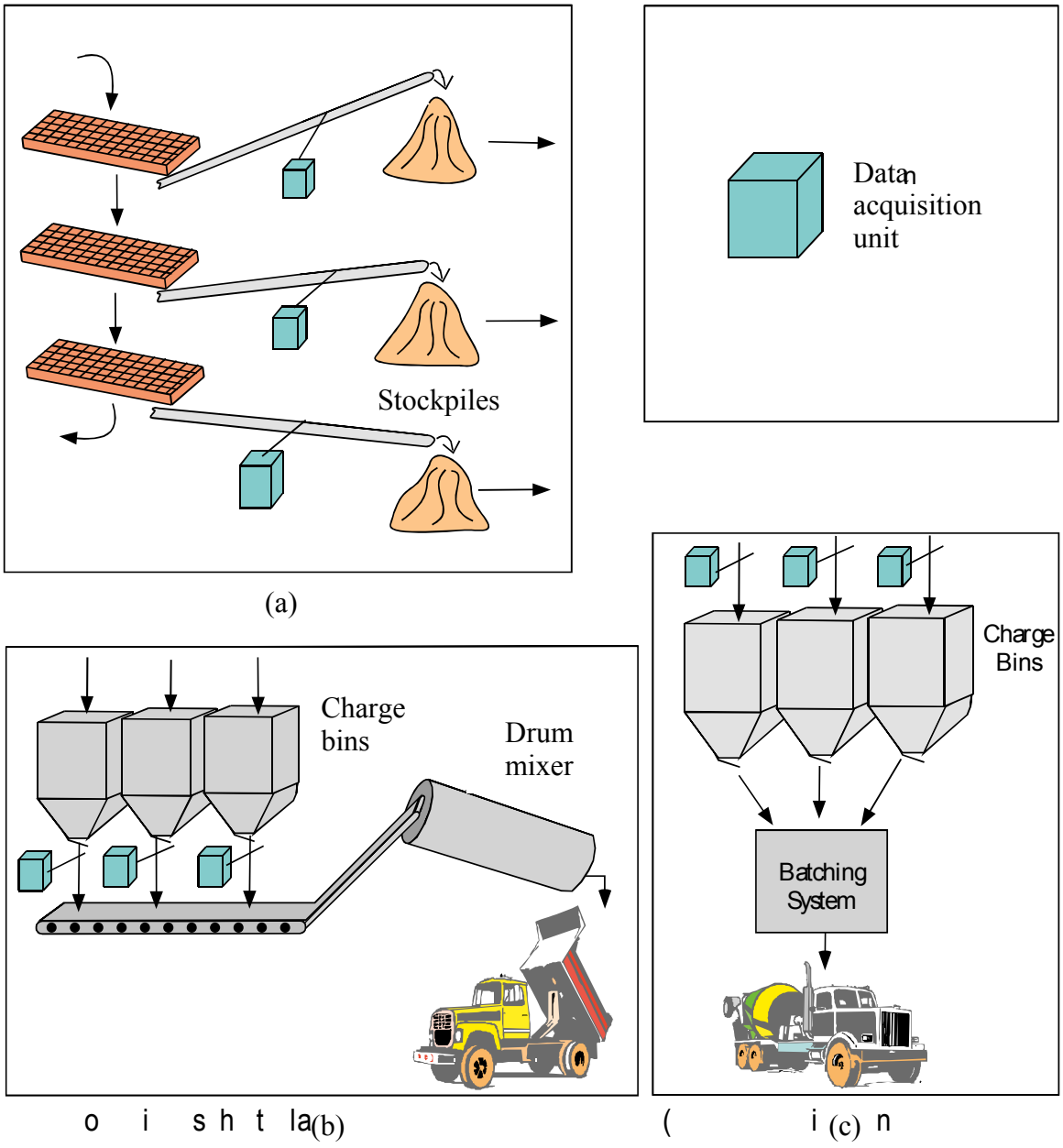

Figure 7.11: Advantageous locations for obtaining aggregate samples and positioning DAUs in different aggregate handling plants: (a) aggregate production plant; (b) hot-mix asphalt plant; (c) ready-mix concrete plant.

Having aggregate samples that are already sorted into somewhat narrow size ranges is advantageous to the design of a DAU. That is, knowing the material will be in some particular size range allows one to design and calibrate the test equipment for optimum scan resolution and speed. In addition, if the aggregate products are adequately rinsed in the production process prior to being sampled, the washing process can be omitted from the DAU operations. Furthermore, the highlighted sampling locations would yield data that could be used for real-time quality control of the plant production by helping to identify problems in the plant operation. Also, scanning the material before it is fully mixed would allow for real-time adjustments to the mix proportions to achieve better control of the final aggregate characteristics.

7.4 ACCURACY OF RAPID CHRACTERIZATION DATA

One can surmise that rapid measurements are likely to yield characterization data that is less precise than that obtained using such conventional methods as sieves and proportional calipers. This is mainly because they are the standardized methods to which other methods need to be compared. However, to be practical, a rapid characterization of particles must have a comparable degree of overall accuracy. For example, while the precision of an automated system may not be as high as a sieve analysis, the capability to characterize grain size in a fast manner may lead to a more representative measurement of aggregate gradation. Three reasons why a rapid measurement

system may yield a better overall measure of grain size are illustrated in Figure 7.12 and discussed below.

As depicted in Figure 7.12 (a), rapid measurements facilitate more frequent sampling of the product stream, which permits better tracking of variations in aggregate characteristics. Changes in the parent material composition, production rates, and plant machinery can all contribute to variations in the produced aggregate characteristics (National Stone Association 1993). To monitor changes in aggregate quality resulting from these variations, sampling must be carried out with sufficient frequency. According to ASTM E 122 (1997), the minimum random sample size needed to determine gradation to within a desired accuracy is proportional to the estimated variation within a given material lot. Hence, when the standard deviation is large, the sample size should be increased to obtain the equivalent level of accuracy. If the gradation of the product stream is changing with respect to time, as indicated in Figure 7.12 (a), more frequent sampling is needed to track these changes. Thus, rapid measurements can be seen to yield a more accurate picture of varying product gradation.

Rapid measurements also make it feasible to test much larger aggregate samples. As illustrated in Figure 7.12 (b), a larger sample size leads to an increased confidence that the measured gradation is in fact representative of the entire population. This concept is embodied by the central limit theorem: if all samples of size n are selected from a population with a finite mean u and standard deviation s, then as n is increased, the distribution of sample means

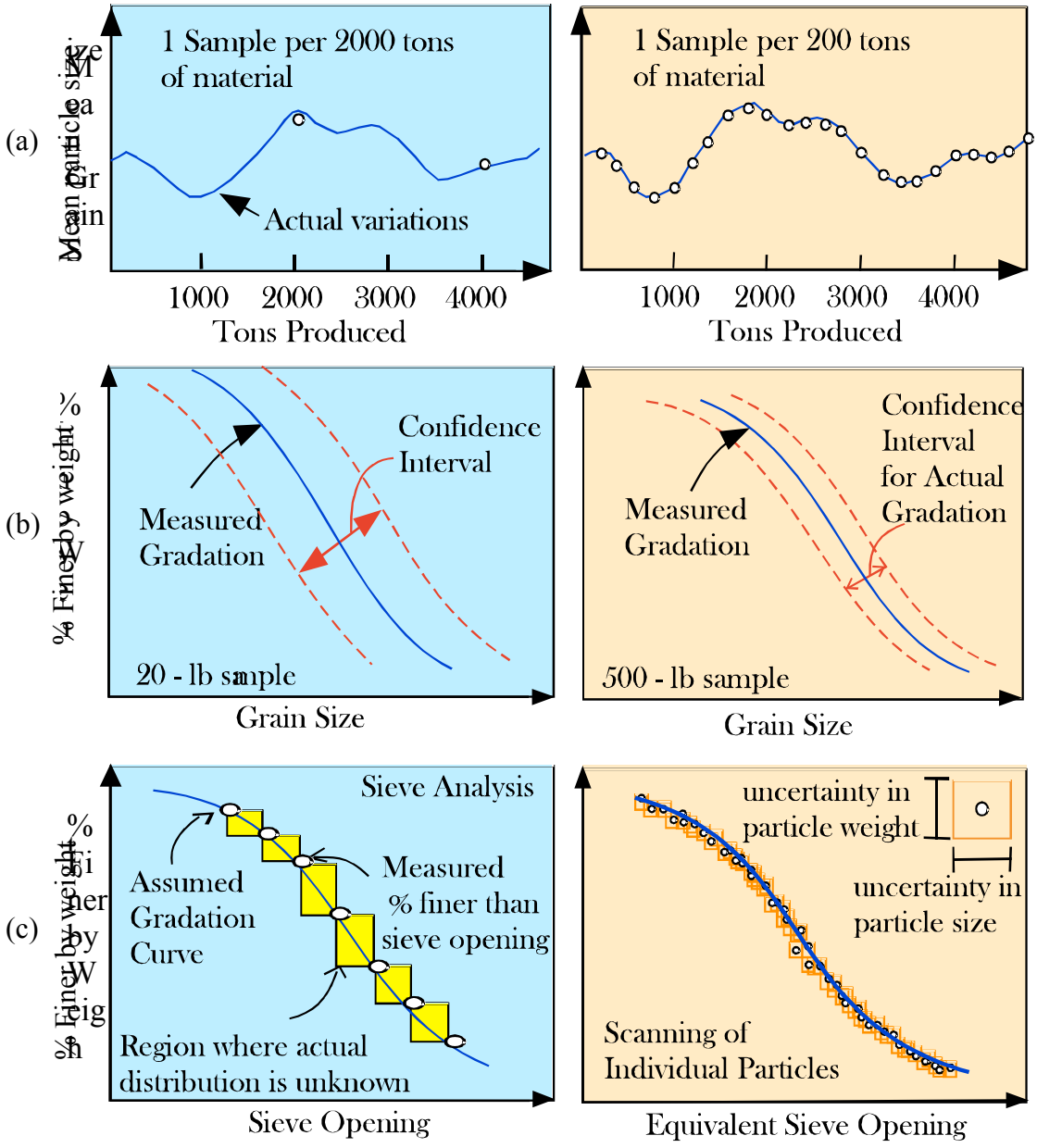

Figure 7.12: Conceptual depiction of why a rapid gradation device will yield better information than can be obtained from conventional sieve analyses.

will tend toward a normal distribution with a mean of n and a standard deviation equal to $s/\sqrt{n}$ (Cangelosi et al. 1983). That is, the larger the sample size, the narrower the confidence interval becomes. Hence, as indicated in Figure 7.12 (b), the grain size distribution of a 500-lb sample will be closer to the actual gradation of the population than the gradation obtained from a 20-lb sample.

A third advantage associated with rapid techniques is illustrated in Figure 7.12 (c). Here, a more precise measure of gradation is obtained because each particle is individually sized, instead of grouping particles that fall between two sieve sizes. Grain size distribution is usually expressed as a percent by weight of the total quantity of aggregate tested that passes a series of standard sieve sizes. In a sieve analysis, data is obtained only for each discrete sieve opening size and interpolation is used to draw the gradation curve. However, no data is obtained on the size of particles lying between two adjacent sieves and the actual gradation is unknown within the boxes shown in Figure 7.12 (c). In contrast, rapid gradation techniques generally involve scanning individual particles and estimating their equivalent size and shape. While these estimated particle dimensions also have some associated uncertainty, measuring the size of each particle yields a more precise determination of the overall gradation, as depicted in Figure 7.12 (c).

A new aggregate characterization system provides an efficient way to characterize construction aggregates. The LASS can measure various aggregate properties such as size, shape, angularity, and texture in a fast, accurate, and reliable manner. When implemented in aggregate plants, HMA plants, concrete plants, or large construction sites, this ability to automatically analyze multiple

characteristics of an aggregate sample is expected to have the following potential benefits:

- Improved reliability in the measured aggregate properties as a result of testing more frequent and larger samples of the product stream
- Reduced labor costs relating to all aspects of aggregate testing
- Improved worker safety from reducing the need to be exposed to chemically harmful stone material
- Decreased production of unacceptable material through prompt adjustment of the production process based on real-time measurements
- Tighter control of aggregate quality based on accurate and complete information

CHAPTER 8
CONCLUSIONS AND RECOMMENDATIONS

This chapter summarizes the accomplishments of the research objectives and presents conclusions. The contributions and the recommendations for future research are then discussed.

8.1 SUMMARY

The main objective of this research was to develop a method to measure various morphological characteristics of construction aggregates in a fast, accurate, and reliable manner. For this purpose, the focus of this research was on laser profiling based hardware, 3D image creation, particle segmentation algorithms, particle measurement algorithms, and generalized 3D particle descriptors.

Chapter 3 described the LASS hardware system architecture along with a discussion of the laser profiling mechanism. It also explained how all the components of the LASS are controlled and integrated with customized software. In addition, a simple 3D image creation algorithm was presented that allows for efficient data storage without critical information loss.

In Chapter 4, an algorithm for segmenting a particle image acquired through laser profiling was developed using a Canny edge detector and a watershed transformation. Canny edges with rigorous and liberal threshold values were used to outline particle boundaries on a binary image and to check the

validity of the watersheds, respectively. To find appropriate regional minima in the watershed transformation, a varying search window method was used, where the number of neighboring pixels being compared with the pixel of interest was determined from the height value of the pixel. When implemented in automated systems that are designed to rapidly assess size and shape characteristics of stone particles, this technique can increase the accuracy of the analysis results as well as save time required for aggregate preparation.

Chapter 5 described a virtual particle measurement method to provide particle shape and size parameters that correlate to results of ASTM D 4791 (Standard test method for flat particles, elongated particles, or flat and elongated particles in coarse aggregate) and ASTM C 136 (Standard test method for sieve analysis of find and coarse aggregates). In the "virtual caliper" and "virtual sieve" methods developed, the 3D data captured on each particle are rotated about different axes to determine dimensional ratios and the smallest mesh opening size through which the particle can pass. Comparisons between the manual measurements of the standardized methods and the results from the LASS showed excellent agreement.

Chapter 6 presented the development of wavelet-based 3D particle descriptors. Aided by the multi-resolution analysis feature of the wavelet transform, these descriptors provide generalized, comprehensive, and objective ways of describing aggregate particles. Tests with this method produced data that shows strong correlation between the particle descriptors and visual perception of the aggregate's morphological properties. These results demonstrate that the

wavelet-based approach is a promising tool for quantifying such important aggregate properties as size, shape, angularity, and surface texture.

In Chapter 7, several issues related to the implementation of a fast aggregate characterization system were addressed. A modular system architecture that provides the flexibility needed to easily integrate an automated testing system into a wide variety of plant applications was suggested. This chapter also discussed such issues as potential sampling locations in aggregate handling plants, advantages gained from a distributed network of data acquisition units and from scanning large and frequent product samples, and economics.

8.2 CONCLUSIONS

Based on the work, the following four conclusions can be made.

1. The shape analysis algorithm developed to measure particle dimensional ratios such as elongation ratio and flatness ratio, is computationally efficient and accurate.
2. The 3D particle indices measured from various properties of aggregate particles correlate well with human visual perceptions.
3. The segmentation algorithm that was developed can separate irregular particles in an image acquired from laser profiling in a robust manner.
4. The laser based 3D measurement method can provide fast and accurate automated aggregate characterization, despite the computationally complex procedure required to handle the 3D data.

8.3 CONTRIBUTIONS

The physical outcome of this study is the Laser-based Aggregate Scanning System (LASS) that can characterize aggregate particles in a fast, accurate, and reliable manner. The main contributions of this research to the body of knowledge are as follows:

1. This study provided guidelines for designing and developing 3D automated particle measurement systems, from the selection of hardware components to algorithm development.
2. The proposed generalized 3D particle descriptors provide a comprehensive framework through which various morphological properties of a particle can be objectively defined and accurately quantified.
3. The 3D image creation algorithm demonstrated that 3D laser scan data could be stored in a 2D image format without losing critical information.
4. The particle shape analysis algorithm (virtual caliper) demonstrated that fast and accurate measurement of a particle shape is possible by converting a computationally expensive 3D problem into a simpler 2D problem.

The LASS can also be applicable to other industries such as mining, food, pharmaceuticals, plastics, steel, etc. where particles need to be characterized for product quality control. For example, the steel industry needs continuous and accurate measurement of sinter and coke to optimize steel production (Dumitru et al. 1999). The research steps in this report can serve as a model for developing

automated quality control systems for those industries, in addition to the aggregate industry.

8.4 RECOMMENDATIONS

In this report, 200 particles, 10 aggregate samples (eight 6 kg samples and two 15 kg samples), and 120 particles were used to evaluate the validity of the particle shape measurement algorithm (virtual caliper), the particle gradation algorithm (virtual sieve) and the particle segmentation algorithm, and the particle descriptors, respectively. In the future, however, the applicability of those algorithms to aggregate characterization should be validated with more aggregate testing and related quantitative experiments. For thorough repeatability tests, the same aggregate samples need to be measured several times by different operators using the LASS with some time interval between each test. In particular, more rigorous evaluations of the descriptors are recommended to prove their size invariant characteristics. Artificial particles with properties that are easy to quantify may be effectively used for this purpose.

There are many interesting avenues for continued research. A few of them are listed in the following sections.

8.4.1 Artificial Intelligence Based Quality Control

If the LASS application is primarily concerned with variations in the product stream rather than complete characterization, a much faster method could be devised. For example, in aggregate production plants, the gradation of

aggregates is monitored based on variations in the percent passing a specified sieve size (National Stone Association 1993). Thus, by monitoring variances, plant operators can know whether the production process needs to be adjusted. The method of extracting only the variance information is likely to facilitate faster analysis because it does not require the complete particle characterization process of measuring all particles including the digital segmenting process.

If a group of aggregates is scanned and the acquired data is converted into a digital image, 2D wavelet transform can be effectively applied to the image. Such features as energies (summation of absolute values of all the elements) of wavelet coefficients at different decomposition levels could be obtained for the whole image. If the group of aggregate is out-of-specification, it is likely that the group's wavelet-based features would be different from those of an in-specification group. Therefore, by comparing those features between in-specification and out-of-specification images, any aggregate group with out-of-specification properties could be detected as unacceptable. Fuzzy logic based neural networks (neuro-fuzzy classifier) could be effectively used to classify the aggregates (Tsoukalas and Uhrig 1997).

8.4.2 Group Texture Analysis

Here, to distinguish the proposed research idea from particle surface texture, the word "group" is used with "texture analysis". The main objective of performing a sieve analysis is to see how well a group of particles can be compacted. To determine this property, the aggregate is divided into small size

ranges, using computational or physical division. Ideally, one would characterize a group of aggregates by the way it looks without going through the division process. This is because the way aggregate particles interact with each other as a group will eventually affect the construction structure. Developing a group texture quantification method that can correlate to performance of structure would be a worthwhile research.

8.4.3 Correlation of the 3D Particle Descriptors with Hot Mix Asphalt and Portland Cement Concrete Performance

The next stage of this research would be an effort to correlate the aggregate properties quantified using the laser-based approach with the behavior of hot mix asphalt (HMA) and portland cement concrete (PCC) mixes. By establishing strong correlation between them, it would be possible to identify positive and negative characteristics of aggregate particles, which could lead to better design and construction methods. For HMA mixes, such properties as resilient modulus, tensile strength, stability, etc. can be investigated, whereas compressive strength, tensile strength, elasticity modulus, shrinkage, creep, etc. can be tested for PCC mixes. As a prerequisite, the modified ASTM C 1252 for coarse aggregate is recommended to be used in order to get an understanding of the relationship between the uncompacted void content and the particle indices.

For this particular purpose, a laser scanner that has two cameras on both sides of the laser source is recommended. This would eliminate the need to scan the same particles twice in opposite directions and to merge the two images for

the purpose of minimizing data loss, leading to much faster and accurate particle characterization.

8.4.4 Comprehensive Economic Feasibility Study

As previously mentioned, the benefits of implementing automated aggregate characterization system most likely derive from gains in productivity through optimized plant operations and strategic gains due to an improved product quality. It would be useful to develop a simulation method or a predictive model that can estimate the potential productivity increase or the improved quality to some tangible economic gains. It is recommended that this proposed study also investigate the benefit of applying the LASS to other industries such as mining, food, pharmaceuticals, plastics, steel, and so on.

8.4.5 Commercialization

To commercialize the LASS, several hardware and software improvements are recommended. First, as visualized in the data acquisition unit in Chapter 7, a conveyor belt system can be added to the LASS. This belt system could be combined with a certain type of mechanical vibrator that can spread particles, such that each particle will have a good chance of being fully scanned. It would also be important to optimize the software to be more user-friendly, more rapid, and more robust.

REFERENCES

Agrawal, Y. C., McCave, I. N., and Riley, J. B. (1991). "Laser diffraction size analysis." *Principles, methods, and application of particle size analysis*, Cambridge University Press, New York, pp. 119-128.

Ahlrich, R. C. (1996). "Influence of aggregate properties on performance of heavy-duty hot-mix asphalt pavements." *Transportation Research Record 1547*, TRB, National Research Council, pp. 7-14.

Aljassar, A. H. (1994). "Automation of aggregate size-gradation analysis." PhD thesis, University of Waterloo, Ottawa, Canada.

Argenti, F, Alparone, L., and Benelli, G. (1990) "Fast algorithms for texture analysis using co-occurrence matrices." *Proc., Part F: Radar and Signal Processing,* IEE, pp. 443-448.

Asphalt Institute. (1986). *Asphalt Plant Manual*, College Park, Maryland.

ASTM. (1998). "Standard test method for uncompacted void content of fine aggregate (as influenced by Particle Shape, Surface Texture, and Grading)." *C 1252-98*, West Conshohoken, PA.

ASTM. (2001). "Standard test method for sieve analysis of find and coarse aggregates." *C 136-01*, West Conshohoken, PA.

ASTM. (2000). "Standard practice for description and identification of soils (visual-manual procedure)." *D 2488-00*, West Conshohoken, PA.

ASTM. (2000). "Standard test method for index of aggregate particle shape and texture." *D 3398-00*, West Conshohoken, PA.

ASTM. (1999). "Standard test method for flat particles, elongated particles, or flat and elongated particles in coarse aggregate." *D 4791-99*, West Conshohoken, PA.

ASTM. (2001). "Standard test method for determining the percentage of fractured particles in coarse aggregate." *D 5821-01*, West Conshohoken, PA.

ASTM. (1997). "Standard practice for choice of sample size to estimate the average for a characteristic of a lot or process." *E 122-97*, West Conshohocken, PA.

Bachman, G, Narici, L, and Beckenstein, E. (2000). *Fourier and wavelet analysis*, Springer-Verlag, New York, NY.

Barksdale R. D., and Y. I. Samir. (1989). "Influence of aggregate shape on base behavior." *Transportation Research Record 1227*, TRB, National Research Council, pp. 173-182.

Beckman Coulter. (1999). "Particle size characterization: Coulter LS200." <http://www.beckmancoulter.com/products/instrument/partChar/technology/PartSize.asp> (Jan. 4. 2002)

Beucher, S. (1991). "The watershed transformation applied to image segmentation." *Proc., 10th Pfefferkorn Conference on Signal and Image Processing in Microscopy and Microanalysis,* Cambridge, UK.

Beucher, S., and Lantuejoul, C. (1979). "Use of watersheds in contour detection." *Proc., Int. Workshop on Image Processing, Real-Time Edge and MotionDetection/Estimation,* Rennes, France.

Beucher, S., and Meyer, F. (1993). "The morphological approach to segmentation: the watershed transformation." *Mathematical morphology in image processing*, Marcel Dekker, Inc., New York, pp. 433-481.

Blatter, C. (1998), *Wavelets: A Primer*, A K Peters, Ltd, Natick, MA.

Bleau, A., and Leon, L. J. (2000). "Watershed-based segmentation and region merging." *Computer Vision and Image Understanding*, Academic Press, 77(3), pp. 317-370.

Brzezicki J. M. and Kasperkiewicz J. (1999). "Automatic image analysis in evaluation of aggregate shape." *Journal of Computing in Civil Engineering*, ASCE, 13(2), pp. 123-128.

Browne, C. (2001). "An evaluation of automated devices to replace and augment manual sieve analyses in determining aggregate gradation." Master Thesis, The University of Texas at Austin, Austin, Texas.

Browne, C., Rauch, A. F., Haas, C. T., and Kim, H. (2001). "Comparison tests of automated equipment for analyzing aggregate gradation." *Proc., 9th Annual Symposium,* ICAR*,* Austin, Texas.

Buchanan, M. S., and Brown, E. R. (1999). "Development and potential use of an automated aggregate gradation device." *Proc., 78th Annual Meeting,* TRB, Washington, D.C.

Bureau of Labor Statistics. (1999). *National Occupational Employment and Wage Estimates: Office and Administrative Support Occupations*, U.S. Department of Labor, Washington, D.C.

Burrus, C. S., Gopinath, R. A., and Guo, H. (1998), *Introduction to Wavelets and Wavelet Transforms: A Primer*, Prentice Hall, Upper Saddle River, NJ.

Buurman, P., Pape, T., and Muggler, C. C. (1997). "Laser grain-size determination in soil genetic studies: 1. Practical problems." *Soil Science*, Williams & Wilkins, 162(4), pp. 211-218.

Cangelosi, V. E., Taylor, P. H, and Rice, P. F. (1983). *Basic Statistics 3rd. Edition*, West Publishing, St. Paul, Minnesota.

Canny J. (1986). "A computational approach to edge detection." *Transactions on pattern analysis and machine intelligence*, IEEE, 8(6), pp. 679-698.

Caspi, D., and Kiryati, N. (1998). "Range imaging with adaptive color structured light." *Transactions on pattern analysis and machine intelligence*, IEEE, 20(5), pp. 470-480.

Cheung, C. C. and Ord, A. (1990). "An on line fragment size analyzer using image processing techniques." *Third International Symposium on Rock Fragmentation by Blasting*, AusIMM, Brisbane, Queensland, pp. 233-238.

Chui, C. K. (1992), *An Introduction to Wavelets*, Academic Press, Inc., San Diego, CA.

CILAS. (2000), "Laser particle size analyzers." <http://www.cilasus.com/theory/> (Jan. 4. 2002)

Coakley, J. P., and Syvitski J. P. M. (1991). "SediGraph technique." *Principles, methods, and application of particle size analysis*, Cambridge University Press, New York, pp. 129-142.

Concrete Equipment Company. (1999). *Coneco 454, Product Brochure, Bulletin 396*, Blair, NE.

Daubechies, I. (1992). *Ten Lectures on Wavelets*, CBMS series, SIAM, Philadelphia, PA.

Day, D. D., and Rogers, D. (1996) "Fourier-based texture measures with application to the analysis of the cell structure of baked products." *Digital Signal Processing,* Academic Press, 6(3), pp. 138-144.

Dearnley, R. (1985). "Effects of resolution on the measurement of grain size." *Mineralogical Magazine,* Mineralogical Society, Vol. 49, pp. 539-546.

DePiero, F. W., and Trivedi, M. M. (1996). 3-D computer vision using structured light: design, calibration, and implementation issues. *Advances in computers*, Academic Press, Vol. 43, pp. 244-278.

Dobrowolski, J. A. (1998). *Concrete Construction Handbook*, McGraw-Hill, New York, NY.

Dougherty, E. R. (1993). *Mathematical morphology in image processing*, Marcel Dekker, Inc., New York, NY.

Dumitru, I., Zdrilic, A., Browne, I., and Lieber, K. (1999). "Optimisation of plant performance and product variability using VisionSizing technology." *Proc., 7th Annual Symposium,* ICAR, Austin, Texas.

Fernlund, J. M. R. (1998). "The effect of particle form on sieve analysis: a test by image analysis." *Engineering Geology*, Elsevier, 50(1), pp. 111-124.

Frazier, M. W. (1999), *An Introduction to Wavelets through Linear Algebra*, Springer-Verlag, New York, NY.

Ghalib, A. M., and Hryciw, R. D. (1999). "Soil particle size distribution by mosaic imaging and watershed analysis." *Journal of Computing in Civil Engineering*, ASCE, 13(2), pp. 80-87.

Gonzalez, R. C., and Wintz, P. (1987). *Digital Image Processing 2nd ed.*, Addison-Wesley, Reading, MA.

Gotlieb, C. C., and Kreyszig, H. E. (1990). "Texture descriptors based on co-occurrence matrices." *Computer Vision, Graphics, and Image Processing,* Academic Press, 51(1), pp. 70-86.

Haas, C. T. (1990). “A Model of pavement surfaces.” PhD dissertation, Carnegie Mellon University, Pittsburgh, PA.

Huber, D. F., and Hebert, M. (1999). “A new approach to 3-D terrain mapping.” *Proc., International Conference on Intelligent Robots and Systems,* IEEE/RSJ, Kyongju, Korea.

Illerstrom, A. (1998). “A 3-D laser technique for size, shape, and texture analysis of ballast.” Master thesis, Royal Institute of Technology, Stockholm.

Jahn, D. W. (2000). "Evaluation of aggregate particle shapes through multiple ratio analysis." *Proc., 8th Annual Symposium,* ICAR, Denver, CO.

Kemeny, J. M., Devgan, A., Hagaman, R. M., and Wu, X. (1993). “Analysis of rock fragmentation using digital image processing.” *Journal of Geotechnical Engineering*, ASCE, 119(7), pp. 1144-1160.

Kennedy, S. K., and Mazzullo, J. (1991). “Image analysis method of grain size measurement.” *Principles, methods, and application of particle size analysis*, Cambridge University Press, New York, pp. 76-87.

Kennedy, T. W., Huber, G. A., Harrigan, E. T., Cominsky, R. J., Hughes, C. S, Harold, V. Q., and Moulthrop, J. S. (1994). *Superior performing asphalt pavements (Superpave): The product of the SHRP asphalt research program*. Strategic Highway Research Program, National Research Council, Washington, D.C.

Kim, H., Browne, C., Rauch, A. F., and Haas, C. T. (2000) "Technical aspect of implementing rapid aggregate gradation" *Proc., 8th Annual Symposium,* ICAR, Denver, CO.

Kim, H., Haas, C. T., Rauch, A. F., and Browne, C. (2001). “A prototype laser scanner for characterizing size and shape parameters in aggregates. *Proc., 9th Annual Symposium,* ICAR, Austin, Texas.

Kruse, C. G. (1999). “Implementation plan for automating highway-materials testing.” *National Cooperative Highway Research Program - Report 427*, TRB, Washington, D.C.

Kuo, C. and Freeman, R. B. (2000). “Imaging indices for quantification of shape, angularity, and surface texture of aggregates. *Proc., 79th Annual Meeting,* TRB, Washington, D.C.

Kuo, C., Frost, J. D., Lai, J. S., and Wang, L. (1996). "Three-dimensional image analysis of aggregate particles from orthogonal projections." *Emerging Technologies in Geotechnical Engineering, Transportation Research Record No. 1526*, TRB, Washington, D.C.

Kuo, C.-Y., Rollings, R.S., and Lynch, L.N. (1998). "Morphological study of coarse aggregates using image analysis." *Journal of Materials in Civil Engineering*, Vol. 10, No. 3, pp. 135-142.

Laboratoire Central des Ponts et Chaussees. (1995). *Product Brochure, VDG 40 - mlpc R 112*, France.

Loizeau, J. L., Arbouille, D., Santiago, S., and Vernet, J. P. (1994). "Evaluation of a wide range laser diffraction grain size analyzer for use with sediments." *Sedimentology*, Blackwell Scientific Publishers, 41(2), pp. 353-361.

Maerz, N. H. (1999). "Online fragmentation analysis: achievements in the mining industry." *Proc., 7th Annual Symposium,* ICAR, Austin, Texas.

Maerz, N. H., and Lusher, M. (2001). "Measurement of flat and elongation of coarse aggregate using digital image processing." *Proc., 80th Annual Meeting,* TRB, Washington, D.C.

Mallat, S. (1999). *A Wavelet Tour of Signal Processing, Second Edition*, Academic Press, San Diego, CA.

Masad, E. (2001). Review of Imaging Techniques for Characterizing the Shape of Aggregates Used in Asphalt Mixes. *Proc., 9th Annual Symposium, ICAR,* Austin, Texas.

Masad, E, Button, J. W., and Papagiannakis, T. (2000), "Fine aggregate angularity: automated image analysis approach." *Proc., 79th Annual Meeting,* TRB, Washington, D.C.

Masad, E, Olcott, D., White, T., and Tashman, L. (2001) "Correlation of imaging shape indices of fine aggregate with asphalt mixture performance." *Proc., 80th Annual Meeting,* TRB, Washington, D.C.

McCave, I. N., and Syvitski, J. P. M. (1991). "Principles and methods of geological particle size analysis." *Principles, methods, and application of particle size analysis*, Cambridge University Press, New York, pp. 3-21.

Micromeritics Instrument Corporation. (1999). *Product Brochure, PDSA 5400 Data Sheet, 540-42701-00*, Norcross, GA.

Micromeritics Instrument Corporation. (1999). *Product Brochure, SediGraph*, Norcross, GA.

Moga, A. N. (1998). "Parallel marker-based image segmentation with watershed transformation." *Journal of Parallel and Distributed Computing*, Academic Press, 51(1), 27-45.

Mora, C. F., Kwan, A. K. H., and Chan, H. C. (1998). "Particle size distribution analysis of coarse aggregate using digital image processing." *Cement and Concrete Research*, Pergamon Press, 28(6), 921-932.

National Stone Association. (1993), *The Aggregate Handbook*, Mercury Press, Rockville, MD.

Newland, D. E. (1993). *An Introduction to Random Vibrations, Spectral & Wavelet Analysis: Third Edition*, Longman Scientific & Technical, New York, NY.

Oppenheim A. V., Schafer, R. W., and Buck, J. R. (1999), *Discrete-Time Signal Processing: Second Edition*, Prentice Hall, Upper Saddle River, NJ.

Parker, J. R. (1997). *Algorithms for Image Processing and Computer Vision*, John Wiley & Sons, Inc., New York, NY.

Parkin, R. M., Calkin, D. W., and Jackson, M. R. (1995). "Roadstone aggregate: an intelligent opto-mechatronic product classifier for sizing and grading." *Mechatronics,* Pergamon Press, 5(5), pp. 461-467.

Persson, A. (1998). "Image analysis of shape and size of fine aggregates." *Engineering Geology*, Elsevier, 50(1), pp. 177-186.

Peet, F. G., and Sahota, T. S. (1985). "Surface curvature as a measure of image texture." *Transactions on Pattern Analysis and Machine Intelligence,* IEEE, 7(6), pp. 734-738.

Pentland, A. P. (1984). "Fractal-based description of natural scenes." *Transactions on Pattern Analysis and Machine Intelligence,* IEEE, Vol. 6, pp. 661-674.

Pratikakis, I. E., Sahli, H., and Cornelis, J. (1999). "Low level image partitioning guided by the gradient watershed hierarchy." S*ignal Processing*, North-Holland Publication, 75(2), pp. 173-195.

Quantachrome Corporation. (1997). *Product Brochure, CILAS 940 Data Sheet*, Boynton Beach, FL.

Rao, R. M., and Bopardikar, A. S. (1998). *Wavelet Transforms*, Addison Wesley Longman, Inc., Reading, MA.

Rao, C, and Tutumluer, E. (2000). "A new image analysis approach for determination of volume of aggregates." *Proc., 79th Annual Meeting,* TRB, Washington, D.C.

Rotex Inc. (1997). *Product Brochure, Gradex 2000, Catalog 609*, Cincinnati, OH.

Saaty, T. L. (1980), *The Analytic Hierarchy Process*, McGraw-Hill, New York, NY.

Sonka, M., Hlavac, V., and Boyle, R. (1999). *Image Processing, Analysis, and Machine Vision*, PWS Publishing, Pacific Grove, CA.

Subers, J., Scheunders, P., Verhoye, M., Linden, A. V. D., Dyck, D. V., and Raman, E. (1997). "Watershed-based segmentation of 3D MR data for volume quantization." *Magnetic Resonance Imaging*, Elsevier, 15(6), pp. 679-688.

Taylor, V. L., and Costello, M. J. (1999) "Fourier analysis of textural variations in human normal and cataractous lens nuclear fiber cell cytoplasm." *Experimental Eye Research,* Academic Press, 69(2), pp. 163-174.

Tepordei V. V. (2001). "Mineral industry surveys: crushed stone and sand and gravel in the fourth quarter 2000." *U.S. Geological Survey*, Reston, VA.

Tolppanen, P., Illerstrom, A., and Stephansson, O. (1999). "3-D laser analysis of size, shape and roughness of railway ballast: research in progress." *Proc., 7th Annual Symposium,* ICAR, Austin, Texas.

Tsoukalas, L. H., and Uhrig, R. E. (1997), *Fuzzy and Neural Approaches in Engineering*, John Wiley & Sons, New York, NY.

U.S. Census Bureau. (1999a). *Asphalt Paving Mixture and Block Manufacturing, 1997, EC97M-3241B*, U.S. Department of Commerce, Economic and Statistics Administration, Washington, D.C.

U.S. Census Bureau. (1999b). *Concrete Block and Brick Manufacturing, 1997, EC97M-3273C*, U.S. Department of Commerce, Economic and Statistics Administration, U.S. Washington, D.C.

U.S. Census Bureau. (1999c). *Concrete Pipe Manufacturing, 1997, EC97M-3273D*, U.S. Department of Commerce, Economic and Statistics Administration, Washington, D.C.

U.S. Census Bureau. (1999d). *Other Concrete Product Manufacturing, 1997, EC97M-3273E*, U.S. Department of Commerce, Economic and Statistics Administration, Washington, D.C.

U.S. Census Bureau. (1999e). *Ready-Mix Concrete Manufacturing, 1997, EC97M-3272B*, U.S. Department of Commerce, Economic and Statistics Administration, Washington, D.C.

Valkenburg, R. J., and McIvor, A. M. (1998). "Accurate 3D measurement using a structured light system." *Image and Vision Computing*, Elsevier, 16(2), pp. 99-110.

Vince Hagen Company. (1999). *Product Brochure, HSM/897/CTP*, Dallas, Texas.

Vincent, L., and Soille, P. (1991). "Watersheds in digital spaces: an efficient algorithm based on immersion simulations." *Transactions on pattern analysis and machine intelligence*, IEEE, 13(6), pp. 583-598.

Wang, L., James, S. L., and Frost, J. D. (1997). "Fourier morphological descriptors of aggregate profiles." *Proc., Engineering Foundation Conference on Imaging Techniques: Techniques and Applications in Civil engineering*, ASCE, Davos, Switzerland, pp. 76-87.

Wang, W. (1998). "Binary image segmentation of aggregates based on polygonal approximation and classification of concavities." *Pattern Recognition*, Pergamon Press, 31(10), pp. 1503-1524.

Weingart, R. L., and Prowell, B. D. (1999). "Specification development using the VDG-40 Vidoegrader for shape classification of aggregates." *Proc., 7th Annual Symposium,* ICAR, Austin, Texas.

Wu, C. M., Chen, Y. C., and Hsieh, K. S. (1992). "Texture features for classification of ultrasonic liver images." *Transactions on Medical Imaging,* IEEE, Vol. 11, pp. 141-152.